ON THE USE OF THE EXPONENTIAL WINDOW METHOD

IN THE SPACE DOMAIN

A Dissertation

by

LI LIU

Submitted to the Office of Graduate Studies of
Texas A&M University
in partial fulfillment of the requirements for the degree of

DOCTOR OF PHILOSOPHY

May 2008

Major Subject: Civil Engineering

ON THE USE OF THE EXPONENTIAL WINDOW METHOD

IN THE SPACE DOMAIN

A Dissertation

by

LI LIU

Submitted to the Office of Graduate Studies of
Texas A&M University
in partial fulfillment of the requirements for the degree of

DOCTOR OF PHILOSOPHY

Approved by:

Chair of Committee,	Jose Roesset
Committee Members,	Paul Roschke
	Paolo Gardoni
	Joe Pasciak
Head of Department,	David Rosowsky

May 2008

Major Subject: Civil Engineering

ABSTRACT

On the Use of the Exponential Window Method in the Space Domain. (May 2008)
Li Liu, B.S., Tsinghua University, Beijing, China;
M.S., Tsinghua University, Beijing, China
M.S., Texas A&M University
Chair of Advisory Committee: Dr. Jose Roesset

Wave propagation in unbounded media is a topic widely studied in different science and engineering fields. Global and local absorbing boundary conditions combined with the finite element method or the finite difference method are the usual numerical treatments. In this dissertation, an alternative is investigated based on the dynamic stiffness and the exponential window method in the space-wave number domain. Applying the exponential window in the space-wave number domain is equivalent to introducing fictitious damping into the system. The Discrete Fourier Transform employed in the dynamic stiffness can be properly performed in a damped system. An open boundary in space is thus created. Since the equation is solved by the finite difference formula in the time domain, this approach is in the time-wave number domain, which provides a complement for the original dynamic stiffness method, which is in the frequency-wave number domain.

The approach is tested through different elasto-dynamic models that cover one-, two- and three-dimensional problems. The results from the proposed approach are compared with those from either analytical solutions or the finite element method. The comparison demonstrates the effectiveness of the approach. The incident waves can be efficiently absorbed regardless of incident angles and frequency contents. The approach proposed in this dissertation can be widely applied to the dynamics of railways, dams, tunnels, building and machine foundations, layered soil and composite materials.

To Alex, Dongmin and my family,

ACKNOWLEDGEMENTS

First of all, I would like to show my deepest gratitude to my advisor Dr. Jose Roesset. I still remember the first day of my Plates and Shells class with Dr. Roesset. He brought in no notes but started writing on the blackboard directly. Never before had I met a professor that could do this. Soon I came to the realization that I just met the most knowledgeable and productive, or simply the best researcher in our field. It was one of the happiest moments in my life when he agreed to advise me. Throughout my graduate study at Texas A&M University he gave me invaluable guidance, inspiration, and tremendous support and encouragement. His wisdom, experiences and sense of humor are the source of my power to overcome the difficulties in my research. What I have learned from him, academic and nonacademic, will benefit me for a lifetime.

I want to thank Dr. Paolo Gardoni for his excellent teaching in probability and statistics and for his advice on my dissertation. I would also like to thank Dr. Paul Roschke for his suggestion on my dissertation. I appreciate his view of what courses a PhD student should take. I am specially grateful to Dr. Joe Pasciak for his finite element class which opened a new horizon for my understanding of numerical methods. Also I appreciate his advice on my dissertation.

I am very pleased to have the chance to make friends with the “Gang in the Basement” who are actually excellent graduate students of civil engineering. I learned so much from them and we enjoyed numerous joyful moments.

Finally, I would like to thank my wife, Dongmin and my family. They gave me endless love and support throughout all these years. Without them, I would not have been able to reach this goal.

TABLE OF CONTENTS

CHAPTER Page

LIST OF FIGURES

FIGURE Page

LIST OF TABLES

CHAPTER I

INTRODUCTION

1.1 Overview

Wave propagation in unbounded media is a topic widely studied in different science and engineering fields such as geophysics, acoustics, electromagnetics, oceanography, etc. In these fields, the domain of the problem is so large that it is considered to be infinite in the practical sense. In civil and structural engineering, this situation emerges in soil-structure interaction [1] or fluid-structure interaction problems [2], when wave propagation in the unbounded soil and rock layers, in a reservoir, or in the ocean is considered. It can be found particularly in problems involving railways, tunnels, dams, machine and building foundations, offshore structures, etc.

To accommodate traditional numerical tools such as the finite element method, the infinite domain has to be truncated to make possible its discretization. Once the domain is truncated, the boundary condition on the truncated domain must be carefully considered. The conventional physical boundaries, Dirichlet or Neumann boundary conditions for instance, induce reflections when the incident waves from within the domain reach the boundary. These reflected waves are spurious in the context of the original problem because there should be no incoming waves from infinity in an unbounded domain, according to Sommerfeld's radiation condition [3]. In order to remove the spurious reflected waves, a different type of boundary must be applied. This boundary, called an absorbing boundary, should be able to absorb all incident waves from within the domain, regardless of their frequency contents and incident angles. The original unbounded domain is then simulated by a truncated domain combined with an absorbing boundary. Waves exit the truncated domain as if there were no boundary or there were only an open boundary.

This dissertation follows the style of Wave Motion.

Besides applications in unbounded domains, the absorbing boundary can be applied to finite domain problems too. When the domain to be studied is very large but only part of the domain is of interest and the reflected waves are not a concern, performing computation over the entire domain is not desirable. The domain is truncated so that the computational load can be reduced. In this case, an absorbing boundary must also be placed on the truncated domain.

1.2 Existing Methods

1.2.1 Classification of absorbing boundaries

Due to its significance, many researchers have proposed different absorbing boundaries since the 1970's. Basically there are two types of absorbing boundaries, namely absorbing boundary conditions and absorbing boundary layers. The former refers to a mathematical condition on the boundary. The latter is a fictitious layer attached to the truncated domain. Figure 1.1 shows these two types of absorbing boundaries. The boundary condition in Figure 1.1(a) is actually the original condition proposed by Clayton and Enqguist [4], where P is the displacement and V the wave velocity. The subscript stands for derivatives with respect to space and time, respectively. The boundary layer in Figure 1.1 (b) has damping in it so that any wave running across the interface between the truncated domain and the layer, indicated by the dashed line, will be dissipated before it can be reflected on the outer boundary of the layer, indicated by the solid line, and bounced back into the truncated domain.

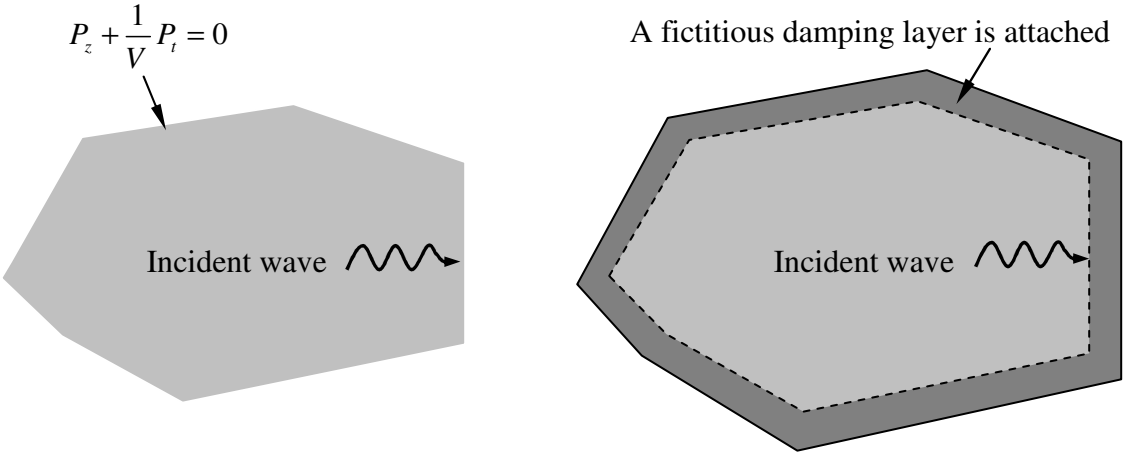

(a) An absorbing boundary (b) An absorbing layer

Figure 1.1 Two different types of absorbing boundaries

In the category of absorbing boundary conditions, there are two different types. The first one is known as local boundary conditions. They usually involve the derivatives of the unknown variable, displacement for example, with respect to time and space. The other type is the so-called global boundary conditions. They usually represent the relation between stresses and displacements on the boundary.

1.2.2 Local absorbing boundary conditions

The original work of Clayton and Enqguist [4], and Lindman [5] belongs to this category. Also included in this category are the boundaries proposed by Bayliss and Turkel [6], and Higdon [7]. Along this track, Collino [8], Grote and Keller [9], and Gudatti [10] introduced different high-order local boundary conditions.

The basic idea of the local boundary conditions derives from the characteristic equation or the dispersion relation of the wave equation in the frequency-wave number domain. In the dispersion relation, the wave number is allowed to be both positive and negative so that wave propagation in both positive and negative directions is represented.

To derive the absorbing boundary condition, wave propagation in one direction, either positive or negative, is deliberately removed from the dispersion relation by choosing only the positive or negative wave number. This new dispersion relation represents the one-way wave propagation. The new dispersion relation, usually involving square roots, is then approximated by the Padé series [11]. The inverse Fourier transform of this approximate relation brings it back into the time-space domain and a one-way wave equation is created. Application of this one-way wave equation on the boundary leads to an absorbing boundary condition.

Depending on the order of approximation in the Padé series, local boundary conditions can be classified as low-order or high-order. Low-order conditions use fewer terms in the Padé series and involve only low-order derivatives. Therefore they are easy to implement. However, accuracy is compromised since the original dispersion relation is not well approximated. The high-order conditions, on the other hand, use more terms in the Padé series so they are more accurate. However, the larger number of terms results in difficulty for the finite element or finite difference implementation.

In the work cited above, Clayton and Enqguist's condition is a low-order one; so are the conditions of Bayliss and Turkel. Collino is believed to be the first to propose a high order local condition and his approach laid the foundation for many other high order conditions. Furthermore his approach also covers the idea of low order conditions. So Collino's method is summarized here.

Consider the horizontal shear (SH) wave equation in a two-dimensional domain where u is the out-of-plane displacement.

$$\frac{\partial^2 u}{\partial t^2} = c_s \nabla^2 u \tag{1.1}$$

where

c_s = Shear wave velocity

∇^2 = Laplace operator $\frac{\partial^2}{\partial x^2} + \frac{\partial^2}{\partial y^2}$

The characteristic equation of Equation (1.1) is

$$m^2 + n^2 = \frac{\omega^2}{c_s} \tag{1.2}$$

where

m = wave number in x direction

n = wave number in y direction

ω = frequency

From Equation (1.2), the wave number m can be solved.

$$m = \frac{\omega}{c_s}\sqrt{1 - \frac{c_s^{\,2}}{\omega^2} n^2} \tag{1.3}$$

Only the positive root is chosen to represent a wave propagating in the positive direction. Multiplying Equation (1.3) by $\tilde{\tilde{U}}(m,n)$, which is the Fourier transform of u with respect to x, y and t, one obtains

$$m\tilde{\tilde{U}} = \frac{\omega}{c_s}\sqrt{1 - \frac{c_s^{\,2}}{\omega^2} n^2}\,\tilde{\tilde{U}} \tag{1.4}$$

Performing the inverse Fourier transform with respect to m.

$$\frac{\partial \tilde{U}}{\partial x} + j\frac{\omega}{c_s}\sqrt{1 - \frac{c_s^{\,2}}{\omega^2} n^2}\,\tilde{U} = 0 \tag{1.5}$$

where

$\tilde{U}(n)$ = the Fourier transform of u with respect to y and t.

j = unit imaginary number

Expanding the square root in a Padé series,

$$\sqrt{1 - \frac{c_s^{\,2}}{\omega^2} n^2} \approx 1 - \sum_{i=1}^{N} \frac{\alpha_i n^2}{\omega^2 / c_s^{\,2} - \beta_i n^2} \tag{1.6}$$

where

$$\alpha_i = \frac{2\sin^2(i\pi/(2N+1))}{2N+1}$$

$$\beta_i = \cos^2\frac{i\pi}{2N+1}$$

Equation (1.5) can be rewritten as

$$\frac{\partial \tilde{\tilde{U}}}{\partial x} + j\frac{\omega \tilde{\tilde{U}}}{c_s} - j\frac{\omega}{c_s}\sum_{i=1}^{N}\frac{\alpha_i n^2 \tilde{\tilde{U}}}{\omega^2 / {c_s}^2 - \beta_i n^2} = 0 \tag{1.7}$$

Defining $\tilde{\tilde{\phi}}_i = \frac{\alpha_i n^2 \tilde{\tilde{U}}}{\omega^2 / {c_s}^2 - \beta_i n^2}$, from Equation (1.7)

$$\frac{\partial \tilde{\tilde{U}}}{\partial x} + j\frac{\omega \tilde{\tilde{U}}}{c_s} - j\frac{\omega}{c_s}\sum_{i=1}^{N}\tilde{\tilde{\phi}}_j = 0 \tag{1.8}$$

Performing the inverse Fourier transform with respect to *y* and *t*, one obtains

$$\frac{\partial u}{\partial x} + \frac{1}{c_s}\frac{\partial u}{\partial x} - \frac{1}{c_s}\sum_{i=1}^{N}\phi_j = 0 \tag{1.9}$$

It is known from the definition of $\tilde{\tilde{\phi}}_i$ that

$$(\omega^2 / {c_s}^2 - \beta_i n^2)\tilde{\tilde{\phi}}_i = \alpha_i n^2 \tilde{\tilde{U}} \tag{1.10}$$

Performing finally the inverse Fourier transform of Equation (1.10) with respect to *y* and *t*,

$$-\frac{1}{{c_s}^2}\frac{\partial^2 \phi_i}{\partial t^2} + \beta_i \frac{\partial^2 \phi_i}{\partial y^2} = \alpha_i \frac{\partial^2 u}{\partial y^2} \tag{1.11}$$

(1.9) and (1.11) represent *N+1* equations with *N+1* unknowns $\phi_i, i = 1,2...N$ and *u*. This is Collino's absorbing boundary condition of order N. It contains only second-order derivatives. But with the higher order, the implementation becomes more difficult as the number of terms increases.

It is interesting to see that in Equation (1.6), if only the constant term "1" is taken, one will get

$$\frac{\partial \tilde{\tilde{U}}}{\partial x} + j\frac{\omega}{c_s}\tilde{\tilde{U}} = 0 \tag{1.12}$$

Taking the inverse Fourier transform of Equation (1.12) with respect to *t* and *y*, Clayton and Enqguist's condition is obtained.

$$\frac{\partial u}{\partial x}+\frac{1}{c_s}\frac{\partial u}{\partial t}=0 \tag{1.13}$$

1.2.3 Global absorbing boundary conditions

The second type of absorbing boundary conditions is constituted by the global conditions. Unlike local conditions, the underlying mechanism of different global conditions varies significantly. However, most of them are based on the relation between stresses and displacements on the boundary. This relation is essentially the dynamic stiffness matrix of the medium outside the truncated domain, referred to as exterior here. Since the global condition describes the exact physics of wave propagation in the exterior, it is an exact absorbing boundary condition.

The consistent transmitting boundary condition proposed by Waas [12], and Kausel and Roesset [13] is a global condition. Waas addressed 2D problems in Cartesian coordinates and axisymmetric problems. Kausel and Roesset solved the general 3D problem in cylindrical coordinates. The idea is to represent the displacements on the boundary in terms of the natural modes of one-way wave propagation in an unbounded layer. From here, the relation between the stresses and displacements, or the exact dynamic stiffness matrix of the exterior is found. This dynamic stiffness matrix is then assembled with the dynamic stiffness matrix of the truncated domain so that the entire unbounded domain is taken into account. This idea was later picked up by Hagstrom and Keller [14] and in their work they even proved the existence of such an exact condition for certain nonlinear problems. Since the method proposed in this dissertation is closely related to the idea of the energy-transmitting boundary, it is not summarized here and will be elaborated in later chapters.

Another global condition proposed by Roesset and Scaletti [15] is based on the cloning and dynamic condensation of the dynamic stiffness matrix of a layer with finite length. Along this track, Wolf and Song extended the idea and developed the Consistent

Infinitesimal Finite Element Cell Method [16]. The basic idea of this boundary is summarized in the following.

Consider a series of identical columns of finite elements extending to a certain distance as shown in Figure 1.2.

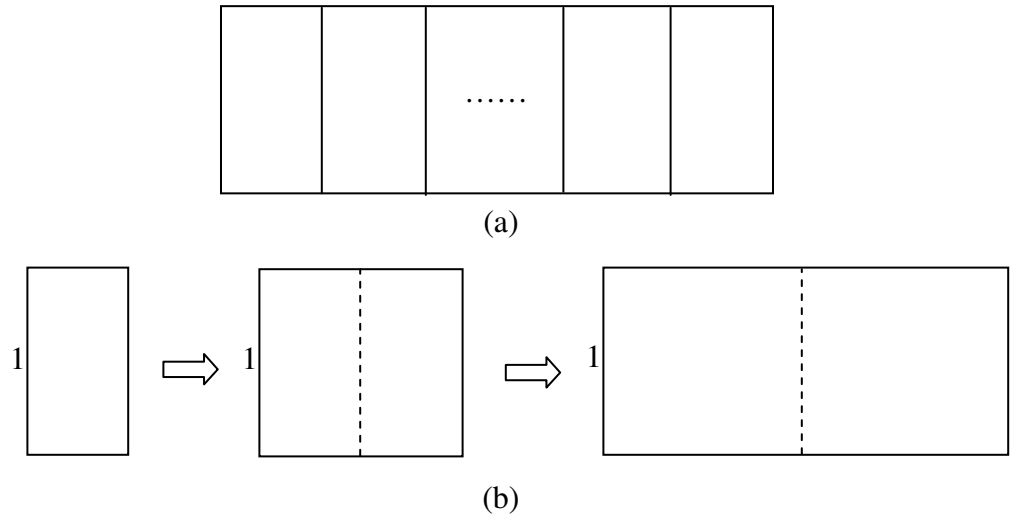

Figure 1.2 The 2D boundary matrices method

Assume that the dynamic stiffness matrix of a particular column is partitioned as

$$K_1 = \begin{bmatrix} K_{11} & K_{12} \\ K_{21} & K_{22} \end{bmatrix} \tag{1.14}$$

where

K_{ij} = sub-matrices with "1" referring to the left vertical boundary and "2" to the right.

The dynamic stiffness matrix for the combination of 2 columns can be readily obtained as.

$$K_2 = \begin{bmatrix} K_{11} & K_{12} & 0 \\ K_{21} & K_{11} + K_{22} & K_{12} \\ 0 & K_{21} & K_{22} \end{bmatrix}$$

The equation for this combination of 2 columns is

$$\begin{bmatrix} K_{11} & K_{12} & 0 \\ K_{21} & K_{11}+K_{22} & K_{12} \\ 0 & K_{21} & K_{22} \end{bmatrix} \begin{Bmatrix} U_1 \\ U_2 \\ U_3 \end{Bmatrix} = \begin{Bmatrix} F_1 \\ F_2 \\ F_3 \end{Bmatrix} \tag{1.15}$$

If there are no external forces acting on Nodes 2, i.e., $F_2 = 0$, the above equation can be condensed with U_2 eliminated

$$\begin{bmatrix} K_{11}-K_{12}K_{21}(K_{11}+K_{22})^{-1} & -K_{12}K_{21}(K_{11}+K_{22})^{-1} \\ -K_{12}K_{21}(K_{11}+K_{22})^{-1} & K_{22}-K_{12}K_{21}(K_{11}+K_{22})^{-1} \end{bmatrix} \begin{Bmatrix} U_1 \\ U_2 \end{Bmatrix} = \begin{Bmatrix} F_1 \\ F_2 \end{Bmatrix} \tag{1.16}$$

Equation (1.16) can be repeated iteratively to cover a truly large distance increasing by the power of 2. If the system has some damping in it, after a few iterations, the distance would be long enough to have all the waves practically damped out.

A nice feature of the above approach is that it can be extended to the 3D case as shown in Figure 1.3 with the top view of the rings. The dynamic stiffness matrix of each ring can be again partitioned as in Equation (1.14) with "1" referring to the inner boundary of the ring and "2" the outer boundary of the ring. In this case, however, the matrices corresponding to a new element would be equal to those of the preceding one multiplied by a constant.

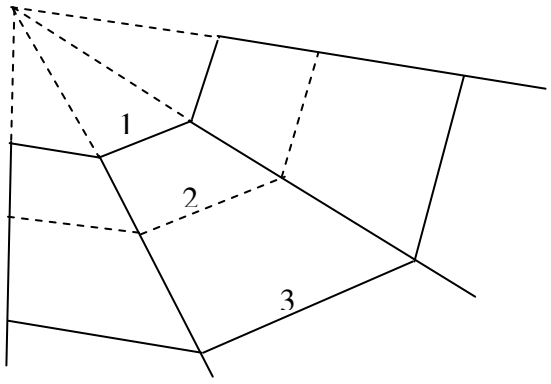

Figure 1.3 The 3D boundary matrices method

Other global conditions exist. Fix and Marin [17] introduced an exact condition involving the solution of an integral equation on the boundary. The integral equation, however, was solved numerically, which introduces an approximation. Keller and Givoli [18] then modified the method of Fix and Marin by imposing a circular and a spherical boundary in the 2D and 3D problems, respectively.

Although the global conditions are exact, they tend to be computationally expensive. For instance, in the consistent transmitting boundary, it is necessary to solve an eigenvalue problem and in Fix and Marin's approach, an integral equation has to be solved numerically. Therefore, the advantages of global conditions over the local conditions in relation to accuracy do not come by without a cost. It should be pointed out that the local conditions can be made as accurate as needed by increasing their order, but this is also achieved at an increased cost of implementation.

Another way to classify absorbing boundary conditions is to distinguish them according to the domain in which they are studied. Local conditions are usually in terms of derivatives with respect to time and space. So they are in the time-space domain. Most of the global conditions involve a dynamic stiffness matrix, which is usually written in terms of frequency and wave number. So global conditions are normally in the frequency-wave number domain. There are, however, occasions in which one would prefer to work in the time domain.

1.2.4 Absorbing layers

The second category of absorbing boundaries is the absorbing boundary layer. Different from the absorbing boundary conditions, the absorbing boundary layer is not a mathematical condition on the boundary of the truncated domain. Rather it is a fictitious layer attached to the truncated domain, as shown in Figure 1.1. The most popular one in this category is the Perfectly Matched Layer (PML). This method was first introduced by Berenger to deal with electromagnetic wave propagation in an unbounded medium [19]. Almost immediately, Chew and Weedon [20] pointed out that Berenger's approach is

actually equivalent to a complex coordinate transform, or coordinate stretching to be precise.

Due to its flexibility in dealing with problems of different geometry, material properties and underlying physics, PML is widely used by researchers in different areas, such as electromagnetics, elastodynamics, acoustics, etc. To name just a few of the researchers in elastodynamics, Liu and Chew [21] were the first ones to introduce PML into elastodynamic wave propagation problems. They solved the problem with finite differences. Collino and Tsogka [22] also derived a PML for the stress-displacement finite difference formulation. Basu and Chopra [23] presented a displacement-based, symmetric finite element implementation of the PML.

As mentioned before, the key idea of PML is that a complex coordinate stretching is equivalent to the introduction of damping in the layer. This can be illustrated by the simple example of a 1D wave in an infinite bar on an elastic foundation as shown in Figure 1.4. The bar is put on an elastic foundation so that it will not fly away. It does not really matter if it is on an elastic foundation for the sake of PML.

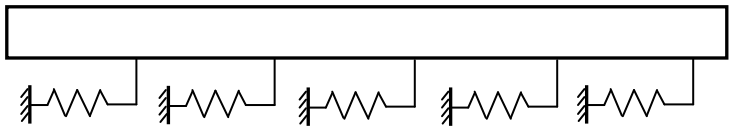

Figure 1.4 A bar on an elastic foundation

The equation of motion is

$$\rho A \frac{\partial^2 u}{\partial t^2} - EA \frac{\partial^2 u}{\partial x^2} + \zeta u = f \tag{1.17}$$

where

u = displacement

E = Young's modulus

ρ = mass density

A = area of cross section

ζ = elastic coefficient of the foundation

f = distributed external load

Consider a solution of the form

$$u = A\exp[j(kx - \omega t)] \tag{1.18}$$

where

k = wave number with positive real part

ω = frequency

j = unit imaginary number $\sqrt{-1}$

The dispersion relation or the characteristic equation of Equation (1.17) is

$$EAk^2 + \zeta - \rho A\omega^2 = 0 \tag{1.19}$$

Obviously this represents a dispersive wave. In Solution (1.18), only propagating waves are considered, which means ω is above the cut-off frequency and k should be real. Performing a coordinate stretching defined by

$$\tilde{x} = \int_0^x \lambda(s)ds \tag{1.20}$$

where

$\tilde{x}$ = the new coordinate

$\lambda(x)$ is a nonzero and continuous function

in the new coordinate, the equation keeps its form so that the solution can be written as

$$u = A\exp[j(k\tilde{x} - \omega t)] \tag{1.21}$$

If the stretching function is chosen as

$$\lambda(x) = 1 + jf(x) \tag{1.22}$$

where

$f(x)$ = a chosen function, for instance, x^2

from Equation (1.20), the new coordinates can be expressed in terms of the old one, as

$$\tilde{x} = \int_0^x (1 + jf(x))ds = x + j\int_0^x f(x)ds \tag{1.23}$$

Then in the x coordinate, the solution is

$$u = A\exp(-k\int_0^x f(x)dx)\exp(j(kx - \omega t)) \tag{1.24}$$

From (1.24), it can be seen that the propagating wave is spatially modulated by a decaying exponential window. Meanwhile at $x = 0$, the coordinate transform gives $\tilde{x} = x$, which means no stretching or damping is introduced. If the interface between the truncated domain and the layer is put at $x = 0$, everything on the interface is continuous so there will be no reflections.

From the above description, it is understood that the complex coordinate stretching introduces damping in the layer. This is exactly how the PML dissipates the waves entering the layer. Meanwhile the coordinate stretching is ingeniously designed so that on the interface between the truncated domain and the layer, the material property, or damping ratio, is continuous. Therefore there will be no wave reflected on the interface in the first place. The absorbing property of the layer depends on layer thickness and the stretching function $\lambda(x)$. Fictitious damping can also be introduced into the system by a complex wave number shift in the wave number domain. Spatial decaying of the propagating wave is similarly achieved.

While PML is a very flexible approach, it has some disadvantages. One big drawback is its need for splitting the unknown field in 2D or 3D cases to accommodate the coordinate stretching, which complicates the implementation significantly. Obviously the number of degrees of freedom in the PML doubles due to this unphysical splitting of the unknown fields. On the interface, the split fields in the PML and the unsplit fields in the truncated domain need to be matched, which adds even more complications to the implementation.

1.3 Alternative Approaches

In this section, a new approach is suggested, which is closely related to the dynamic stiffness method followed by Gazetas [24] to find the stiffness functions of strip and rectangular footings, but using the thin layer method (TLM) instead of the exact layer matrices in the frequency-wave number domain, and making use of the exponential window method (EWM). To provide a clear description of the approach, it is appropriate to start with the TLM.

As mentioned before, the TLM was first introduced by Waas [12] to address 2D plane wave propagation problems in Cartesian coordinates or axisymmetric problems in cylindrical coordinates. It was then extended to general 3D wave propagation by Kausel [25] in cylindrical coordinates. Kausel and Roesset [13] introduced then the concept of a "hyper-element". In Waas' formulation, the displacement field is approximated in the depth direction by finite element expansions with an exact expression in the horizontal direction in terms of wave number and frequency. In Kausel's formulation, the displacement field is approximated by finite element expansions in the depth direction, a Fourier series in the tangential direction and Hankel functions in the radial direction. At the interface between the core region and the external region, the energy-transmitting boundary is applied (Figure 1.5).

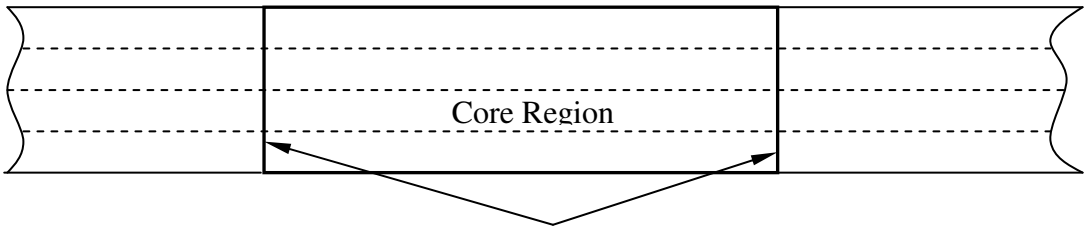

Energy Transmitting Boundary

(a) The TLM of Waas

Figure 1.5 The thin layer method

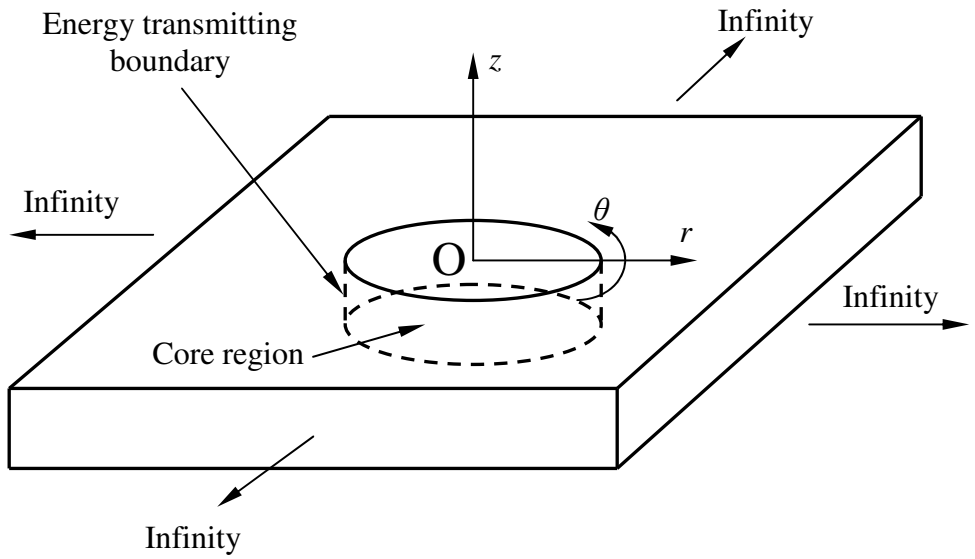

(b) The TLM of Kausel and Roesset

Figure 1.5 Continued

The TLM was further studied and developed to deal with different kinds of problems. Tan [26] formulated the finite element method for layered fluid-soil media. Ghibril [27] demonstrated the capability of TLM for the problem of wave scattering due to finite interfacial cracks. The strip element method developed by Liu and Achenbach [28] to investigate wave scattering in anisotropic media was essentially the thin layer method.

Kausel and Roesset then developed the dynamic stiffness method for the same layered medium problem [29]. They formulated the exact dynamic stiffness matrix of a layer on the basis of the Haskell-Thompson transfer matrix. Using this approach, Kausel and Peek [30] later obtained an explicit closed form solution for the Green's functions corresponding to dynamic loads acting on or within layered strata. The original idea of dynamic stiffness was then picked up by Gazetas [24] to calculate the stiffness functions for surface strip footings and rectangular foundations. Gazetas used an expansion of the load by the Discrete Fourier Transform and combined it with the dynamic stiffness matrix of soil layers in the frequency-wave number domain. In this approach, the

dynamic stiffness matrix is analytical. Unlike the thin layer method, the medium is no longer divided up into a core region and an exterior. The unknown fields are solved directly in the frequency domain. The solution in the time domain is then obtained through the inverse Fourier transform. In the presence of damping, which is typical in the case of wave propagation in soil, the waves are practically damped out after a certain distance. Therefore if the computational area is carefully chosen, the problem of unboundedness can be circumvented.

The advantages of this approach over the consistent boundary matrix in the TLM is that is does not require the subdivision of each physical soil layer and that it provides an exact solution for an underlying elastic half space. The limitations are that it requires some internal damping in the soil and the use of a large number of points along the surface (number of terms in the Discrete Fourier Transform) to guarantee that waves attenuate within the domain considered. This same approach was later used by Doyle to treat general wave propagation problems in structures [31,32]. It has been referred to as the "spectral finite element method" although this same terminology is being used for a different type of finite elements. Also using this approach, Al-Khoury et al [33] studied the wave propagation associated with the Falling Weight Deflectometer.

Based on the above discussion, it is clear that the TLM works for systems with or without damping but requires a consistent energy absorbing boundary. The dynamic stiffness approach does not need an absorbing boundary but requires the existence of internal damping. Here a new approach is investigated, in which the need for energy absorbing boundary in the TLM or damping in the dynamic stiffness method is eliminated. This can be achieved through the exponential window method (EWM).

Originally the EWM was used in digital signal processing (DSP) to reduce leakage when the Discrete Fourier Transform was used [34]. Kausel and Roesset were the first to introduce this method to solve elastodynamic systems with small or no damping [35]. In all frequency domain methods, when the Discrete Fourier Transform (DFT), which is the version of Fourier transform implemented on a computer, is performed, one needs to deal with the initial conditions problem. If the free vibration terms of a dynamic

system's response are not damped out before the time range of interest, errors will be introduced.

To fix this problem, people add trailing zeroes to prolong the duration so that the free vibration will damp out before the start of the time range of interest. The limit of this approach is obvious. If a system has no damping at all, the free vibration will never damp out regardless of the length of trailing zeroes. In Kausel and Roesset's approach, a complex frequency shift is performed to the frequency domain equation. This complex frequency shift leads to three changes to the original system. First, the input force is exponentially windowed in the time domain. Second, there is a complex frequency shift in the transfer function. Third, the response is also exponentially windowed in the time domain. The complex frequency shift in the transfer function actually introduces a certain amount of damping into the system. By appropriately choosing the frequency shift parameter, or the amount of damping, free vibration terms in the response of the new system can be practically damped out. This is desirable because it is exactly the requirement for correctly performing DFT. Therefore, the response in the new system can be correctly obtained through the dynamic stiffness method. Then the response of the original system can be reconstructed by imposing an inverse exponential window. The time point at which the analysis is cut does not matter any more. It can be said that an "open boundary in time" is created.

The implication of the above discussion is straightforward: if the problem were formulated in the wavenumber domain, and the same idea of the exponential window were applied the space point at which the model is cut would not matter any more. An open boundary in space would then be created.

The dynamic stiffness method of Kausel and Roesset is in the frequency-wave number domain. That is, to obtain the solution in the time-space domain, it is necessary to perform an inverse Fourier transform with respect to both frequency and wave number. In this dissertation, the equation is not written in the frequency-wave number domain. It is written in the time-wave number domain. For the solution in the time domain, an explicit scheme can be implemented such as the central difference formula.

The advantage of the explicit scheme, combined with a lumped mass matrix, is twofold. First, it eliminates the need for solving a simultaneous system of algebraic equations. Secondly, there is no need to form explicitly the global stiffness matrix, saving thus both memory and CPU time.

The thin layer method or the dynamic stiffness method can be implemented in Cartesian coordinates for 3D wave propagation problems. In this case, there are two possibilities. The first one is to solve the displacement field by the 2D Fourier transform in the horizontal plane and finite element discretization in the depth direction. This approach can be used to treat such problems as machine and building foundations. The second one is to solve the displacement field by finite element expansion on the cross-section and to use the Fourier transform in the longitudinal direction. This approach can be used to treat such problems as tunnels and dams.

1.4 Outline of the Dissertation

The objective of this dissertation is to investigate the applicability of the exponential window method in the space domain to solve wave propagation problems in unbounded media, using a formulation in the time domain with the thin layer method. In Chapter II, the general formulation of the proposed method, which can be applied to different types of wave propagation problems, is presented. Chapter III covers wave propagation in an infinite beam on elastic foundation as an application for one-dimensional cases. Chapter IV presents the application to the two-dimensional plane strain wave propagation problem. In Chapter V, three-dimensional wave propagation problems are discussed. Chapter VI summarizes the results of the research and proposes future work.

CHAPTER II

FORMULATION

2.1 Overview

This chapter describes the proposed method. It can be generally applied to one-dimensional, two-dimensional, and three-dimensional cases. The description begins with a modified form of the equations of motion of an elastodynamic system. The equations in the time-wave number domain are then derived. After this, the introduction of damping by a complex wave number shift is explained in detail. Some issues associated with the application in space rather than time of the exponential window method are also discussed.

2.2 Modified Equation of Motion

Consider the displacement formulation of a linear elastodynamic problem on a domain that is unbounded in some spatial direction. The original equations of motion of the system are a set of partial differential equations in terms of time and all the spatial coordinates. As the first step in the proposed method, the displacement fields must be approximated through a discretization process, for instance a finite difference approximation or a finite element expansion, in the spatial directions where the domain is finite. Through this process, the original equations of motion are changed so that only the derivatives with respect to the spatial coordinates where the domain is infinite are kept in the equations. These new equations are called the modified equations of motion in this dissertation, to distinguish them from the original equations of motion. If the domain is infinite in all directions, no discretization process is needed and the modified equations of motion are the same as the original ones.

Defining the displacement vector $\mathbf{U} = \{u_1, v_1, w_1, ...u_N, v_N, w_N\}^T$ with *u*, *v*, and *w* the displacements in the *x*, *y* and *z* directions, respectively, and *N* the number of degrees of freedom of the system, a modified equation of motion can be written as

$$\mathbf{M}\frac{\partial^2 \mathbf{U}(x, y, z, t)}{\partial t^2} + \mathbf{L}\mathbf{U}(x, y, z, t) = \mathbf{F}(x, y, z, t), \tag{2.1}$$

where

t = time

M = mass matrix of size $N \times N$

F = external force vector of size $N \times 1$

L = a linear differential operator of size $N \times N$

The entries in the linear operator **L** contain derivatives with respect to the space coordinates. They also contain information on material properties. In fact, the specific form of **L** depends both on the kinematics of the system, which reflect the relation between displacements and strains, and on the constitutive law, which reflects the relation between stresses and strains. Although Equation (2.1) is written in matrix form and the matrix form along with the number of degrees of freedom are usually associated with semi-discretized finite element equations, Equation (2.1) can represent a scalar equation.

As a simple example, consider the problem of a transverse wave propagating in an infinitely long Euler-Bernoulli beam. The original equation of motion is

$$EI\frac{\partial^4 w}{\partial x^4} - \rho A\frac{\partial^2 w}{\partial t^2} = q \tag{2.2}$$

where

w = deflection

E = Young's modulus

I = bending moment of inertia

ρ = mass density

A = area of cross section

q = distributed external load

Since the problem has only one spatial dimension and it is infinite, no discretization is needed and the modified equation of motion is the same as the original one. In this case, the matrices and vectors in Equation (2.1) all become scalars. Specifically $\mathbf{M} = \rho A$, $\mathbf{U} = w$, $\mathbf{L} = EI\dfrac{\partial^4}{\partial x^4}$, and $\mathbf{F} = q$.

Another example is the general 3D wave propagation in an unbounded space. The original equations of motion are [36]

$$\begin{aligned}
&(\lambda+\mu)\left(\frac{\partial^2 u}{\partial x^2}+\frac{\partial^2 v}{\partial x\partial y}+\frac{\partial^2 w}{\partial x\partial z}\right)+\mu\nabla^2 u+f_x=\rho\frac{\partial^2 u}{\partial t^2}\\
&(\lambda+\mu)\left(\frac{\partial^2 u}{\partial y\partial x}+\frac{\partial^2 v}{\partial y^2}+\frac{\partial^2 w}{\partial y\partial z}\right)+\mu\nabla^2 v+f_y=\rho\frac{\partial^2 v}{\partial t^2}\\
&(\lambda+\mu)\left(\frac{\partial^2 u}{\partial z\partial x}+\frac{\partial^2 v}{\partial z\partial y}+\frac{\partial^2 w}{\partial z^2}\right)+\mu\nabla^2 w+f_z=\rho\frac{\partial^2 w}{\partial t^2}
\end{aligned} \tag{2.3}$$

where

ρ = mass density

λ and μ = Lame constants

u, v, and w = displacements in x, y and z directions, respectively

f_x, f_y, and f_z = body force in x, y and z directions, respectively

$\nabla^2 = \dfrac{\partial^2}{\partial x^2}+\dfrac{\partial^2}{\partial y^2}+\dfrac{\partial^2}{\partial z^2}$, the Laplace operator

No discretization is needed and the modified equations of motion are the same. Therefore, Equation (2.3) can be written in the form of Equation (2.1) with the matrices.

$$\mathbf{U} = \begin{Bmatrix} u & v & w \end{Bmatrix}^T$$

$$\mathbf{M} = \begin{bmatrix} \rho & 0 & 0 \\ 0 & \rho & 0 \\ 0 & 0 & \rho \end{bmatrix}$$

$$\mathbf{F} = \begin{Bmatrix} f_x & f_y & f_z \end{Bmatrix}^T$$

$$\mathbf{L}=\begin{bmatrix} (\lambda+\mu)\dfrac{\partial^2}{\partial x^2}+\mu\nabla^2 & (\lambda+\mu)\dfrac{\partial^2}{\partial x\partial y} & (\lambda+\mu)\dfrac{\partial^2}{\partial x\partial z} \\ (\lambda+\mu)\dfrac{\partial^2}{\partial y\partial x} & (\lambda+\mu)\dfrac{\partial^2}{\partial y^2}+\mu\nabla^2 & (\lambda+\mu)\dfrac{\partial^2}{\partial y\partial z} \\ (\lambda+\mu)\dfrac{\partial^2}{\partial z\partial x} & (\lambda+\mu)\dfrac{\partial^2}{\partial z\partial y} & (\lambda+\mu)\dfrac{\partial^2}{\partial z^2}+\mu\nabla^2 \end{bmatrix}$$

These two examples do not need discretization. However, this process is needed when the domain is finite in one of the directions as will be shown in Chapter IV when 2D wave propagation in an unbounded strip is considered and in Chapter V when 3D wave propagation in an unbounded layer is considered. The linear operator **L** will include derivatives with respect to the space coordinates that are not eliminated by the discretization process.

2.3 Equation of Motion in the Time-Wave Number Domain

Applying the Fourier transform to Equation (2.1) with respect to all the space coordinates that are in the equation, and using the property governing the Fourier transform of the derivatives, Equation (2.1) can be written as

$$\mathbf{M}\frac{\partial^2 \bar{\mathbf{U}}(l,m,n,t)}{\partial t^2}+\bar{\mathbf{L}}(l,m,n)\bar{\mathbf{U}}(l,m,n,t)=\bar{\mathbf{F}}(l,m,n,t) \tag{2.4}$$

where

m, n, and l = wave numbers in x, y and z directions, respectively

$\bar{\mathbf{U}}$ = the Fourier transform of $\mathbf{U}$

$\bar{\mathbf{F}}$ = the Fourier transform of $\mathbf{F}$

The entries in matrix $\bar{\mathbf{L}}$ are now polynomials in terms of the wave numbers m, n and l. In the two examples given in Section 2.2, for the Euler Bernoulli beam

$\bar{\mathbf{L}} = EIm^4$.

and for the 3D wave propagation problem,

$$\bar{\mathbf{L}} = -\begin{bmatrix} \alpha & (\lambda+\mu)mn & (\lambda+\mu)ml \\ (\lambda+\mu)mn & \beta & (\lambda+\mu)nl \\ (\lambda+\mu)ml & (\lambda+\mu)nl & \gamma \end{bmatrix}.$$

where

$$\alpha = (\lambda+2\mu)m^2 + \mu(n^2+l^2)$$

$$\beta = (\lambda+2\mu)n^2 + \mu(m^2+l^2)$$

$$\gamma = (\lambda+2\mu)l^2 + \mu(m^2+n^2)$$

Equation (2.4) is in the time-wave number domain. In the original dynamic stiffness method of Kausel and Roesset, another Fourier transform with respect to time is performed to turn the equation into the frequency-wave number domain. In the frequency-wave number domain, one only needs to solve a set of algebraic equations to obtain the displacements.

Equation (2.4) can be solved directly in the time domain using, for instance, finite differences. For a diagonal mass matrix if the central difference scheme is used, there is no need to solve a set of simultaneous equations, making the solution very efficient. The time-wave number domain approach is not necessarily better than the frequency-wave number domain approach but it provides an alternative and a complement to the original method.

2.4 Finite Difference Solution

Approximating the second-order derivative in Equation (2.4) by the central difference formula,

$$\frac{\partial^2 \bar{\mathbf{U}}}{\partial t^2} = \frac{\bar{\mathbf{U}}^{(k+1)} - 2\bar{\mathbf{U}}^{(k)} + \bar{\mathbf{U}}^{(k-1)}}{\Delta t^2} \tag{2.5}$$

$$\bar{\mathbf{U}} = \bar{\mathbf{U}}^{(k)} \tag{2.6}$$

$$\bar{\mathbf{F}} = \bar{\mathbf{F}}^{(k)} \tag{2.7}$$

where

k = index of time step

$\bar{\mathbf{U}}^{(k-1)}$ = displacement vector at time step *k-1*

$\bar{\mathbf{U}}^{(k)}$ = displacement vector at time step *k*

$\bar{\mathbf{U}}^{(k+1)}$ = displacement vector at time step *k+1*

Δt = time step

Substituting Equation (2.5), (2.6) and (2.7) into Equation (2.4), one obtains

$$\mathbf{M}\frac{\bar{\mathbf{U}}^{(k+1)} - 2\bar{\mathbf{U}}^{(k)} + \bar{\mathbf{U}}^{(k-1)}}{\Delta t^2} + \bar{\mathbf{L}}\,\bar{\mathbf{U}}^{(k)} = \mathbf{F}^{(k)} \tag{2.8}$$

Equation (2.8) can be rewritten as

$$\bar{\mathbf{U}}^{(k+1)} = \mathbf{M}^{-1}(\mathbf{F}^{(k)}\Delta t^2 - \bar{\mathbf{L}}\,\bar{\mathbf{U}}^{(k)}\Delta t^2 + 2\bar{\mathbf{U}}^{(k)} - \bar{\mathbf{U}}^{(k-1)}) \tag{2.9}$$

Equation (2.9) provides an iterative process to find the displacement vector throughout the time steps. The initial conditions are

$$\bar{\mathbf{U}}^{(0)} = \bar{\mathbf{U}}_0 \tag{2.10}$$

$$\bar{\mathbf{U}}^{(1)} = \frac{1}{2}\mathbf{M}^{-1}(\mathbf{F}^{(0)}\Delta t^2 - \bar{\mathbf{L}}\,\bar{\mathbf{U}}_0\Delta t^2 + 2\bar{\mathbf{U}}_0 + 2\Delta t\,\bar{\mathbf{V}}_0) \tag{2.11}$$

where

$\bar{\mathbf{U}}_0$ = initial displacement

$\bar{\mathbf{V}}_0$ = initial velocity

In Equation (2.9), if the mass matrix **M** is diagonal, either because of a system with lumped masses, a spectral formulation of the finite element method, or a diagonalization of a full consistent mass matrix, there is no need for solving a set of simultaneous equations. In the other definition of the spectral finite element formulation described by Komatitsch and Tromp [37], the nodes and the integration quadrature points are specially designed, so that the consistent mass matrix is diagonal.

The term $\bar{\mathbf{L}}\bar{\mathbf{U}}$ represents the vector of internal elastic forces exerted on the nodes by the elements and involves in principle the global stiffness matrix. However, since the multiplication of the inverse of the mass matrix does not involve solving equations, there is no need to assemble the global matrix $\bar{\mathbf{L}}$ and multiply it by the displacement vector. One only needs to loop over all the elements and add each element's contribution to the elastic force acting on the nodes according to the connectivity table. This will reduce considerably the memory requirements especially when the number of nodes is large.

One issue associated with the explicit scheme is stability. The explicit scheme is conditionally stable. This condition, known as the C-F-L condition, relates the allowed time step with the element size.

2.5 The Exponential Window Method

2.5.1 The exponential window method in the frequency domain

To provide better understanding of the exponential window method in the wave number domain, the exponential window method in the frequency domain is discussed here. Consider the dynamics of the very simple system of a mass and a spring, a single degree freedom system initially at rest. The equation of motion is

$$m\frac{\partial^2 u}{\partial t^2} + ku = f \tag{2.12}$$

where

m = mass

k = spring coefficient

f = force

u = displacement

The equation in the frequency domain is

$$(k - m\omega^2)U = F \tag{2.13}$$

where

U = Fourier transform of the displacement

F = Fourier transform of the input force

The dynamic stiffness of the system in the frequency domain is

$$K = k - m\omega^2 \tag{2.14}$$

where

ω = frequency

Since K is a real number, the Fourier transforms of the input force and the displacement have no phase difference. This indicates that there is no damping in the system.

The displacement in the frequency domain can be easily obtained from Equation (2.13).

$$U = \frac{F}{k - m\omega^2} \tag{2.15}$$

Then the time response can be obtained performing an inverse Fourier transform.

The seemingly simple procedure described above has a catch. For example, consider the system with the following parameters. $m = 1.0kg$, $k = 1.0N/m$. The input force, with sinusoidal time history, is shown in Figure 2.1. The duration of the force is T_f, and the duration of the analysis is T_d. The response of the system is plotted with different ratios, of T_f and T_d. The results are compared with the exact solution as shown in Figure 2.2. It can be seen that the error in the solution by Equation (2.15) tends to be unrelated to the ratio. Taking longer analysis duration does not help to reduce the error. The exact solution was obtained using finite differences with very small time steps.

The reason behind this discrepancy is due to the periodic nature of the Discrete Fourier Transform (DFT), which matches the displacement and velocity conditions at the beginning and at the end of the duration. Thus the initial condition is violated if the system is not quiet at the end of the duration.

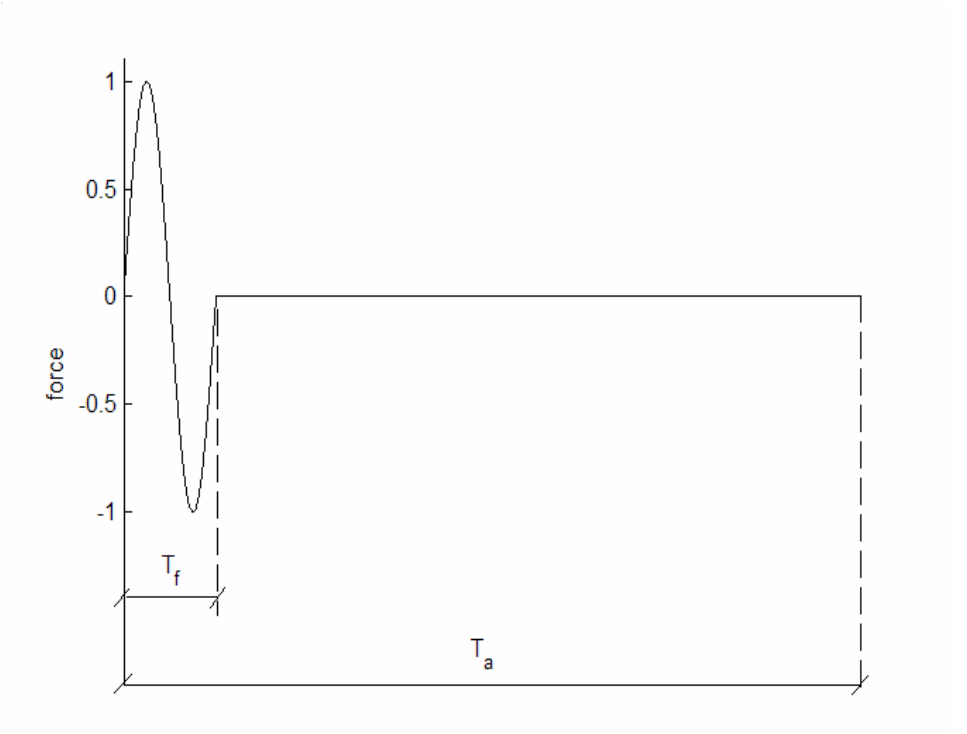

Figure 2.1 Time history of the sinusoidal input force

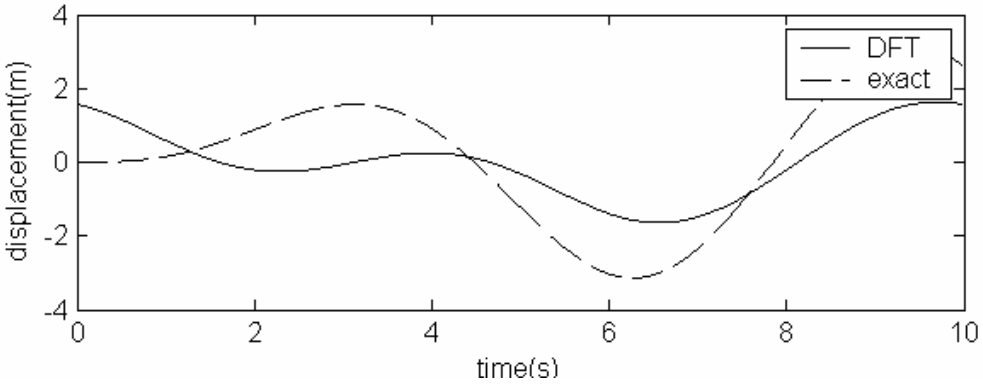

(a) $T_f = 6.28s$, $T_d = 10s$

Figure 2.2 Comparison of results with different analysis duration

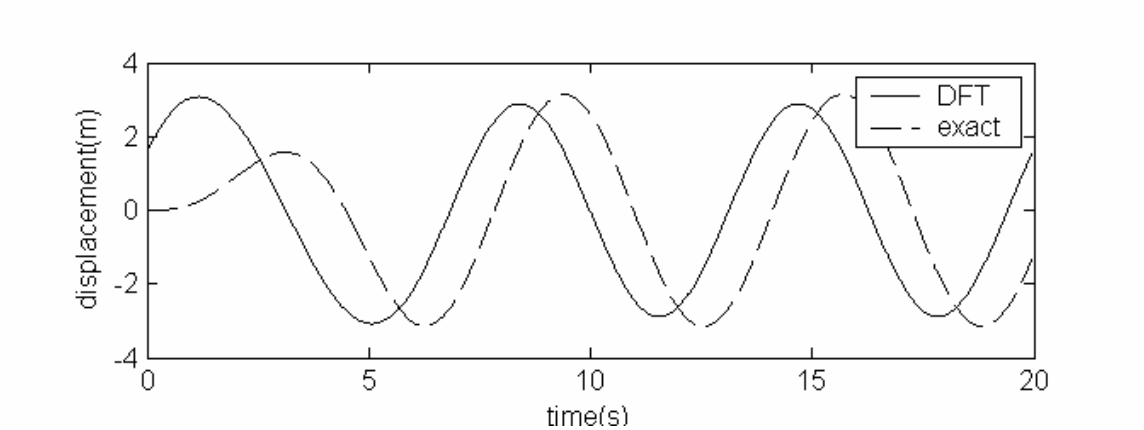

(b) $T_f = 6.28s$, $T_d = 20s$

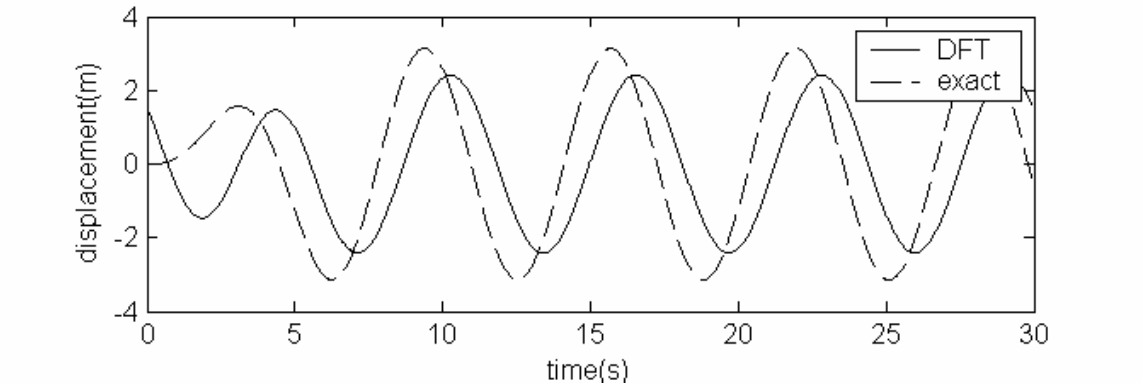

(c) $T_f = 6.28s$, $T_d = 30s$

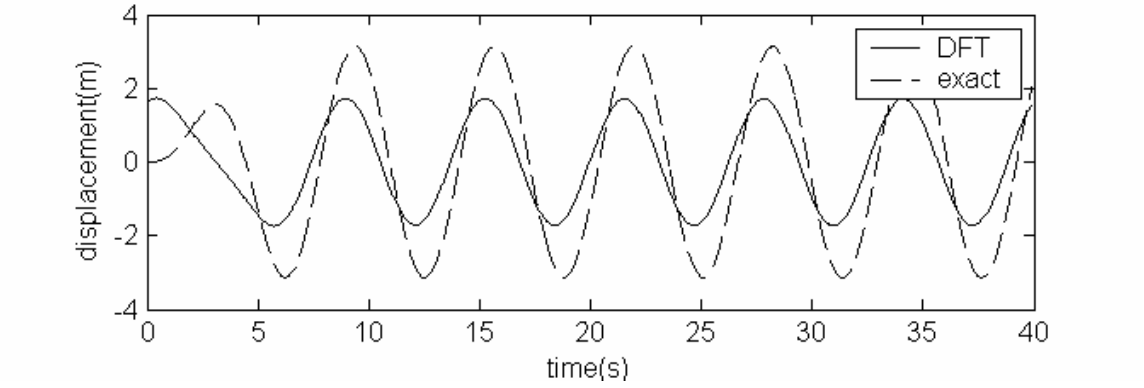

(d) $T_f = 6.28s$, $T_d = 40s$

Figure 2.2 Continued

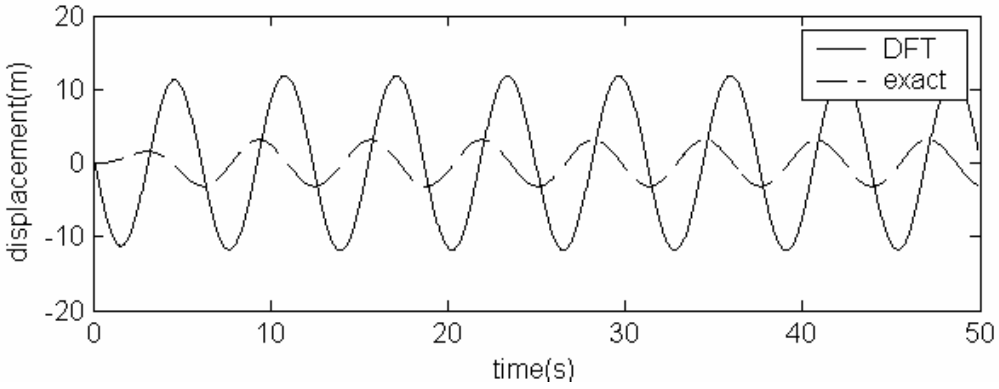

(e) $T_f = 6.28s$, $T_d = 50s$

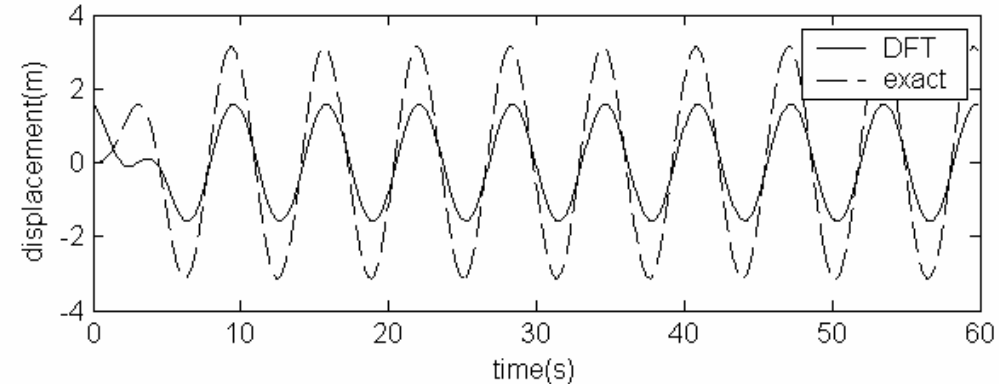

(e) $T_f = 6.28s$, $T_d = 60s$

Figure 2.2 Continued

Now consider the same system with the addition of a dashpot, the dynamic stiffness of this damped system is

$$K_d = k - m\omega^2 + jc \tag{2.16}$$

where

c = dashpot constant

The displacement in the frequency domain is

$$U = \frac{F}{k - m\omega^2 + jc} \tag{2.17}$$

The dynamic stiffness in (2.16) has an imaginary part, which results from the dashpot and indicates the existence of damping in the system. With damping, if the analysis duration is long enough, the vibration will damp out so that at the end of the duration, the conditions would be very close to the quiet condition. Therefore, one can expect that the results from the DFT would converge to the exact solution increasing the analysis duration. This is verified by the results shown in Figure 2.3 with the dashpot constant of *0.05Ns/m* and other system parameters the same.

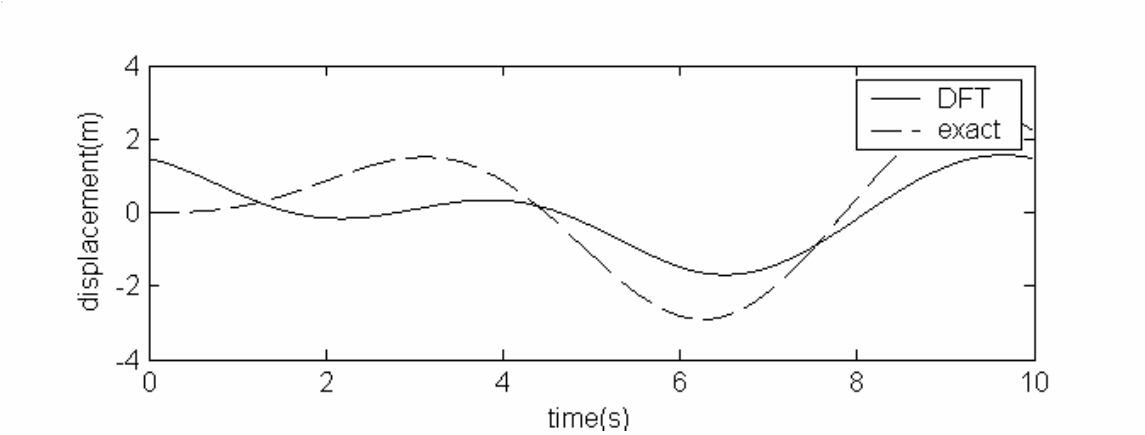

(a) $T_f = 6.28s$, $T_d = 10s$, $c=0.05Ns/m$

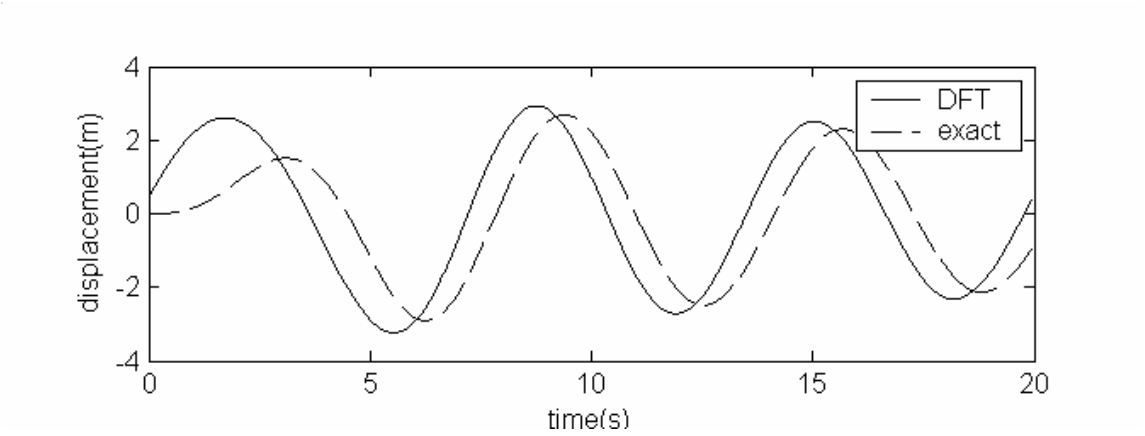

(b) $T_f = 6.28s$, $T_d = 20s$, $c=0.05Ns/m$

Figure 2.3 Results of different analysis duration with damping

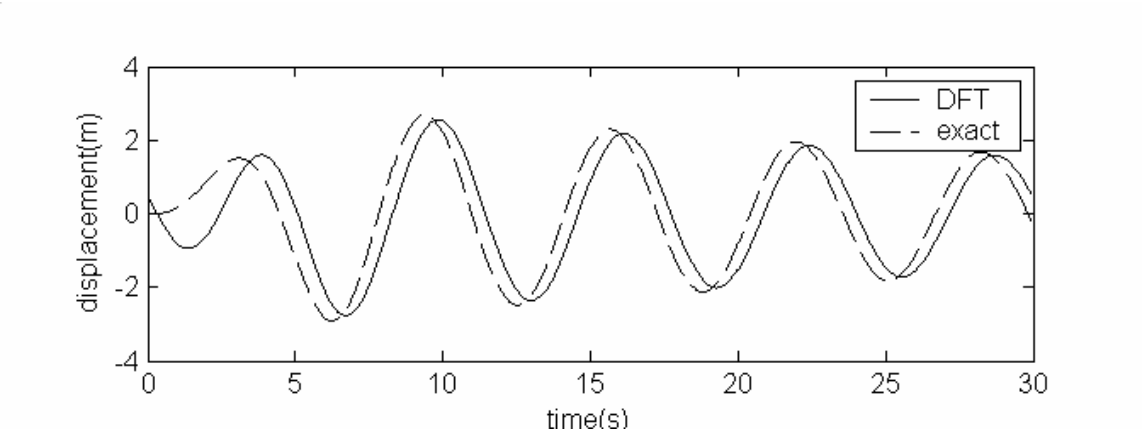

(c) $T_f = 6.28s$, $T_d = 30s$, $c=0.05Ns/m$

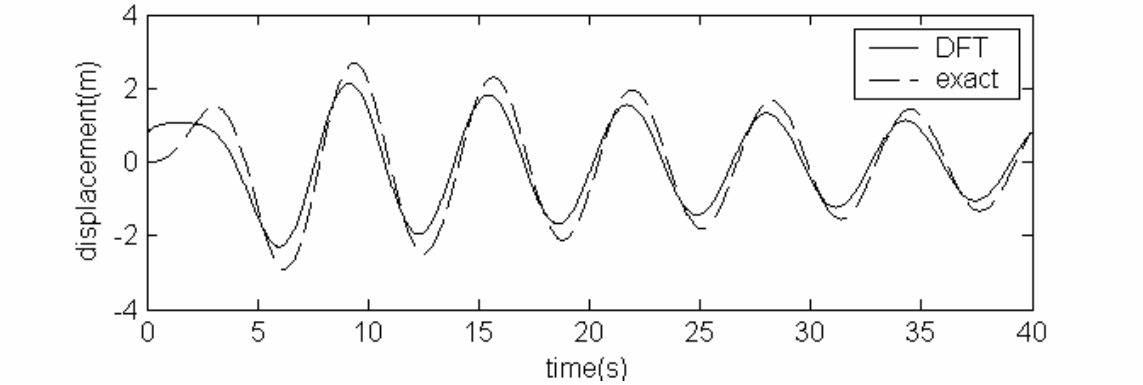

(d) $T_f = 6.28s$, $T_d = 40s$, $c=0.05Ns/m$

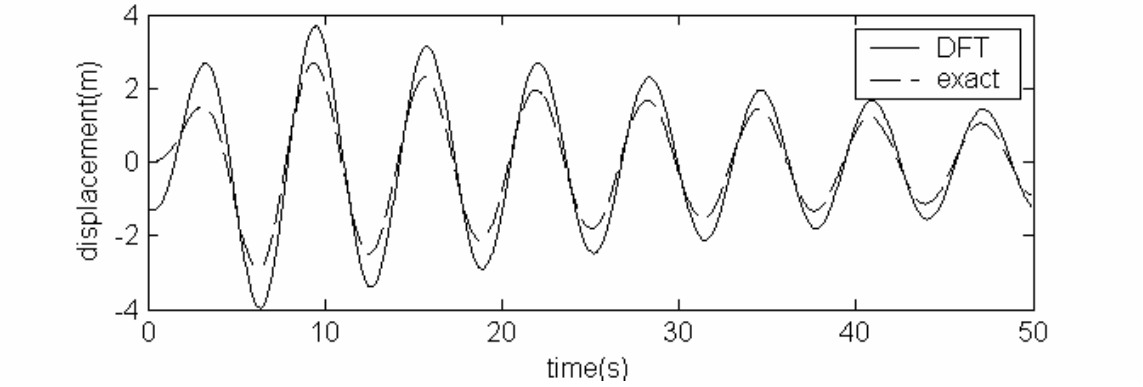

(e) $T_f = 6.28s$, $T_d = 50s$, $c=0.05Ns/m$

Figure 2.3 Continued

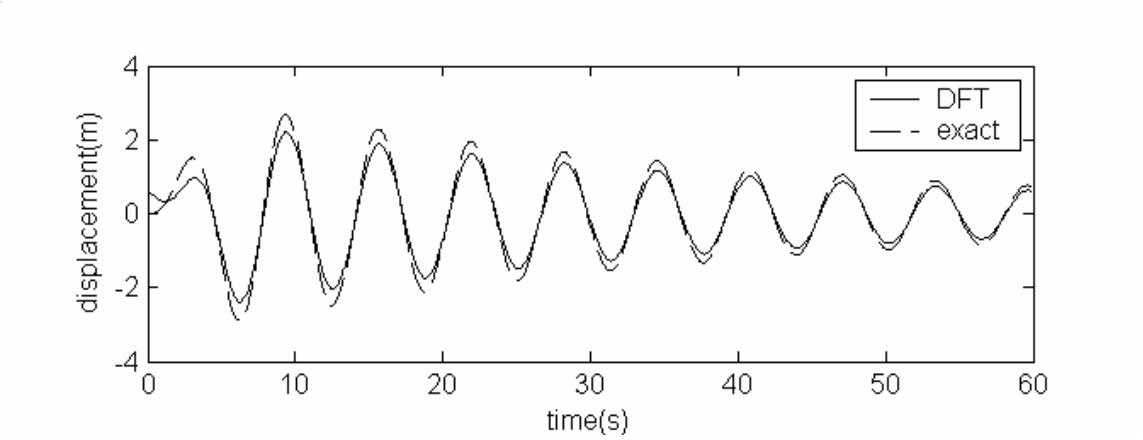

(f) $T_f = 6.28s$, $T_d = 60s$, $c=0.05Ns/m$

Figure 2.3 Continued

The conclusion from the above discussion is that if there is damping in the system, it is possible to find the correct results if the duration of analysis and the quiet zone, where the excitation force is zero, are long enough.

Applying to Equation (2.14), a complex frequency shift, $\omega' = \omega + jc_1$, one obtains

$$K = k - m(\omega' - jc_1)^2 = k - m\omega'^2 + mc_1^2 + j2mc_1\omega' \tag{2.18}$$

Comparing Equation (2.18) with Equation (2.16), one can see that Equation (2.18) corresponds to a damped system. Actually it is a system with mass *m*, the spring coefficient $k + mc_1^2$, and a dashpot $2mc_1\omega'$.

The force in the shifted system is

$$F_{shifted}(\omega) = F(\omega - jc) \tag{2.19}$$

In the time domain

$$f_{shifted}(t) = f(t)e^{-ct} \tag{2.20}$$

The displacement in the shifted system is

$$U_{shifted}(\omega) = U(\omega - jc) \tag{2.21}$$

In the time domain

$$u_{shifted}(t) = u(t)e^{-ct} \tag{2.22}$$

One can calculate $F_{shifted}(\omega)$ by imposing a decaying window on the input force before performing the DFT, and after $u_{shifted}(t)$ is obtained by performing an inverse DFT to $U_{shifted}(\omega)$, one can retrieve the response of the original system by imposing a rising window on $u_{shifted}(t)$.

Figure 2.4 shows the results using the exponential window method for the undamped system in Figure 2.2. The results are good regardless of the analysis duration. This means the location at which the analysis is cut does not matter. Alternatively it can be said that an open boundary in time is created. If the same procedure were to be carried out in space, one might expect that an open boundary in space would be created. In the next section, the potential application of the method in the space domain is discussed.

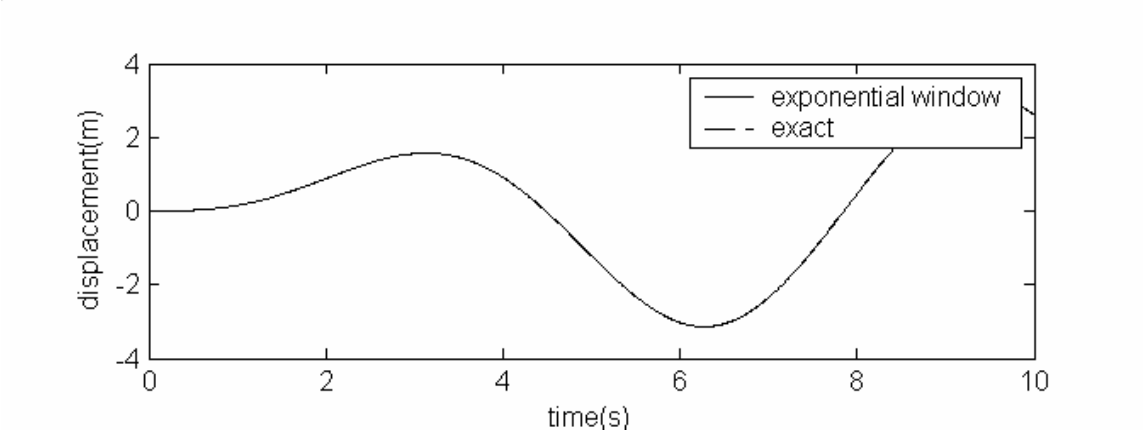

(a) $T_f = 6.28s$, $T_d = 10s$

Figure 2.4 Results from the exponential window method

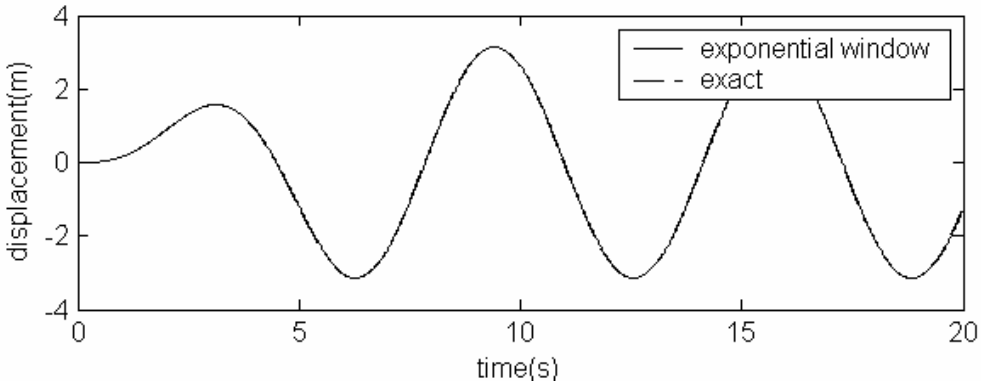

(b) $T_f = 6.28s$, $T_d = 20s$

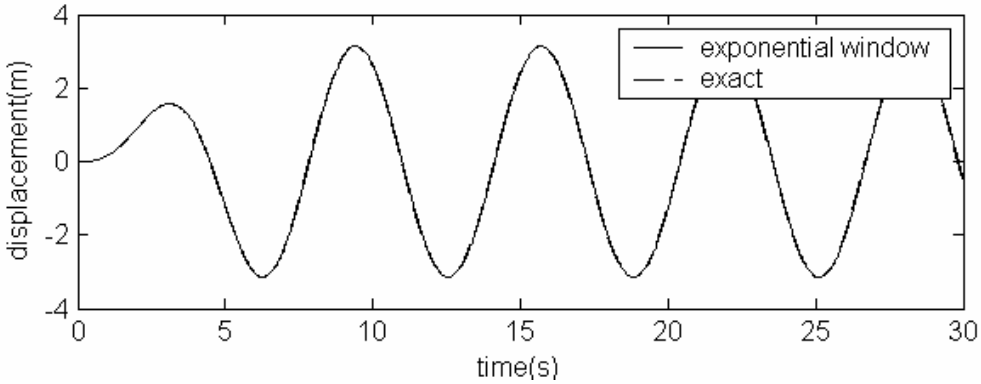

(c) $T_f = 6.28s$, $T_d = 30s$

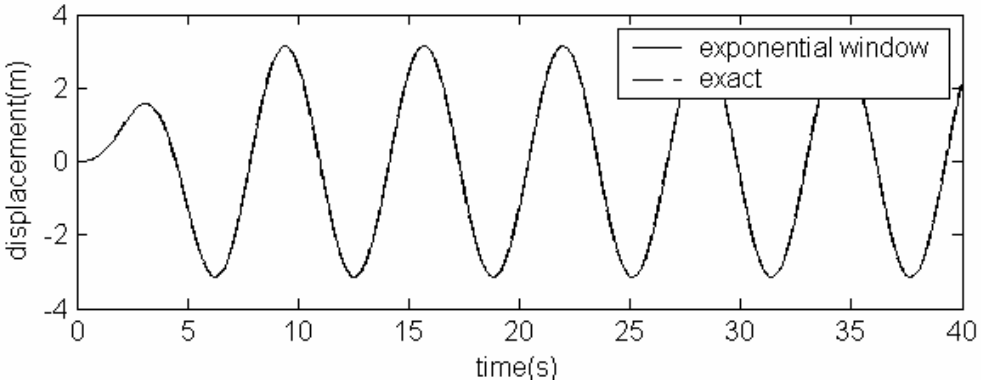

(b) $T_f = 6.28s$, $T_d = 40s$

Figure 2.4 Continued

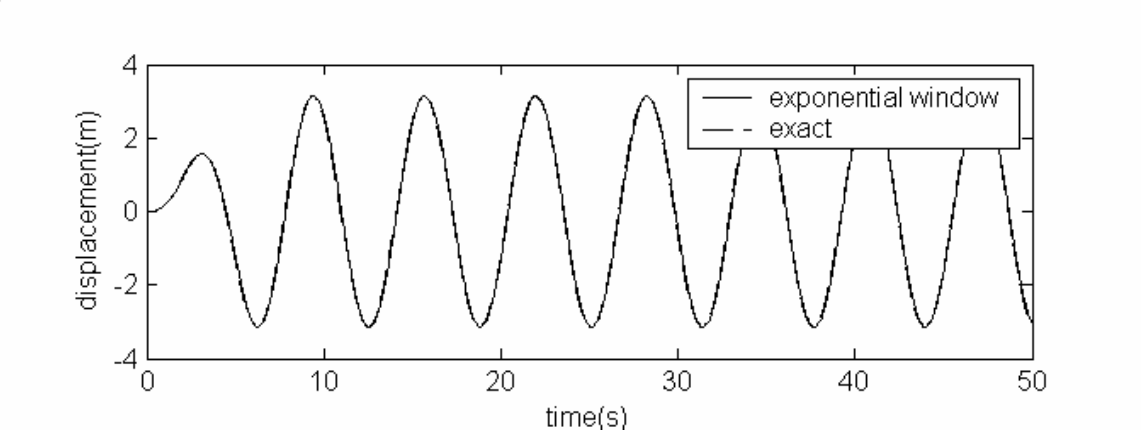

(e) $T_f = 6.28s$, $T_d = 50s$

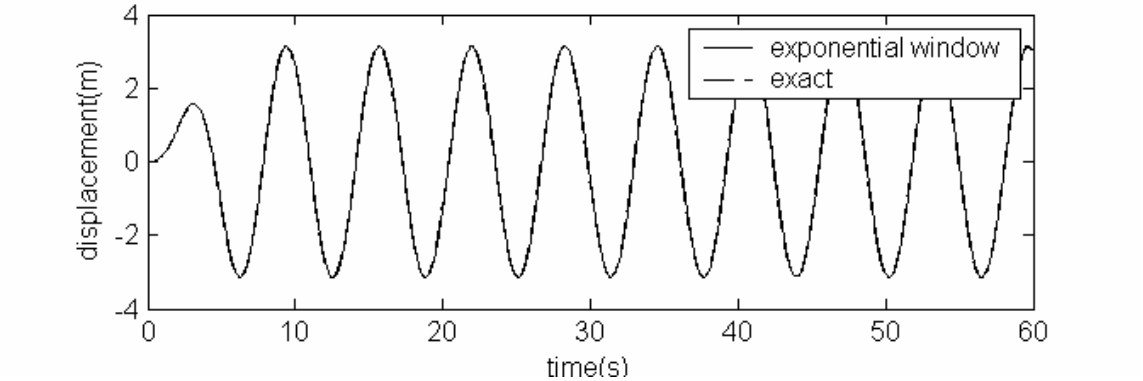

(f) $T_f = 6.28s$, $T_d = 60s$

Figure 2.4 Continued

2.5.2 Application of the complex wave number shift in the space domain

In this section, the concept of the exponential window for the solution of dynamic problems in the frequency domain is extended to the formulation of dynamic problems in the space domain. The expectation is that performing a complex wave number shift in space might help to generate good results regardless of the location where the model is cut, or alternatively, that it could lead to an open boundary in the space domain.

Setting the following for the three dimensional wave propagation problem:

$m = m' - jc_1$

$$n = n' - jc_2$$

$$l = l' - jc_3$$

the following equation is obtained.

$$\mathbf{M}\frac{\partial^2 \bar{\mathbf{U}}(m' - jc_1, n' - jc_2, l' - jc_3, t)}{\partial t^2} + \bar{\mathbf{L}}(m' - jc_1, n' - jc_1, l' - jc_1) \times \bar{\mathbf{U}}(m' - jc_1, n' - jc_1, l' - jc_1, t) = \bar{\mathbf{F}}(m' - jc_1, n' - jc_1, l' - jc_1, t) \tag{2.23}$$

The new equation (2.23) is in terms of the shifted wave numbers m', n', and l'. The primary difference between Equation (2.23) and Equation (2.4) lies in the change of matrix $\bar{\mathbf{L}}$, that is actually the "dynamic stiffness matrix" in the wave number domain. In Equation (2.4), the entries in $\bar{\mathbf{L}}$ are all real numbers if the original equation of motion contains only even number order derivatives. The entries in $\bar{\mathbf{L}}$ may be complex if the original equation of motion contains odd number order derivatives. In both cases, however, the structure of the entries of $\bar{\mathbf{L}}$ does not reflect the existence of damping if the original equation of motion contains no damping.

With the complex wave number shifting, the structure of the entries of $\bar{\mathbf{L}}$ changes. Due to the introduction of $-jc_1$, $-jc_2$, and $-jc_3$, damping is added to the original system. Then Equation (2.23) can perhaps be solved correctly by the DFT and the inverse DFT.

What is left is to apply the exponential window to the force and displacement. The force in the shifted system is

$$\bar{\mathbf{F}}_{shifted}(m, n, l) = \bar{\mathbf{F}}(m - jc_1, n - jc_2, l - jc_3) \tag{2.24}$$

In the space domain

$$\mathbf{F}_{shifted}(x, y, z) = \mathbf{F}(x, y, z)e^{-c_1 x - c_2 y - c_3 z} \tag{2.25}$$

The displacement in the shifted system is

$$\bar{\mathbf{U}}_{shifted}(m, n, l) = \bar{\mathbf{U}}(m - jc_1, n - jc_2, l - jc_3) \tag{2.26}$$

In the time domain

$$\mathbf{U}_{shifted}(x, y, z) = \mathbf{U}(x, y, z)e^{-c_1 x - c_2 y - c_3 z} \tag{2.27}$$

Equation (2.25) means that a decaying window is applied to the input force before it is transformed to the wave number domain. Equation (2.27) indicates that the response in the original system can be retrieved by applying a rising window after the response in the shifted system is obtained.

2.6 Issues to Consider

In the above discussion, an analogy between time and space was used to explain the concept. However, time and space are not completely equivalent. There are two issues that must be considered.

One issue is associated with the causal nature of time. Motion can "propagate" in only one direction, which is the positive direction, in the time domain. But in the space domain, waves can propagate in both positive and negative directions. If a uniform window is applied over the entire range, only wave motion in the positive direction would be properly simulated and the simulated wave in the negative direction would be incorrectly modeled. Rather than decaying, in the negative direction, the fictitious damping would actually "boost" the motion and thus lead to a blowout. There are two possible ways to deal with this situation. First, by intuition, a two-segment window can be designed with a decaying exponential window imposed in the positive direction and a rising exponential window imposed in the negative direction. Second, if a symmetric problem is to be analyzed, only the wave propagating in the positive direction needs to be studied and the wave propagating in the other direction is just a mirror image.

The other issue is associated with the conjugate symmetry property of the Fourier transform. Since the solution to the equation of motion is real, the DFT of the displacements is conjugate symmetric with respect to the Nyquist frequency, or Nyquist wave number in this case. The property needs be applied in the DFT since the results from DFT above the Nyquist wave number only carry spurious frequency contents and

should not be used. It is easy to apply this property in a one dimensional DFT, but in a two dimensional DFT, needed in three-dimensional problems, some special consideration is needed when the exponential window is implemented. This will be explained in detail in later chapters.

CHAPTER III

INFINITE BEAM ON ELASTIC FOUNDATION-1D APPLICATION

3.1 Overview

The study of an infinite beam on an elastic foundation as shown in Figure 3.1 has a long history documented in the literature. It can be used to model different problems where moving loads on a structure with a dominant longitudinal dimension are involved. To name just a few, Timoshenko was the first to model a moving load of constant velocity on a railway [38]. To account for high frequencies associated with high speed moving loads, Achenbach and Sun [39] used a Timoshenko beam rather than the Euler-Bernoulli beam. Kim and Roesset investigated the effects of moving loads on pavements through the dynamic stiffness approach [40]. In the early days, investigators attacked the problem analytically so they were able to deal with the infinity condition well. As more complicated models were developed and numerical methods became popular, a procedure to enforce numerically the condition at infinity became necessary. To the author's knowledge, the existing numerical methods have not really addressed the infinity problem. It is circumvented because the existence of damping in real applications eliminates the need for an absorbing boundary if an appropriate length of the model is chosen.

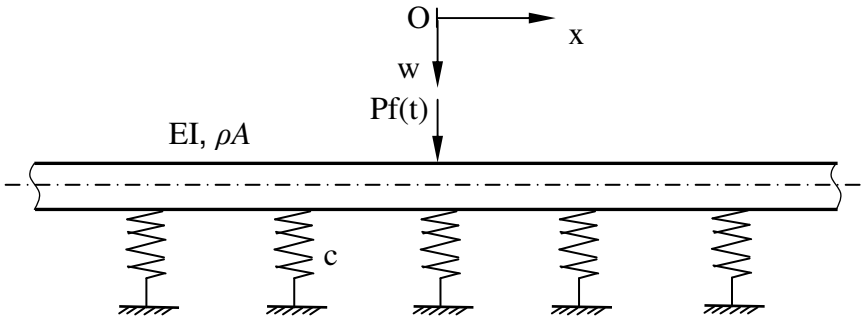

Figure 3.1 An infinitely long beam on elastic foundation

In this chapter, the proposed method is applied to an infinite beam on an elastic foundation. The steady state response of the beam is studied both analytically and numerically with the exponential window imposed. The results with different frequencies and truncated lengths are compared. The conjugate symmetry property of the Fourier transform and its application in elastodynamic problems using frequency domain methods are discussed. The impact of damping on the implementation of the symmetry property is explained and an alternative or more general approach is presented. The transient response of the same beam under a triangular pulse load is also studied in the time-wave number domain. The effectiveness of the exponential window in this case is examined by comparing the results with and without the exponential window.

3.2 Analytical Solution of Steady State Response

In this section, the steady state response of an undamped infinite beam on elastic foundation subject to a harmonic load is studied. The reason to study the steady state response is that the solution can be obtained analytically and the numerical accuracy of the proposed method can be examined.

The equation of motion of the beam in Figure 3.1 is [36]

$$EI\frac{\partial^4 w(x,t)}{\partial x^4} + cw(x,t) - \rho A\frac{\partial^2 w}{\partial t^2} = Pf(t)\delta(x) \tag{3.1}$$

where

w = deflection of the beam

EI = bending stiffness

ρA = mass per unit length

c = elastic constant of the foundation

P = magnitude of the applied force

$f(t)$ = time history of the applied force

$\delta(x)$ = Dirac delta function

The steady state response to a harmonic applied force, $f(t) = e^{j\Omega t}$ can be obtained by substituting $w(x,t) = W(x,\Omega)e^{j\Omega t}$ into Equation (3.1). Then

$$EI\frac{\partial^4 W(x,\Omega)}{\partial x^4} + (c - \rho A\Omega^2)W(x,\Omega) = P\delta(x) \tag{3.2}$$

where $W(x,\Omega)$ is the Fourier transform with respect to time.

Equation (3.2) is an ordinary differential equation with respect to space only. To solve it, its modes must be found first. If $\rho A\Omega^2 - c > 0$, calling $\alpha^4 = \frac{\rho A\Omega^2 - c}{EI}$ with $\alpha > 0$, the characteristic equation is

$$r^4 - \alpha^4 = 0 \tag{3.3a}$$

the modes are $e^{j\alpha x}$, $e^{-j\alpha x}$, $e^{\alpha x}$ and $e^{-\alpha x}$. The first two modes correspond to propagating waves in both directions and the other two modes correspond to evanescent waves in both directions. If $\rho A\Omega^2 - c < 0$, calling $\alpha^4 = \frac{c - \rho A\Omega^2}{EI}$ with $\alpha > 0$, the characteristic equation is

$$r^4 + \alpha^4 = 0 \tag{3.3b}$$

The modes are then $e^{r_1 x}, e^{r_2 x}, e^{r_3 x}$ and $e^{r_4 x}$ with $r_1 = \frac{\sqrt{2}\alpha}{2} + j\frac{\sqrt{2}\alpha}{2}$, $r_2 = -\frac{\sqrt{2}\alpha}{2} + j\frac{\sqrt{2}\alpha}{2}$, $r_3 = \frac{\sqrt{2}\alpha}{2} - j\frac{\sqrt{2}\alpha}{2}$ and $r_4 = -\frac{\sqrt{2}\alpha}{2} - j\frac{\sqrt{2}\alpha}{2}$. The first two modes correspond to propagating waves in the positive *x* direction and the other two to propagating waves in the negative *x* direction.

To solve Equation (3.2) directly requires finding a particular solution to the Dirac delta function on the right hand side. It is easy to take advantage of symmetry and to divide the beam into two halves at the location of the applied force as shown in Figure 3.2. The small segment in the middle is of differential length. For the segments on the left and right, there will be no applied force, so the particular solution would be trivial. Then the solution of the homogeneous equation is the general solution for each segment.

Meanwhile the continuity at the origin has to be satisfied, which provides the following boundary conditions.

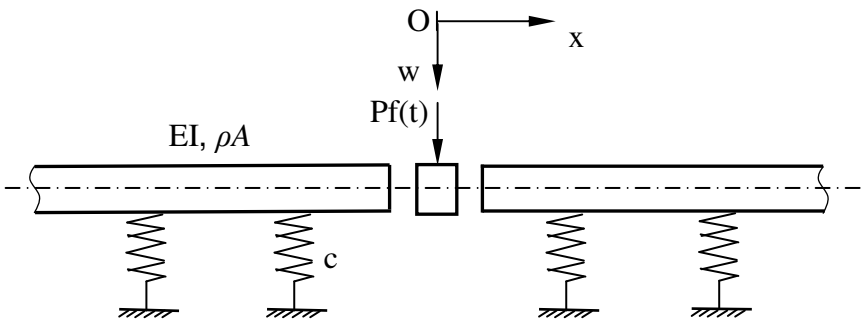

Figure 3.2 Segmentation of the beam

$$x \to +\infty, W_r(x) \text{ is finite} \tag{3.4a}$$

$$x \to -\infty, W_l(x) \text{ is finite} \tag{3.4b}$$

$$W_r(0^+) = W_l(0^-) \tag{3.4c}$$

$$\frac{\partial W_r}{\partial x}(0^+) = \frac{\partial W_l}{\partial x}(0^-) \tag{3.4d}$$

$$\frac{\partial^2 W_r}{\partial x^2}(0^+) = \frac{\partial^2 W_l}{\partial x^2}(0^-) \tag{3.4e}$$

$$EI\frac{\partial^3 W_r}{\partial x^3}(0^+) = EI\frac{\partial^3 W_l}{\partial x^3}(0^-) + P \tag{3.4f}$$

When $\rho A\Omega^2 - c > 0$, since the segment on the left runs to infinity, according to Summerfeld's radiation condition, its solution should not include the $e^{-j(\alpha x - \Omega t)}$ term, which represents wave propagating to the right. Similarly, the solution for the segment on the right should not include a term $e^{j(\alpha x + \Omega t)}$. After these conditions are considered, the solution is found to be

$$W_r = -\frac{P}{4\alpha^3 EI}e^{-\alpha x} - \frac{P}{j4\alpha^3 EI}e^{-j\alpha x}(x > 0) \tag{3.5a}$$

$$W_l = -\frac{P}{4\alpha^3 EI} e^{\alpha x} - \frac{P}{j4\alpha^3 EI} e^{j\alpha x} (x < 0) \tag{3.5b}$$

It should be noticed that in this case the solution is complex. The points along the beam are not vibrating in phase and there are waves propagating with a velocity Ω/α. The amplitude of the vibrations is $\frac{P}{4\alpha^3 EI}\sqrt{2+2\sin(\alpha x)e^{-\alpha x}+e^{-2\alpha x}}$. When $\rho A\Omega^2 - c < 0$, the solution for the segment on the right should include only those modes decaying in the positive x direction, i.e., modes with negative real part. Similarly the solution for the segment on the left should include modes decaying in the negative x direction, i.e., modes with positive real part. The solution is found to be

$$W_r = \frac{P}{4r_2^3 EI} e^{r_2 x} + \frac{P}{4r_4^3 EI} e^{r_4 x} = \frac{\sqrt{2}P}{4EI\alpha^3} e^{-\frac{\sqrt{2}}{2}\alpha x} (\cos(\frac{\sqrt{2}}{2}\alpha x) + \sin(\frac{\sqrt{2}}{2}\alpha x))(x > 0) \tag{3.5c}$$

$$W_l = -\frac{P}{4r_1^3 EI} e^{r_1 x} - \frac{P}{4r_3^3 EI} e^{r_3 x} = \frac{\sqrt{2}P}{4EI\alpha^3} e^{-\frac{\sqrt{2}}{2}\alpha x} (\cos(\frac{\sqrt{2}}{2}\alpha x) - \sin(\frac{\sqrt{2}}{2}\alpha x))(x < 0) \tag{3.5d}$$

It is clear that on each side of the load, there are two modes in either case so there are four constants and these constants can be determined by applying conditions (3.4c) through (3.4f). It should be noticed that in this case the solution is real and all points along the beam would be vibrating in phase. There are no waves propagating.

3.3 Steady State Response with Exponential Windows

The solution to Equation (3.2) can be found numerically by truncating the beam to a finite length L and performing the DFT with respect to x. Since the original beam is infinitely long, the exponential window must be imposed (Figure 3.3).

Performing the Fourier transform of Equation (3.2) with respect to x, one obtains

$$EIk^4 \tilde{W}(k,\Omega) + (c - \rho A\Omega^2)\tilde{W}(k,\Omega) = \tilde{P}(k) \tag{3.6}$$

where

k = the wave number

$\tilde{W}$ = the displacement in the wave number domain.

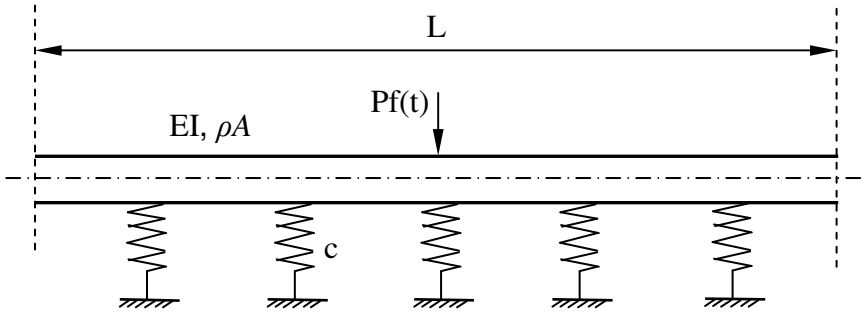

Figure 3.3 The truncated beam

The complex wave number shift is $k = k' - j\beta$.

$$EI(k' - j\beta)^4 \tilde{W}_s(k' - j\beta, \Omega) + (c - \rho A\Omega^2)\tilde{W}_s(k' - j\beta, \Omega) = \tilde{P}_s(k' - j\beta) \tag{3.7}$$

where

$\tilde{W}_s$ = displacement in the shifted wave number domain

$\tilde{P}_s$ = force in the shifted wave number domain

From (3.7), $\tilde{W}_s$ can be obtained

$$\tilde{W}_s = \frac{\tilde{P}_s}{EI(k' - j\beta)^4 + c - \rho A\Omega^2} \tag{3.8}$$

The displacement in the space domain for the shifted system can be obtained by applying the inverse Fourier transform to Equation (3.8). The displacement of the original system is retrieved by imposing finally the rising exponential window.

$$W = W_s e^{\beta x} \tag{3.9}$$

3.4 Comparison of Steady State Results

The steady state responses obtained by the analytical and the numerical solutions are shown in Figures 3.4 to 3.7. Different excitation frequencies, and truncated lengths were used to verify the effectiveness of the exponential window. As a comparison, the results from the solution without the exponential window are also included. The parameters are $EI = 1.0$, $\rho A = 10.0$, and $c = 500.0$. The different frequencies are *0.1Hz*, *0.5Hz*, *1.5Hz* and *2.5Hz*. The different lengths are *5.12m*, *10.24m* and *20.48m*.

Several observations can be made from these results. First, there exists a threshold excitation frequency below which propagation does not happen and above which motion can propagate. The threshold frequency is the fundamental natural frequency $\sqrt{\frac{c}{\rho A}}$, where c is the stiffness per unit length of the foundation and ρA is the mass per unit length of the beam. At the threshold frequency, the beam is vibrating in resonance on the elastic foundation like a rigid body. The motion decreases rapidly in amplitude if the excitation frequency is lower than the threshold frequency. The motion spreads out if the frequency is higher than the threshold frequency.

Second, when the excitation frequency is lower than the threshold frequency, the results from the solution without imposing the exponential window are very good as shown in Figures 3.4 and 3.5. On the other hand, the results with the exponential window exhibit small numerical errors in the vicinity of the boundary for small lengths of the truncated domain. When the length of the truncated domain increases, the error tends to disappear. This phenomenon is observed again when natural or physical damping is introduced in the system. In this case, the length of the truncated domain needs to be carefully selected.

Finally, when the excitation frequency is higher than the threshold frequency, the results with the exponential window match the analytical solution very well, regardless of the excitation frequency and the truncated length. The results from the solution without the exponential window are quite random and generally do not match the

analytical solution. This means that the suggested procedure works very well. It is interesting to notice that as the length of the truncated domain increases the possible convergence of the results without exponential window, if it exists, is not monotonic. The results seem to be better at times for the smallest length than for the longer ones.

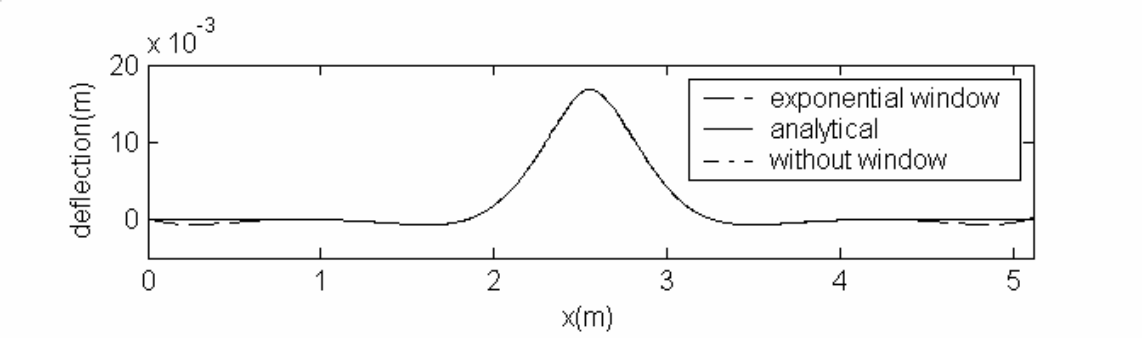

(a) length = 5.12m

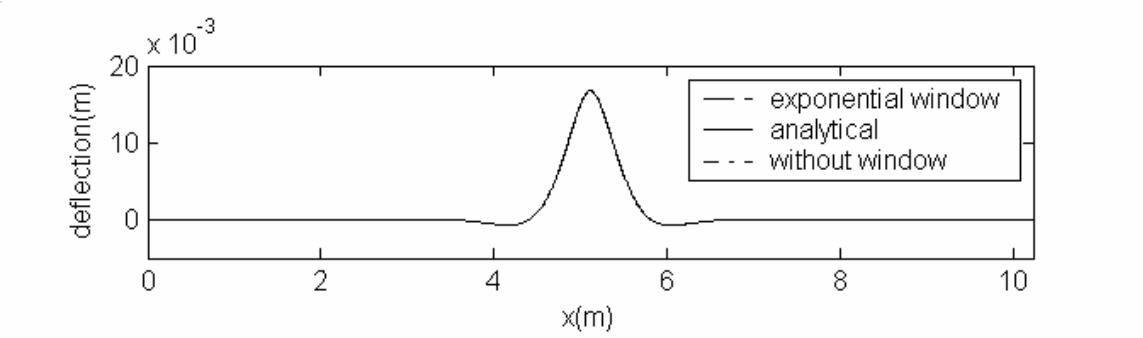

(b) length = 10.24m

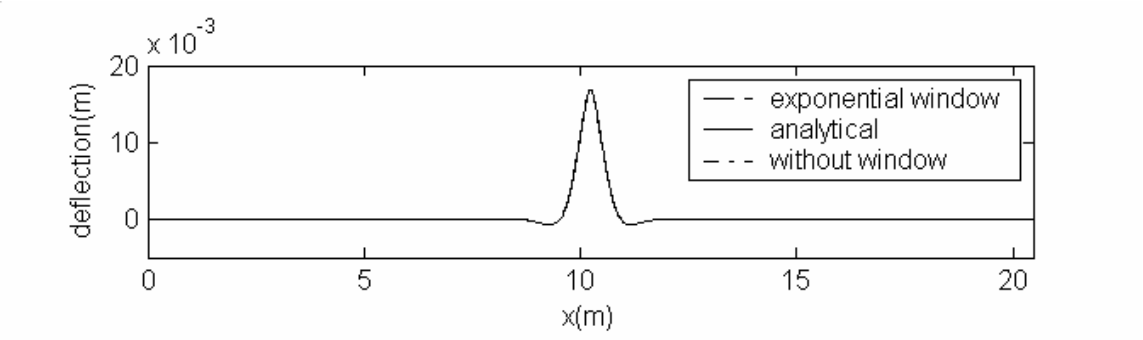

(c) length = 20.48m

Figure 3.4 Results with excitation frequency of 0.1Hz

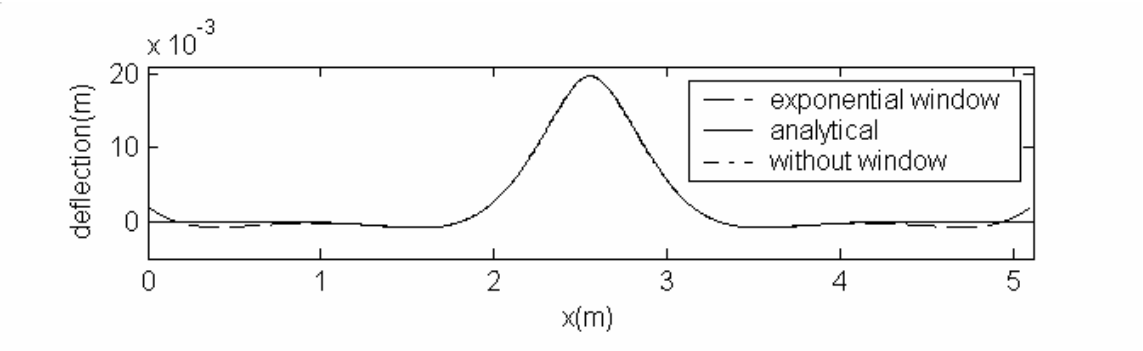

(a) length = 5.12m

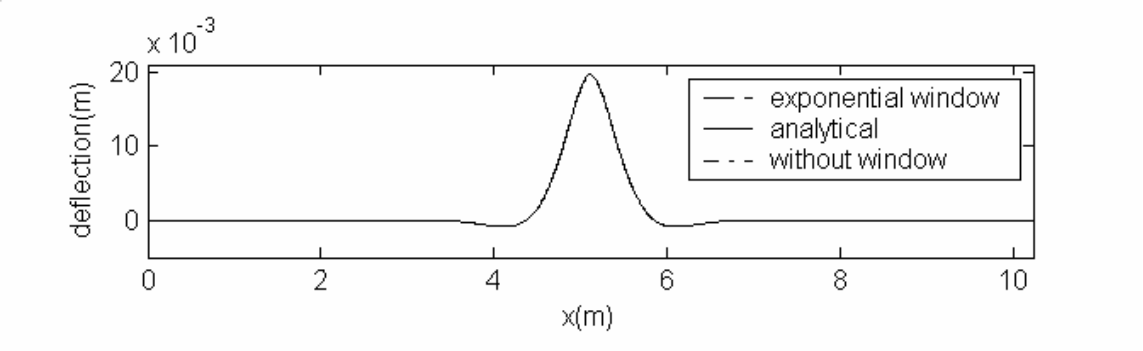

(b) length = 10.24m

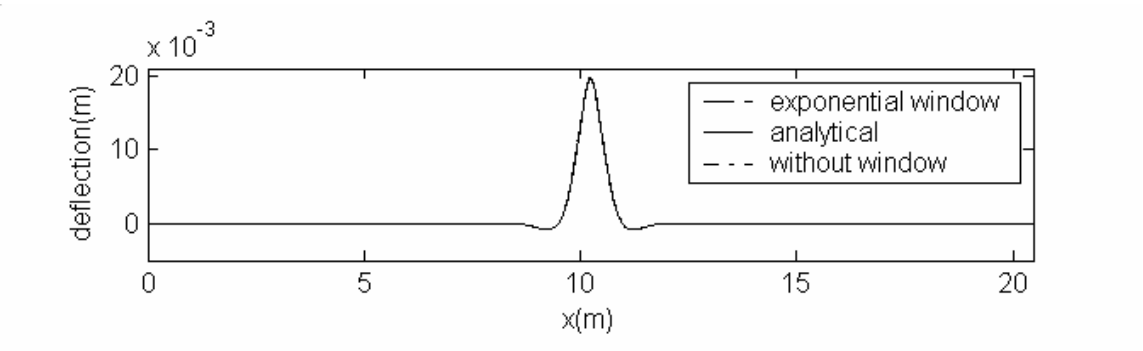

(c) length = 20.48m

Figure 3.5 Results with excitation frequency of 0.5Hz

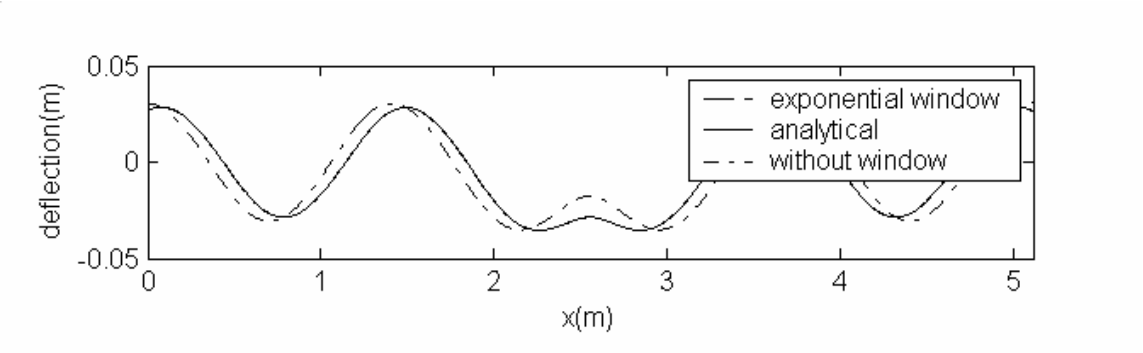

(a) length = 5.12m

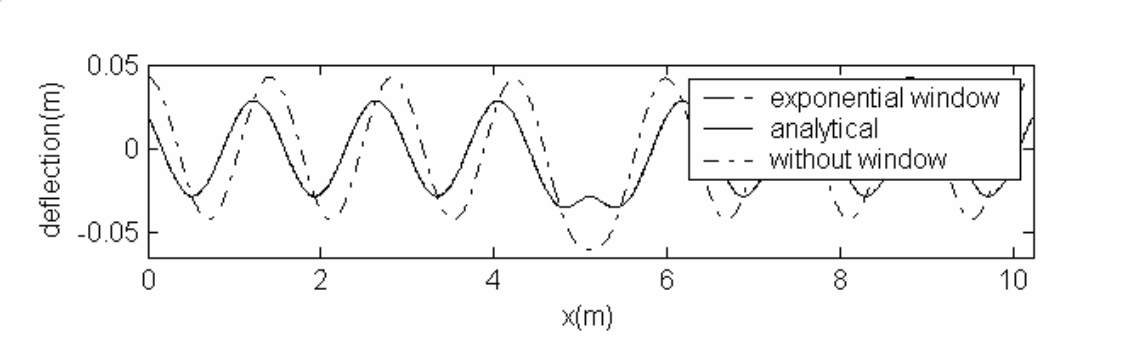

(b) length = 10.24m

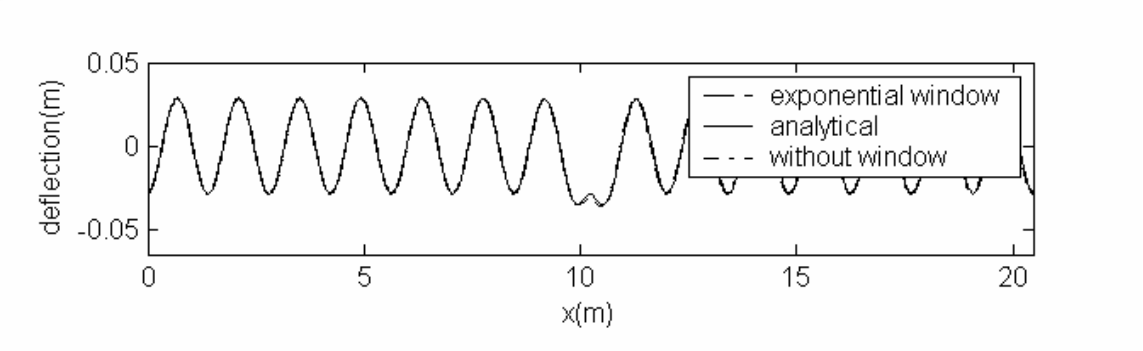

(c) length = 20.48m

Figure 3.6 Results with excitation frequency of 1.5Hz

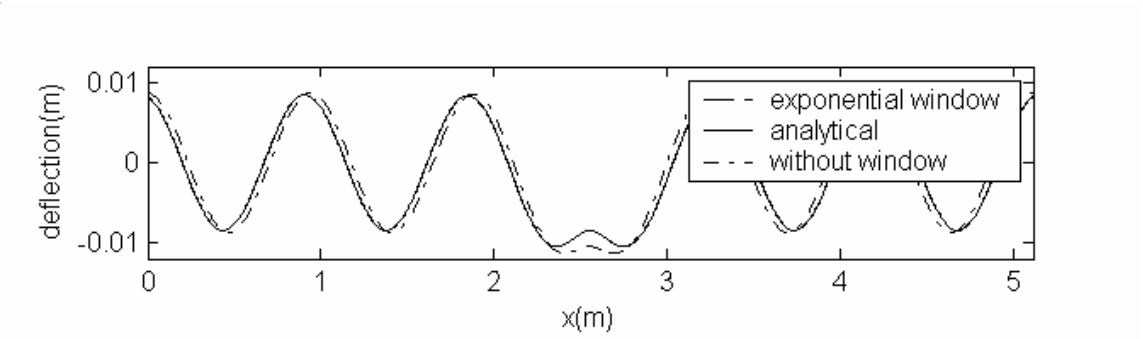

(a) length = 5.12m

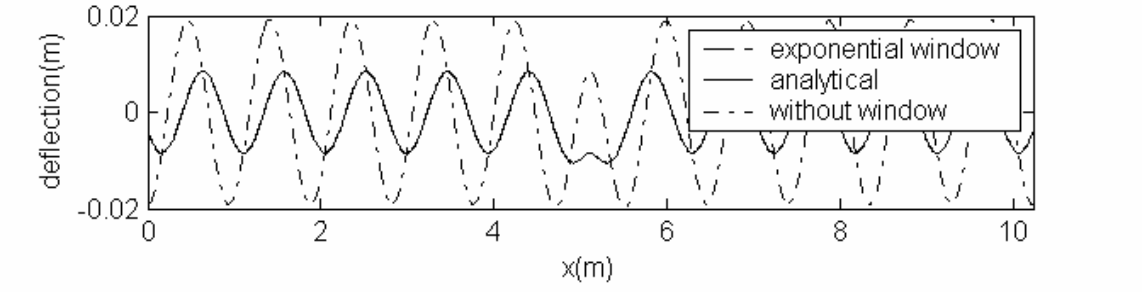

(b) length = 10.24m

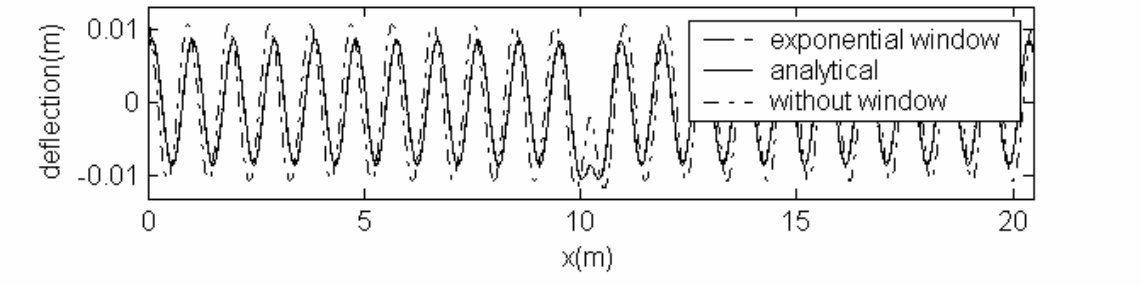

(c) length = 20.48m

Figure 3.7 Results with excitation frequency of 2.5Hz

3.5 Further Discussion on the Steady State Response

3.5.1 The conjugate symmetry of the Fourier transform

A point that deserves some consideration is associated with the conjugate symmetry property of the Fourier transform of a real function or the Discrete Fourier transform of a real array.

Consider the Fourier transform pair

$$F(\omega) = \int_{-\infty}^{\infty} f(t) e^{-j\omega t} dt \tag{3.10a}$$

$$f(t) = \int_{-\infty}^{\infty} F(\omega) e^{j\omega t} d\omega \tag{3.10b}$$

If *f(t)* is a real function, then from (3.10a),

$$F(-\omega) = \int_{-\infty}^{\infty} f(t) e^{j\omega t} dt = conj(\int_{-\infty}^{\infty} f(t) e^{-j\omega t} dt) = conj(F(\omega)) \tag{3.11}$$

where

conj( ) = conjugate operation

For a real function, its Fourier transform is conjugate symmetric with respect to the origin.

Consider the Discrete Fourier Transform pair

$$X(k) = \sum_{n=0}^{N-1} x(n) e^{-j2\pi kn/N}, k = 0,1,2,...,N-1 \tag{3.12a}$$

$$x(n) = \frac{1}{N} \sum_{k=0}^{N-1} X(k) e^{-j2\pi kn/N}, n = 0,1,2,...,N-1 \tag{3.12b}$$

If *x(n)* is a real sequence, then from (3.12a),

$$\begin{aligned} X(N-k) &= \sum_{n=0}^{N-1} x(n) e^{-j2\pi(N-k)n/N} = \sum_{n=0}^{N-1} x(n) e^{j2\pi kn/N} \\ &= conj(\sum_{n=0}^{N-1} x(n) e^{-j2\pi kn/N}) = conj(X(k)) \end{aligned} \tag{3.13}$$

Thus for a real sequence, the Discrete Fourier Transform is conjugate symmetric with respect to the point indexed by *N/2*, where the Nyquist frequency is located.

The conjugate symmetric property of the Fourier transform has an important implication when the Discrete Fourier Transform is used to solve an elastodynamic equation. In an elastodynamic equation, the input force is always real. In the absence of damping, the displacement must be real too. Then the Discrete Fourier Transform of both the input force and the displacement must be conjugate symmetric with respect to the Nyquist frequency, which implies that the transfer function or the dynamic stiffness must also be conjugate symmetric with respect to the Nyquist frequency. In practice, only the dynamic stiffness values corresponding to frequencies lower than the Nyquist frequency have to be calculated. For frequencies higher than the Nyquist frequency, the conjugate symmetric property is applied to obtain the dynamic stiffness. Alternatively, this property is applied directly to the displacement in the frequency domain. This is not only convenient, but also correct.

Looking at this point from another angle, the Nyquist frequency defines the highest frequency in a discrete sequence that can be correctly represented in its Discrete Fourier Transform. Above the Nyquist frequency, aliasing occurs and the results are meaningless [41]. Therefore it would be incorrect to calculate the dynamic stiffness values corresponding to frequencies above the Nyquist frequency by directly substituting the frequency into the expression of the dynamic stiffness.

The above argument applies to the wave number domain just as it does to the frequency domain. So in the following discussion, one should keep in mind that the term "frequency" is used to represent both frequency and wave number. However, the above argument applies only when there is no damping in the system. With damping, the solution by the frequency domain method should be complex to represent a phase difference, which reflects the existence of damping. In this case, the displacement in the frequency domain, as expected, is no longer conjugate symmetric with respect to the Nyquist frequency while aliasing still exists above the Nyquist frequency. One needs to consider an alternative to the approach based on the conjugate symmetry property.

3.5.2 The impact of damping

As argued in the previous subsection, one should not apply the conjugate symmetry property when damping exists. In this case, the method to calculate the dynamic stiffness above the Nyquist frequency must be modified as follows.

Assume the duration of analysis is *T*, and the number of points used in the Discrete Fourier Transform is *N*. The equation in the frequency domain is

$$\mathbf{K}_i \mathbf{U}_i = \mathbf{F}_i \tag{3.14}$$

where

i = the index of frequencies: $\omega_i = i/T$, *i = 1, 2, N*.

$\mathbf{K}_i$ = the dynamic stiffness corresponding to the i-th frequency.

$\mathbf{F}_i$ = the DFT of input force

$\mathbf{U}_i$ = the DFT of the displacement

Assume the dynamic stiffness of the system is **K**. The dynamic stiffness corresponding to the i-th frequency is

$$\mathbf{K}_i = \begin{cases} \mathbf{K}(\omega_i), & i <= N/2 \\ \mathbf{K}(-\omega_{N-i}), & i > N/2 \end{cases} \tag{3.15}$$

The validity of Equation (3.15) is based on the original definition of the Discrete Fourier Transform, which defines the frequencies from $-N/2T$ to $N/2T$ [42]. Equation (3.15) is more general than the approach in the previous subsection where the conjugate symmetry property was applied. Equation (3.15) covers the symmetry cases, but is not limited to these cases.

To illustrate this point, consider again the beam on elastic foundation but now introducing dashpots (Figure 3.8). As mentioned before, with the existence of damping, motion is practically damped out over a certain distance so there is no window needed to obtain the correct results with the dynamic stiffness method.

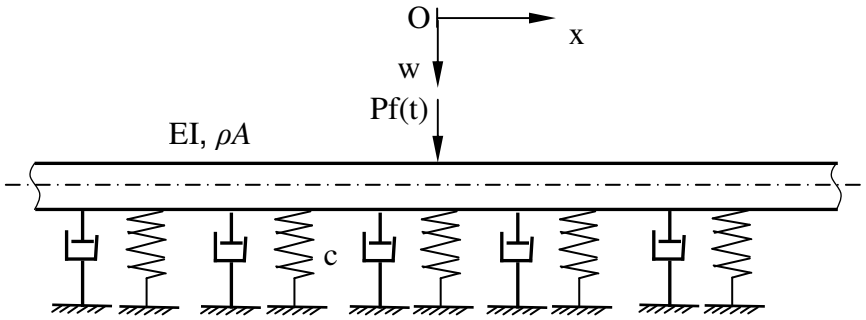

Figure 3.8 An infinitely long beam on elastic foundation with dashpots

The equation of motion is

$$EI\frac{\partial^4 w(x,t)}{\partial x^4} + cw(x,t) + \eta\frac{\partial w}{\partial t} - \rho A\frac{\partial^2 w}{\partial t^2} = Pf(t)\delta(x) \tag{3.16}$$

where

η = dashpot coefficient.

The equation in the wave number domain is

$$(EIk^4 + c - \rho A\Omega^2 + j\eta\Omega)W = P \tag{3.17}$$

If Equation (3.15) is used, the dynamic stiffness, as represented by the term in parenthesis, is no longer conjugate symmetric with respect to the Nyquist wave number, due to the existence of the imaginary term $j\eta\Omega$. So it is expected that the result obtained applying Equation (3.15) should be different from that obtained applying the conjugate symmetry property. The following figures show how the results from the conjugate symmetry property deviate from those obtained from Equation (3.15), with different amounts of damping. The length of analysis is 40.96m. The other parameters are $EI = 0.1$, $\rho A = 1.0$, $c = 500.0$, $\Omega = 2.0$.

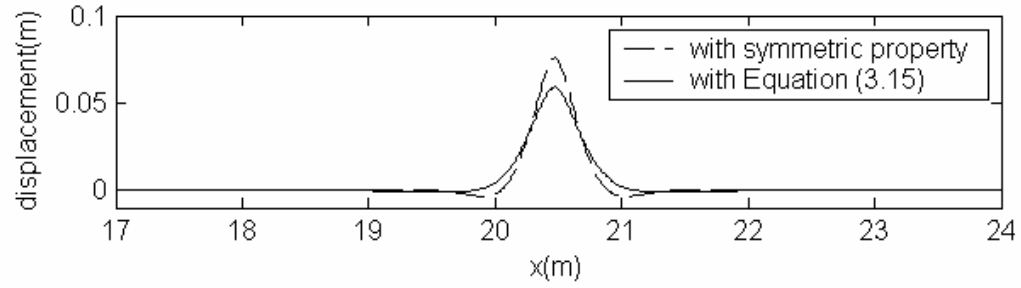

(a) η = 7.0

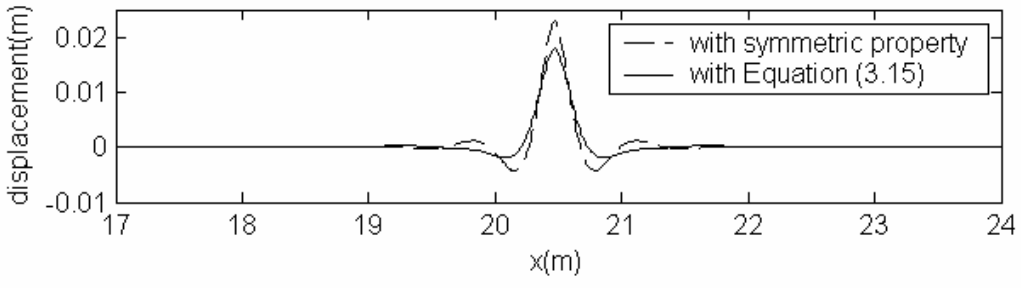

(b) η = 70

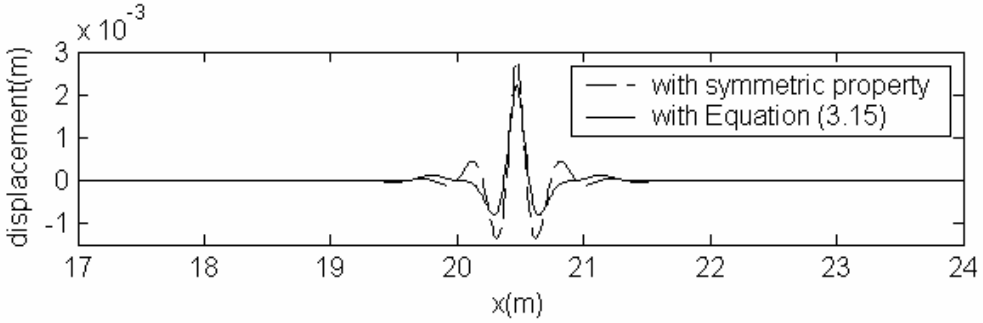

(c) η = 700

Figure 3.9 Comparison of the symmetric property and Equation (3.15)

From Figure 3.9, it can be observed that with increasing damping, the results obtained imposing symmetry with respect to the Nyquist frequency deviate increasingly from the exact solution obtained applying Equation (3.15). This is understandable because increasing the damping implies that the imaginary part of the dynamic stiffness in Equation (3.17) becomes closer to its real part so its impact can no longer be ignored.

The impact of damping is also not negligible when the exponential window is introduced to simulate effects of an absorbing boundary. The results from applying the symmetric property are compared with the analytical solution in Figure 3.10. It is clear that spurious motion is introduced. However, when Equation (3.15) is used, the results from the absorbing boundary match perfectly the analytical solution.

Figure 3.11 compares the results using the exponential window and the analytical solution with different wave number shifting parameters. The wave number shifting parameter m is associated with the parameter β in Equation (3.7) by the relation

$$\beta = m\frac{\ln(10)}{L} \tag{3.18}$$

where

ln = the natural logarithm operator

L = the analysis length or the truncated length

The parameters used in both Figure 3.9 and 3.10 are $EI = 1.0$, $\rho A = 10.0$, $c = 500.0$, $\Omega = 2.0$, $\eta = 70$.

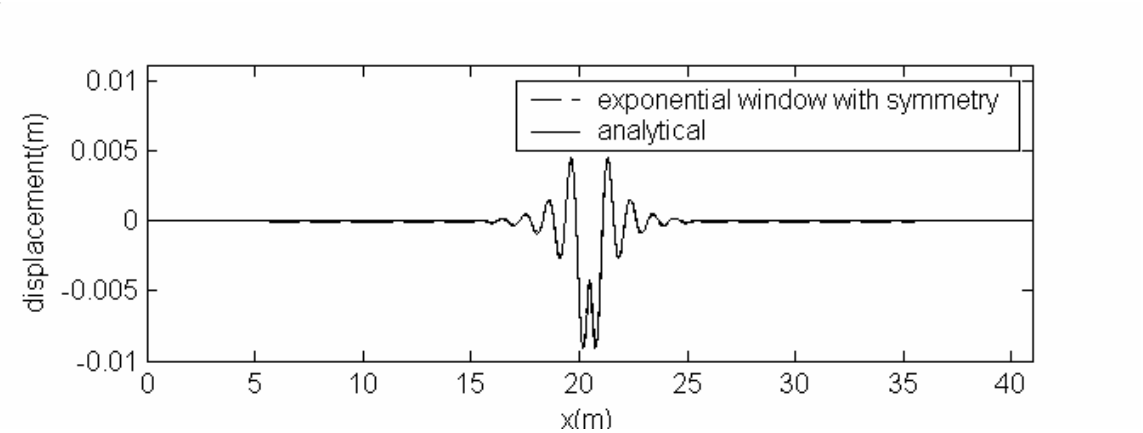

(a) m = 1.0

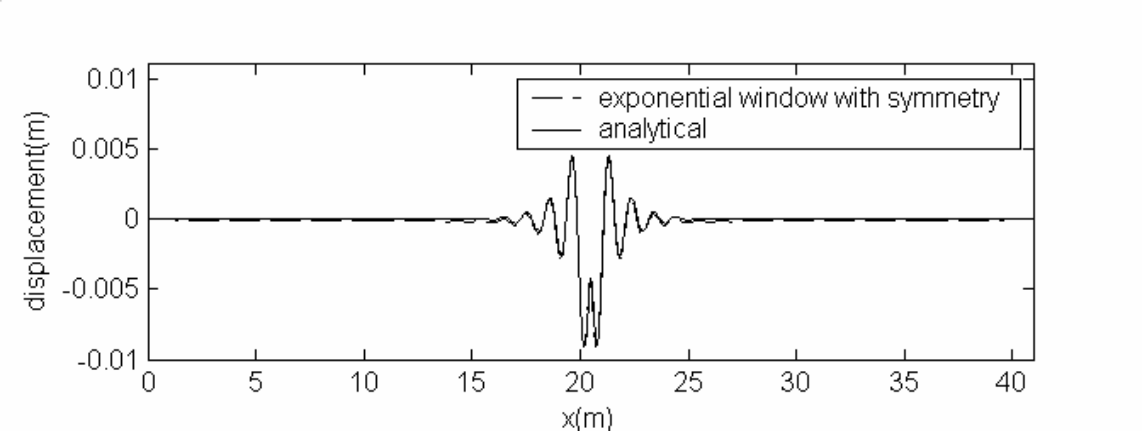

(b) m = 2.0

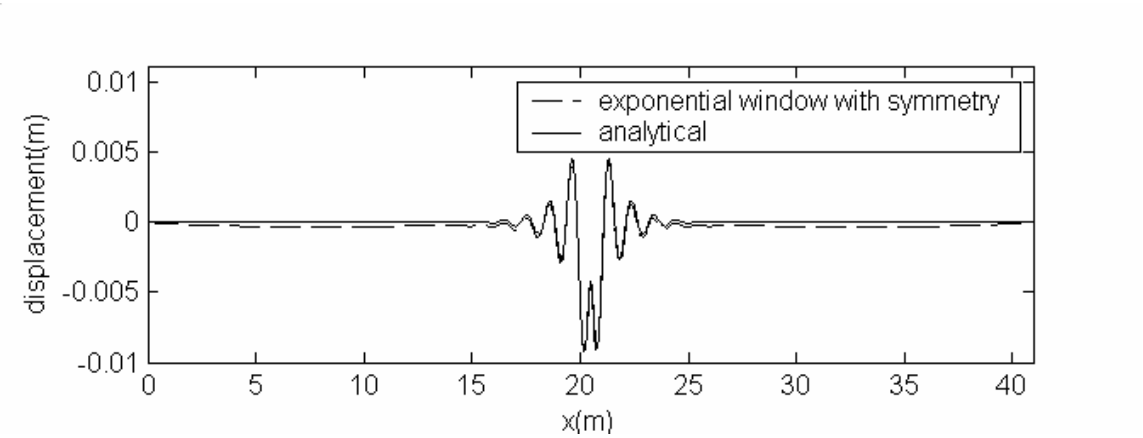

(c) m = 3.0

Figure 3.10 Results by symmetry property and the analytical solution

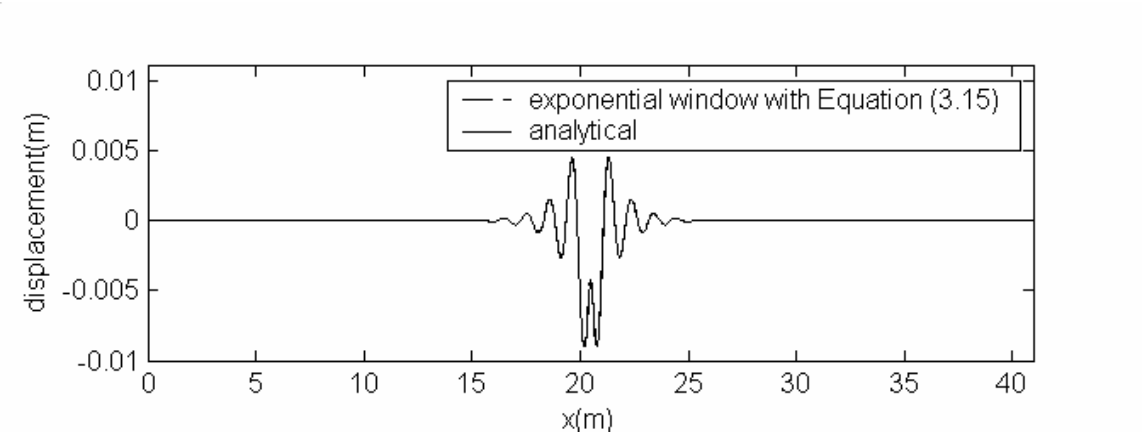

(a) m = 1.0

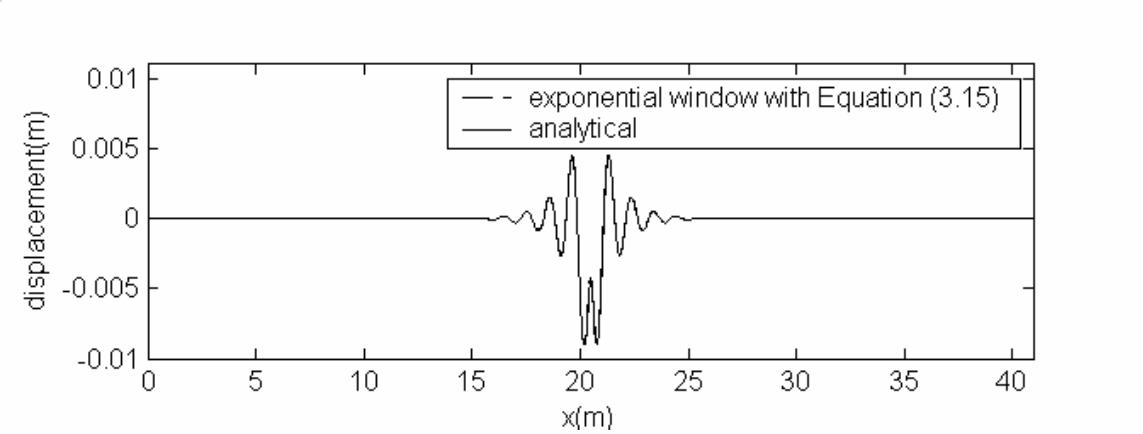

(b) m = 2.0

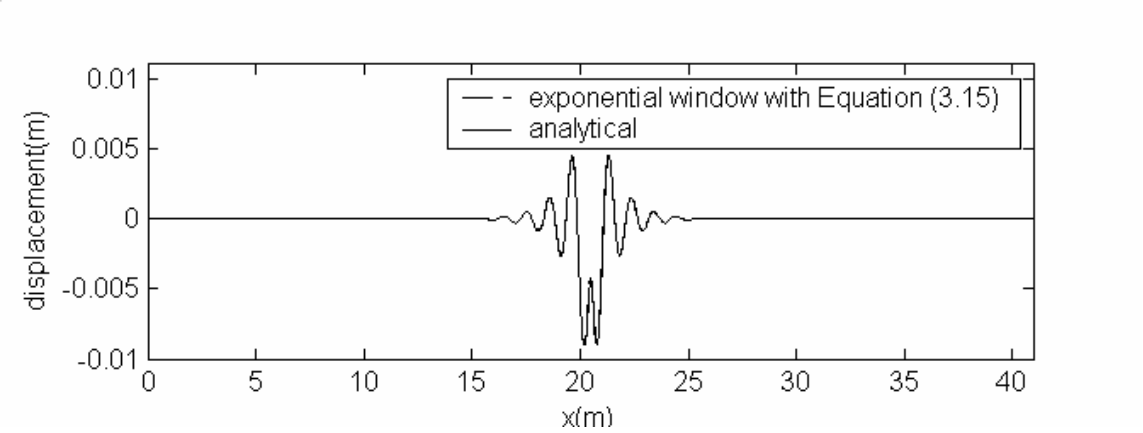

(c) m = 3.0

Figure 3.11 Results by Equation (3.15) and the analytical solution

3.6 Transient Response

The transient response of the same beam in Figure 3.3 under a triangular pulse load is studied. The time history of the load is defined as in Figure 3.12.

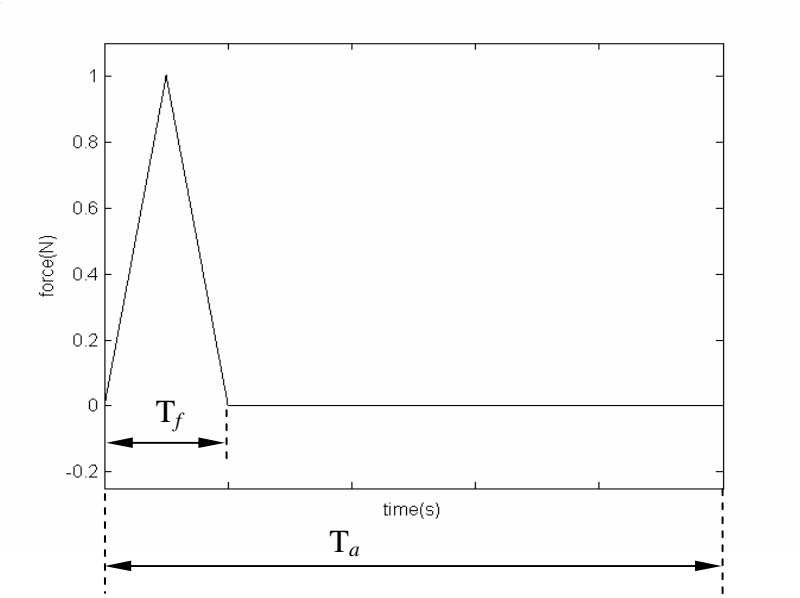

Figure 3.12 Time history of the triangular pulse

Performing the Fourier transform of Equation (3.2) with respect to *x*, one obtains

$$EIk^4 \tilde{W}(k,t) + c\tilde{W}(k,t) - \rho A \frac{\partial^2 \tilde{W}(k,t)}{\partial t^2} = Pf(t) \tag{3.19}$$

The complex wave number shift is the same as in the steady state case. Equation (3.19) can be solved in the time-wave number domain using finite differences in the time domain. The solution in the space-time domain can be then retrieved by performing the inverse Fourier transform of $\tilde{W}(k,t)$. The procedure was described in detail in Chapter II and will not be repeated here. The displacement picked up by a receiver located at distance L_R from the excitation is studied (Figure 3.13). The parameters are $EI = 1.0$, $\rho A = 10.0$, $c = 500.0$.

The displacements obtained with and without the exponential window are compared. Figure 3.14 shows the results with $L = 20.48m$ and $L_R = 3L/8$. Sixty four points are used to perform the Discrete Fourier Transform. The width of the triangular pulse is *0.5s*. With this pulse, most of the energy is carried in frequencies above the threshold frequency of 1.13Hz. Figure 3.15 shows the results with $L = 40.96m$ and $L_R = 7L/16$. 128 points were used to perform the Discrete Fourier Transform and the width of the triangular pulse was still *0.5s*.

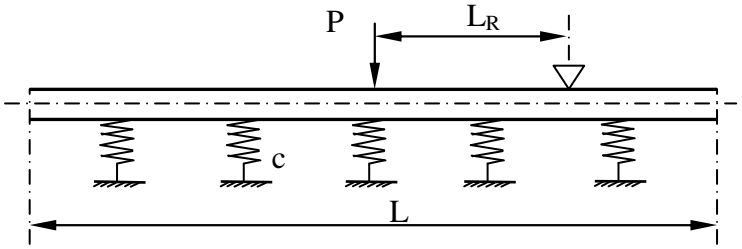

Figure 3.13 Location of the receiver

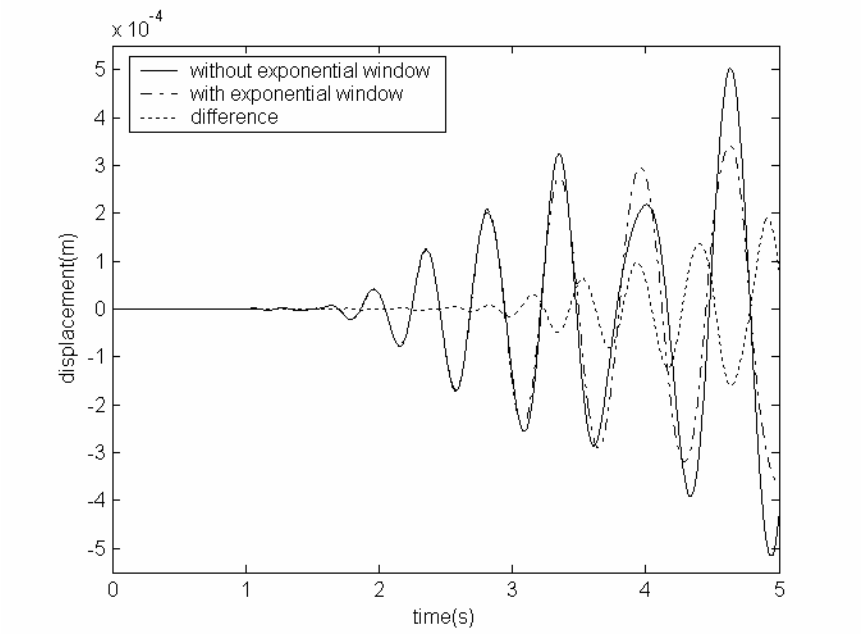

Figure 3.14 Results with and without the window ($L = 20.48m$ and $T_f = 0.5s$)

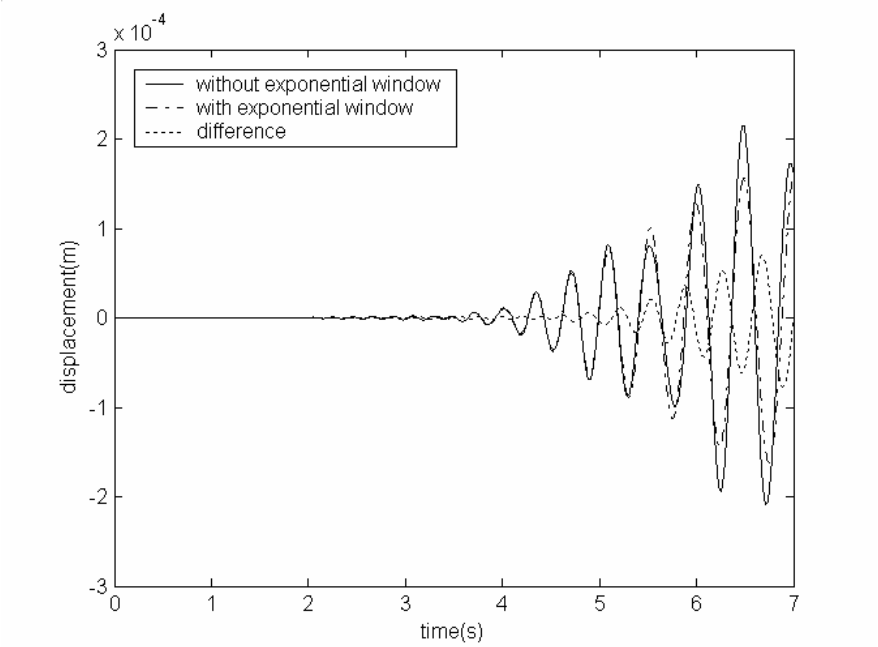

Figure 3.15 Results with and without the window ($L = 40.96m$ and $T_f = 0.5s$)

From Figures 3.14 and 3.15, it can be seen that the responses with or without the exponential window are the same at the beginning but start to differ from a certain point. It is interesting to observe that the first arrival of the responses is about 1.0 second earlier than the first arrival of the difference in both figures. The distance between the receiver and the right end of the truncated beam is the same (2.56m) in both figures, suggesting that the difference is due to the arrival of reflected waves from the right end of the truncated beam in the case without the exponential window.

The result obtained with the exponential window method is also compared with those computed with a finite element model and different lengths. Figure 3.15 shows the results from the exponential window method with $L = 20.48m$ and $L_R = 3L/8$. Also shown are the results from the finite element method with $L = 20.48m$ and $L_R = 3L/8$, and $L = 40.96m$ and $L_R = 3L/16$. From Figure 3.16, it can be seen that the finite element method gives different results with different truncated lengths (Refer to the solid line and the center line in Figure 3.16). This is understandable because the arrival time of the

reflected wave changes with the truncated length. The result with the exponential window with the smaller truncated length *20.48m* (Refer to the dotted line in Figure 3.16), however, matches well that from the finite element method with the longer truncated length *40.96m* (Refer to the center line in Figure 3.16). This indicates that with the exponential window, absorption occurs at the truncated boundary.

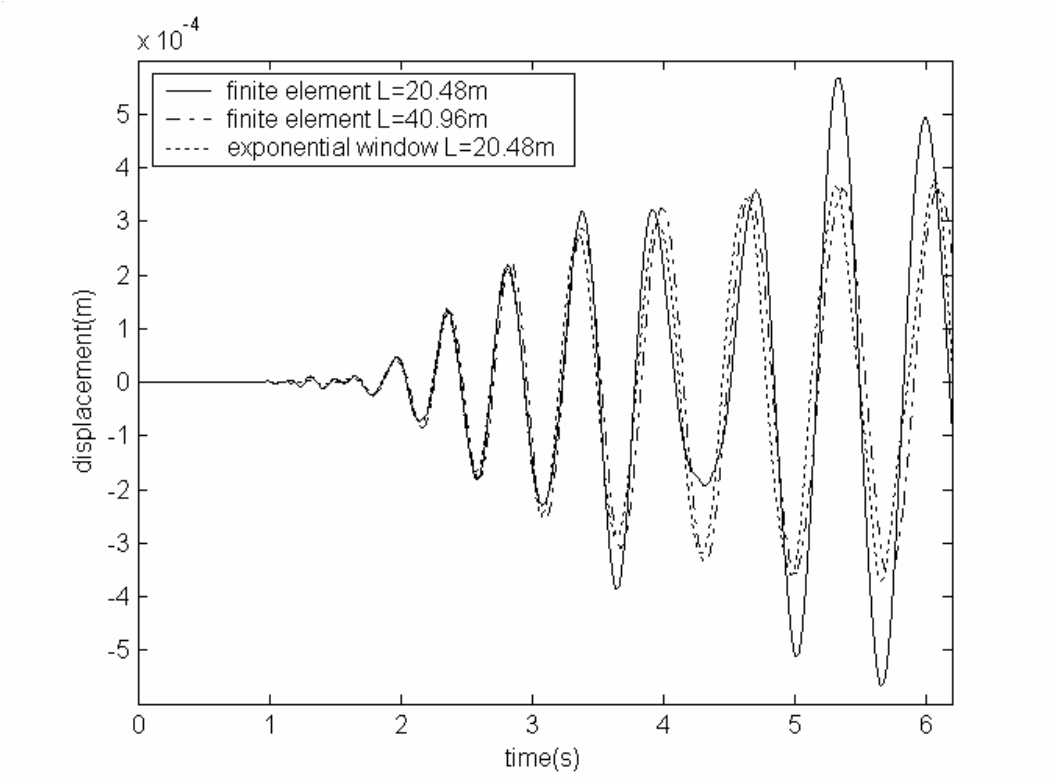

Figure 3.16 Results with exponential window and finite elements ($T_f = 0.5s$)

It is also of interest to compare the results with a different pulse length, *1.2s*. With this pulse, most of the energy is carried by frequencies below the threshold frequency. Figure 3.17 shows the results with $L = 20.48m$ and $L_R = 3L/8$. Sixty four points were used to perform the Discrete Fourier Transform. Figure 3.18 shows the results with $L = 40.96m$ and $L_R = 7L/16$. One hundred and twenty eight points were used to perform the Discrete Fourier Transform. Again, the first arrival of the responses is about 1.0

second earlier than the first arrival of the difference in both figures, suggesting the arrival of reflected waves from the right end of the truncated beam in the case without the exponential window.

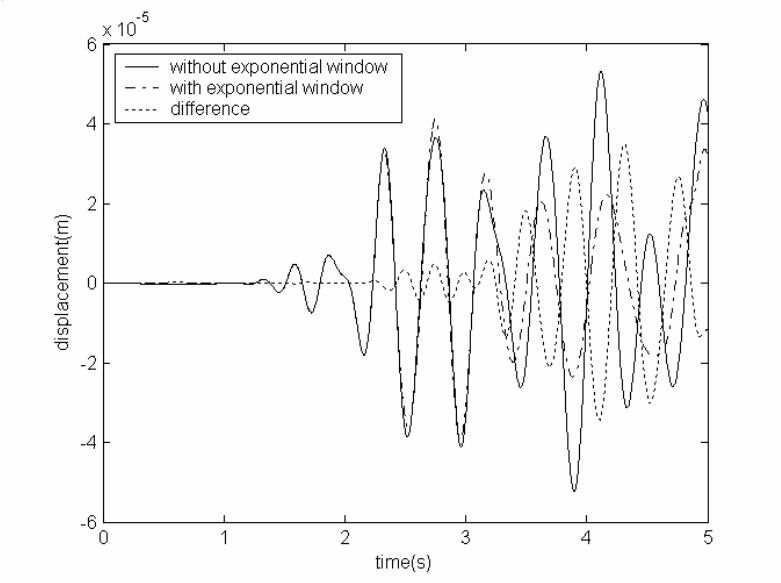

Figure 3.17 Results with and without the window ($L = 20.48m$ and $T_f = 1.2s$)

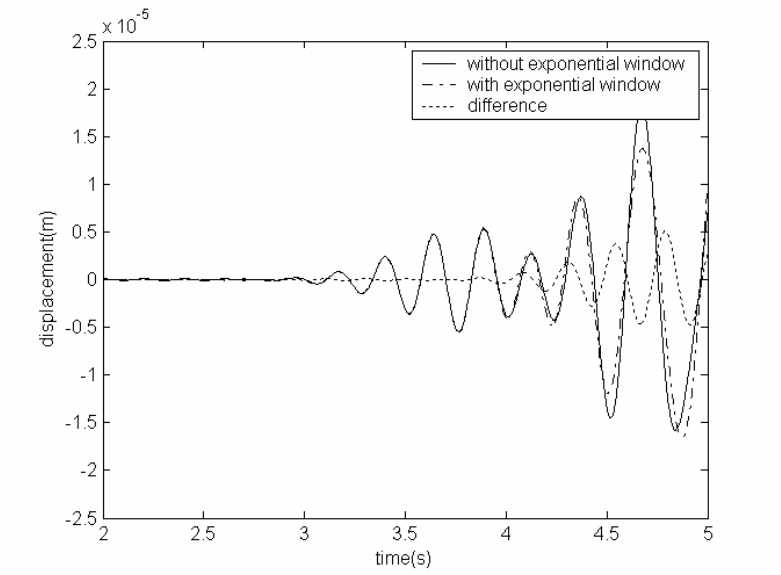

Figure 3.18 Results with and without the window ($L = 40.96m$ and $T_f = 1.2s$)

Again, the results from the exponential window method are compared with those from the finite element method. Figure 3.19 shows the results from the exponential window method with $L = 20.48m$ and $L_R = 3L/8$. Also shown are the results from the finite element method with $L = 20.48m$ and $L_R = 3L/8$, and $L = 40.96m$ and $L_R = 3L/16$. Similar to Figure 3.16, it can be seen the result with the exponential window with the smaller truncated length *20.48m* (dotted line in Figure 18) matches well that from the finite element method with the longer truncated length *40.96m* (the center line in Figure 18). This implies again that with the exponential window, absorption occurs at the truncated boundary.

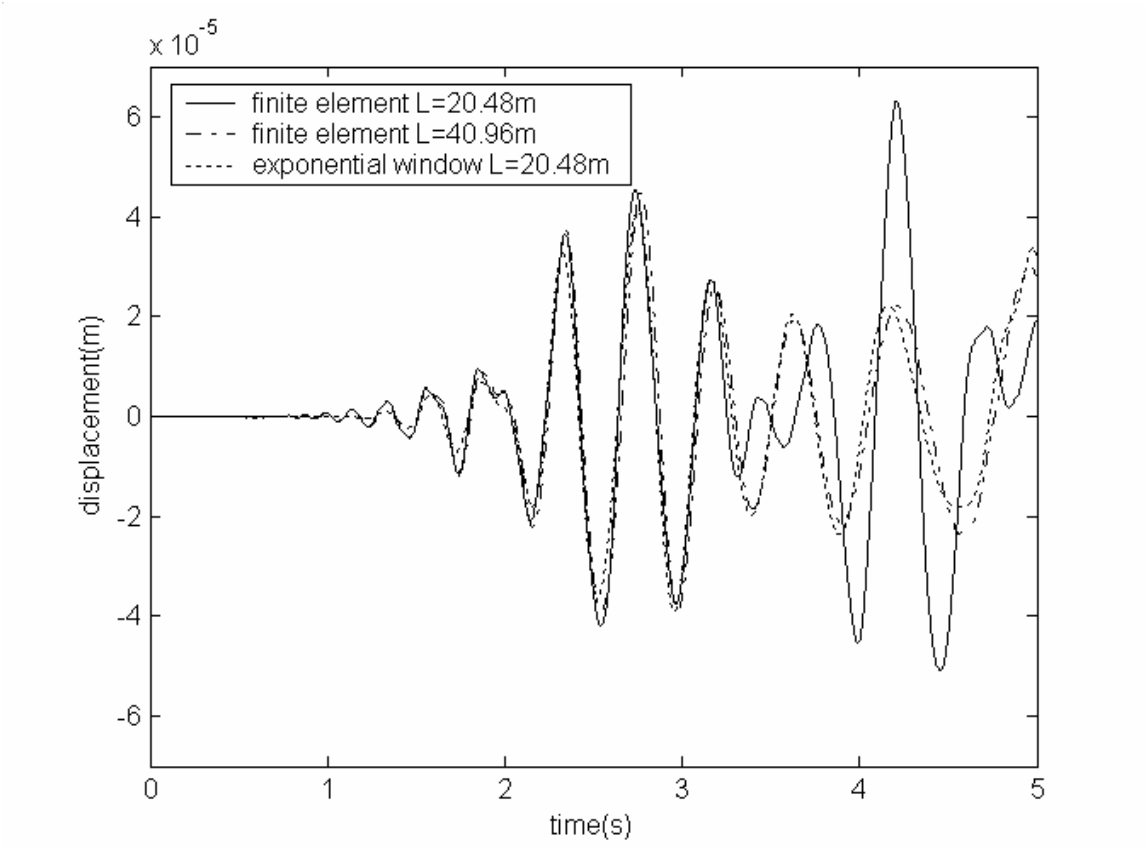

Figure 3.19 Results with exponential window and finite elements ($T_f = 1.2s$)

From the above discussion, it is seen that with exponential window, the truncated beam can be used to effectively simulate the original unbounded beam at least up to the time duration considered. However, errors appear if the duration is increased. Considering again the problem in Figure 3.19 as an example if the truncated length is large enough, the result from the finite element method can be regarded as "accurate" and used as the "true" response of the unbounded beam for a certain duration. Figure 3.20 shows the results from both finite element method and the exponential window method. The truncated length for the finite element method is *81.92m*. The truncated length for the exponential window method is *20.48m*. The distance between the excitation and the receiver is *7.68m* in both cases. It can be seen that after *5.0s*, spurious oscillations occur in the solution with the exponential window method.

It appears from these results that the exponential window introduces damping only for the wave propagating in one direction, which is the positive *x* direction in the above examples. In the negative *x* direction, when the wave motion reaches the left end, it is reflected and finally reaches the receiver. This is evidenced by the later arrival of the spurious oscillation when the truncated length is *40.96m* with the same distance between the source and the receiver. In this case, it takes longer for the spurious oscillation to get reflected at the left end, start in the positive x direction, and finally reach the receiver. In Figure 20, the result from the exponential window with the truncated length of *40.96m* matches very well with that from the finite element method. The spurious oscillation does not happen within *7.0s*.

The time at which these oscillations start coincides roughly with the time of arrival of the waves propagating in the negative direction, reflecting at the left end and reaching the point of observation. The exponential window provides thus an absorbing window at the right end for the waves propagating in the positive *x* direction but not at the left. When the length is increased to *40.96m*, with the result also shown in Figure 3.20, the waves reflected at the left end do not have enough time to reach the observation point within the *7.0* seconds considered.

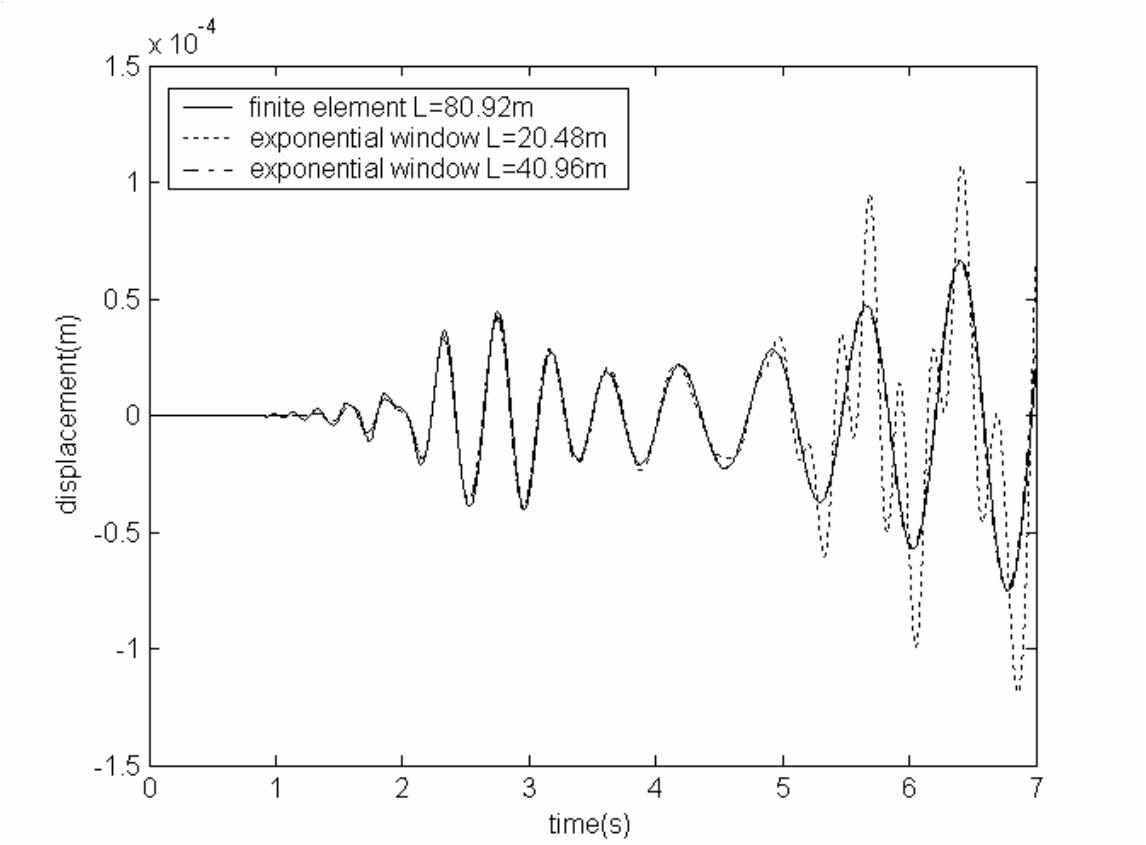

Figure 3.20 Responses at the receiver with different truncated lengths

CHAPTER IV

PLANE *SV*-*P* WAVES IN AN UNBOUNDED STRIP

4.1 Overview

In this chapter we consider the propagation of plane *SV* and *P* waves in an unbounded strip that can represent a soil layer over rigid rock (Figure 4.1). The strip is infinite in the *x* direction but finite in the *y* direction. The boundary conditions on the upper and lower boundary in the *y* direction are physical. For the case of a soil layer overlying much stiffer rock, the top boundary would have specified stresses or tractions while the bottom boundary is fixed. In Figure 4.1, both the top and bottom boundary are fixed. In this case, uniformly distributed loads are located in the shaded area. The direction of the load can be horizontal, as shown in Figure 4.1, or vertical.

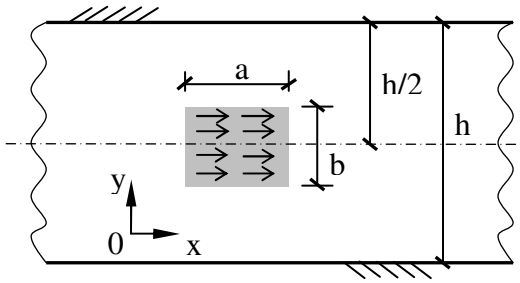

Figure 4.1 The infinite strip

As mentioned in Chapter II, the displacement field is approximated by a finite element expansion in the directions where the domain is finite and a modified equation of motion is derived. In this problem, the finite element expansion is applied in the *y* direction. The strip is infinitely long in the *x* direction so it is truncated at some distance. The same method could be used for three-dimensional problems with a finite dimension in two directions and an infinite length in the third direction. Then a two-dimensional

finite element expansion would be employed on the cross section and the Fourier expansion would be used with the exponential window in the infinite direction.

4.2 Modified Equation of Motion

The equation of motion for plane *SV-P* waves is

$$(\lambda+\mu)\left(\frac{\partial^2 u}{\partial x^2}+\frac{\partial^2 v}{\partial x \partial y}\right)+\mu\nabla^2 u=\rho\frac{\partial^2 u}{\partial t^2} \tag{4.1a}$$

$$(\lambda+\mu)\left(\frac{\partial^2 u}{\partial y \partial x}+\frac{\partial^2 v}{\partial y^2}\right)+\mu\nabla^2 v=\rho\frac{\partial^2 v}{\partial t^2} \tag{4.1b}$$

where

ρ = mass density

λ, μ = Lame's constants

u = displacement in x direction

v = displacement in y direction

$$\nabla^2=\frac{\partial^2}{\partial x^2}+\frac{\partial^2}{\partial y^2}$$

Consider a sub-layer taken from the unbounded strip in Figure 4.1 as shown in Figure 4.2. The displacement vector is $\mathbf{U}=\{u,v\}^T$. The nodal displacement vector $\mathbf{V}=\{u_1,v_1,u_2,v_2\}^T$ has u_1 and v_1 as displacements at the top and u_2 and v_2 at the bottom, respectively. The force vector is $\mathbf{T}=\{p_1,q_1,p_2,q_2\}^T$ with p_1, q_1 as tractions at the top and p_2, q_2 at the bottom, respectively.

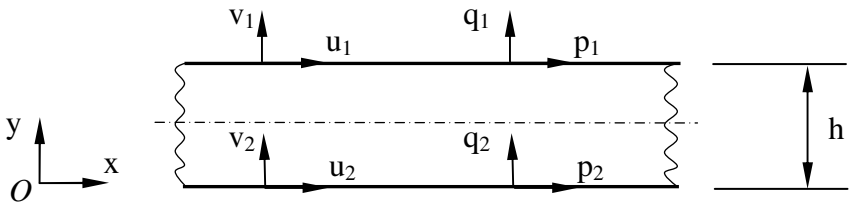

Figure 4.2 A sub-layer of finite element

Calling $\boldsymbol{\sigma} = \{\sigma_{xx}, \sigma_{yy}, \sigma_{xy}\}^T$ and $\boldsymbol{\varepsilon} = \{\varepsilon_{xx}, \varepsilon_{yy}, \varepsilon_{xy}\}^T$, the constitutive law is

$$\boldsymbol{\sigma} = \mathbf{C}\boldsymbol{\varepsilon} \text{ with } \mathbf{C} = \begin{bmatrix} \lambda + 2\mu & \lambda & 0 \\ \lambda & \lambda + 2\mu & 0 \\ 0 & 0 & \mu \end{bmatrix}.$$

The strains and displacements are connected by

$$\boldsymbol{\varepsilon} = \mathbf{L}^{\mathbf{T}}\mathbf{U} \text{ with } \mathbf{L} = \begin{bmatrix} \frac{\partial}{\partial x} & 0 & \frac{\partial}{\partial y} \\ 0 & \frac{\partial}{\partial y} & \frac{\partial}{\partial x} \end{bmatrix}.$$

Following Kausel's formulation [23], the displacement field can be written as

$$\mathbf{U}(x, y, t) = \mathbf{N}(y)\mathbf{V}(x, t) \tag{4.2}$$

The matrix **N** is

$$\mathbf{N}(y) = \begin{bmatrix} \frac{h-y}{h} & 0 & \frac{y}{h} & 0 \\ 0 & \frac{h-y}{h} & 0 & \frac{y}{h} \end{bmatrix} \text{ for linear elements and}$$

$$\mathbf{N}(y) =$$

$$\begin{bmatrix} 1-3\frac{x}{h}+2\frac{x^2}{h^2} & 0 & 4(\frac{x}{h}-\frac{x^2}{h^2}) & 0 & -\frac{x}{h}+2\frac{x^2}{h^2} & 0 \\ 0 & 1-3\frac{x}{h}+2\frac{x^2}{h^2} & 0 & 4(\frac{x}{h}-\frac{x^2}{h^2}) & 0 & -\frac{x}{h}+2\frac{x^2}{h^2} \end{bmatrix}$$

for quadratic elements.

Applying then the principle of virtual work to the finite element layer,

$$\delta\mathbf{V}^{*T}\mathbf{T} = \int_0^h \delta\boldsymbol{\varepsilon}^{*T}\boldsymbol{\sigma}dx \tag{4.3}$$

The superscript in Equation (4.3) stands for conjugate operation. The reason for introducing this more general form of virtual work is that the displacement $\mathbf{V}(x,t)$ can be treated as a complex number later on by assuming $\mathbf{V}(x,t) = \bar{\mathbf{V}}(k,t)e^{jkx}$, which is equivalent to applying a Fourier transform to $\mathbf{V}(x,t)$ with respect to *x*. With the

conjugate operation, anti-symmetric first-order terms are produced. Then the mass and stiffness matrix can be derived as

$$\mathbf{M} = \int_0^h \rho \mathbf{N}^T \mathbf{N} dy \tag{4.4}$$

$$\mathbf{K} = \int_0^h \mathbf{N}^T \mathbf{L}^{*T} \mathbf{C} \mathbf{L} \mathbf{N} dy \tag{4.5}$$

The stiffness matrix can be decomposed into three matrices associated with the second-order, first-order and constant term, respectively. After some algebraic manipulations, one obtains the modified equation of motion.

$$-\mathbf{A}_2 \frac{\partial^2 \mathbf{V}}{\partial x^2} + \mathbf{A}_1 \frac{\partial \mathbf{V}}{\partial x} + \mathbf{A}_0 \mathbf{V} + \mathbf{M} \frac{\partial^2 \mathbf{V}}{\partial t^2} = \mathbf{T} \tag{4.6}$$

There is a first-order term in the equation. As stated in Chapter II, the first-order term does not indicate the existence of damping as it would with first order time derivatives. For linear elements, the matrices are listed below for ready reference. Note that $\boldsymbol{A}_1$ is anti-symmetric.

$$\mathbf{A}_2 = \begin{bmatrix} \frac{h(\lambda+2\mu)}{3} & 0 & \frac{h(\lambda+2\mu)}{6} & 0 \\ 0 & \frac{h\mu}{3} & 0 & \frac{h\mu}{6} \\ \frac{h(\lambda+2\mu)}{6} & 0 & \frac{h(\lambda+2\mu)}{3} & 0 \\ 0 & \frac{h\mu}{6} & 0 & \frac{h\mu}{3} \end{bmatrix}$$

$$\mathbf{A}_1 = \begin{bmatrix} 0 & \frac{\mu-\lambda}{2} & 0 & \frac{\mu+\lambda}{2} \\ \frac{\lambda-\mu}{2} & 0 & \frac{\mu+\lambda}{2} & 0 \\ 0 & -\frac{\mu+\lambda}{2} & 0 & \frac{\lambda-\mu}{2} \\ -\frac{\mu+\lambda}{2} & 0 & \frac{\mu-\lambda}{2} & 0 \end{bmatrix}$$

$$\mathbf{A}_0 = \begin{bmatrix} \frac{G}{h} & 0 & -\frac{G}{h} & 0 \\ 0 & \frac{\lambda+2G}{h} & 0 & -\frac{\lambda+2G}{h} \\ -\frac{G}{h} & 0 & \frac{G}{h} & 0 \\ 0 & -\frac{\lambda+2G}{h} & 0 & \frac{\lambda+2G}{h} \end{bmatrix}$$

$$\mathbf{M} = \begin{bmatrix} \frac{\rho h}{3} & 0 & \frac{\rho h}{6} & 0 \\ 0 & \frac{\rho h}{3} & 0 & \frac{\rho h}{6} \\ \frac{\rho h}{6} & 0 & \frac{\rho h}{3} & 0 \\ 0 & \frac{\rho h}{6} & 0 & \frac{\rho h}{3} \end{bmatrix}$$

For quadratic elements, the matrices are

$$\mathbf{A}_2 = \begin{bmatrix} \frac{2\mu h}{15} & 0 & \frac{\mu h}{15} & 0 & -\frac{\mu h}{30} & 0 \\ 0 & \frac{(4\lambda+2\mu)h}{15} & 0 & \frac{(2\lambda+\mu)h}{15} & 0 & -\frac{(2\lambda+\mu)h}{30} \\ \frac{\mu h}{15} & 0 & \frac{8\mu h}{15} & 0 & \frac{\mu h}{15} & 0 \\ 0 & \frac{(2\lambda+\mu)h}{15} & 0 & \frac{(16\lambda+8\mu)h}{15} & 0 & \frac{(2\lambda+\mu)h}{15} \\ -\frac{\mu h}{30} & 0 & \frac{\mu h}{15} & 0 & \frac{2\mu h}{15} & 0 \\ 0 & -\frac{(2\lambda+\mu)h}{30} & 0 & \frac{(2\lambda+\mu)h}{15} & 0 & \frac{(4\lambda+2\mu)h}{15} \end{bmatrix}$$

$$\mathbf{A}_1 = \begin{bmatrix} 0 & \frac{\mu-\lambda}{2} & 0 & -\frac{4(\lambda+\mu)}{3} & 0 & \frac{\lambda+\mu}{3} \\ \frac{\lambda-\mu}{2} & 0 & -\frac{4(\lambda+\mu)}{3} & 0 & \frac{\lambda+\mu}{3} & 0 \\ 0 & \frac{4(\lambda+\mu)}{3} & 0 & 0 & 0 & -\frac{4(\lambda+\mu)}{3} \\ \frac{4(\lambda+\mu)}{3} & 0 & 0 & 0 & -\frac{4(\lambda+\mu)}{3} & 0 \\ 0 & -\frac{\lambda+\mu}{3} & 0 & \frac{4(\lambda+\mu)}{3} & 0 & \frac{\mu-\lambda}{2} \\ -\frac{\lambda+\mu}{3} & 0 & \frac{4(\lambda+\mu)}{3} & 0 & \frac{\lambda-\mu}{2} & 0 \end{bmatrix}$$

$$\mathbf{A}_0 = \begin{bmatrix} \frac{7(\lambda+2\mu)}{3h} & 0 & -\frac{8(\lambda+2\mu)}{3h} & 0 & \frac{\lambda+2\mu}{h} & 0 \\ 0 & \frac{7\mu}{3h} & 0 & -\frac{8\mu}{3h} & 0 & \frac{\mu}{h} \\ -\frac{8(\lambda+2\mu)}{3h} & 0 & \frac{16(\lambda+2\mu)}{3h} & 0 & -\frac{8(\lambda+2\mu)}{3h} & 0 \\ 0 & -\frac{8\mu}{3h} & 0 & \frac{16\mu}{3h} & 0 & -\frac{8\mu}{3h} \\ \frac{\lambda+2\mu}{h} & 0 & -\frac{8(\lambda+2\mu)}{3h} & 0 & \frac{7(\lambda+2\mu)}{3h} & 0 \\ 0 & \frac{\mu}{h} & 0 & -\frac{8\mu}{3h} & 0 & \frac{7\mu}{3h} \end{bmatrix}$$

$$\mathbf{M} = \begin{bmatrix} \frac{2\rho h}{15} & 0 & \frac{2\rho h}{15} & 0 & -\frac{\rho h}{15} & 0 \\ 0 & \frac{2\rho h}{15} & 0 & \frac{2\rho h}{15} & 0 & -\frac{\rho h}{15} \\ \frac{2\rho h}{15} & 0 & \frac{8\rho h}{15} & 0 & \frac{2\rho h}{15} & 0 \\ 0 & \frac{2\rho h}{15} & 0 & \frac{8\rho h}{15} & 0 & \frac{2\rho h}{15} \\ -\frac{\rho h}{15} & 0 & \frac{2\rho h}{15} & 0 & \frac{2\rho h}{15} & 0 \\ 0 & -\frac{\rho h}{15} & 0 & \frac{2\rho h}{15} & 0 & \frac{2\rho h}{15} \end{bmatrix}$$

As mentioned in the previous section, this approach may also be applied to three-dimensional cases where the dimension in the longitudinal direction is infinite (Figure 4.3). On the cross section, the displacement is approximated by a finite element expansion and in the longitudinal direction (z direction) the Fourier transform is used.

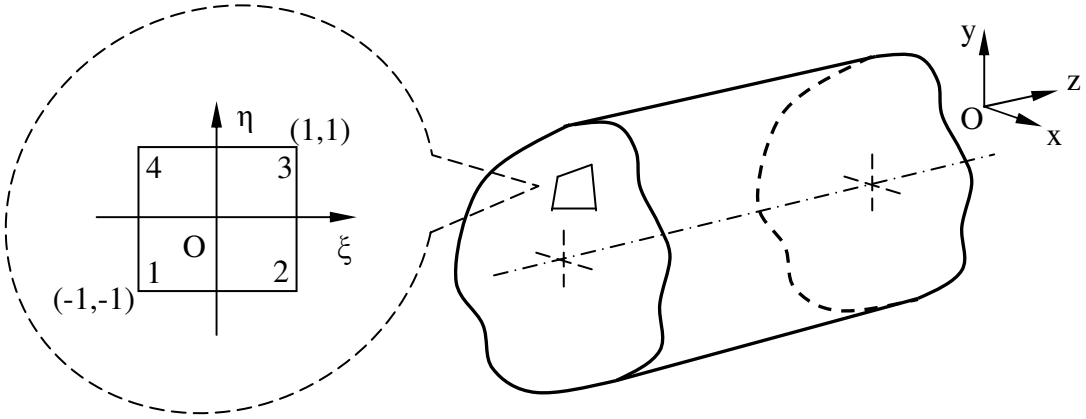

Figure 4.3 A three-dimensional problem

The element matrices take the same form as the two dimensional case. In the reference coordinate, the general form of the matrices for the master element is

$$\mathbf{M} = \iint_D \rho \mathbf{N}(\xi,\eta)^T \mathbf{N}(\xi,\eta) \mid J \mid d\xi d\eta \tag{4.7}$$

$$\mathbf{K} = \iint_D \mathbf{N}(\xi,\eta)^T \mathbf{L}^{*T} \mathbf{C} \mathbf{L} \mathbf{N}(\xi,\eta) d\xi d\eta \tag{4.8}$$

In expressions (4.7) and (4.8), ξ and η are local coordinates, $|J|$ is the Jacobian representing the transform from the global coordinates to the reference coordinates, **N** is the shape function matrix, and **C** represents the constitutive law.

$$\mathbf{L} = \begin{bmatrix} \frac{\partial}{\partial x} & 0 & 0 & 0 & \frac{\partial}{\partial z} & \frac{\partial}{\partial y} \\ 0 & \frac{\partial}{\partial y} & 0 & \frac{\partial}{\partial z} & 0 & \frac{\partial}{\partial x} \\ 0 & 0 & \frac{\partial}{\partial z} & \frac{\partial}{\partial y} & \frac{\partial}{\partial x} & 0 \end{bmatrix}$$

$$\mathbf{C}=\begin{bmatrix} \lambda+2\mu & \lambda & \lambda & 0 & 0 & 0 \\ \lambda & \lambda+2\mu & \lambda & 0 & 0 & 0 \\ \lambda & \lambda & \lambda+2\mu & 0 & 0 & 0 \\ 0 & 0 & 0 & \mu & 0 & 0 \\ 0 & 0 & 0 & 0 & \mu & 0 \\ 0 & 0 & 0 & 0 & 0 & \mu \end{bmatrix}$$

The matrix **N** depends on the element type used. For linear quadrilateral elements, $\mathbf{N}(y)=\begin{bmatrix} N_1\mathbf{I} & N_2\mathbf{I} & N_3\mathbf{I} & N_4\mathbf{I} \end{bmatrix}$,

where

I = 3×3 identity matrix

$$N_1=\frac{1}{4}(\xi-1)(\eta-1)$$

$$N_2=-\frac{1}{4}(\xi+1)(\eta-1)$$

$$N_3=\frac{1}{4}(\xi+1)(\eta+1)$$

$$N_4=-\frac{1}{4}(\xi-1)(\eta+1)$$

Therefore for linear quadrilateral elements, **M** and **K** are 12×12. For linear triangular elements, **M** and **K** are 9×9.

4.3 The Complex Wave Number Shift

Performing the Fourier transform with respect to the space coordinate *x*, one obtains the equation in the wave number-time domain

$$(\mathbf{A}_2k^2+j\mathbf{A}_1k+\mathbf{A}_0)\bar{\mathbf{V}}(k,t)+\mathbf{M}\frac{\partial^2\bar{\mathbf{V}}(k,t)}{\partial t^2}=\bar{\mathbf{T}}(k,t) \tag{4.9}$$

where

k = wave number in x direction

j = unit imaginary number

$\bar{\mathbf{V}}$ = Fourier transform of the displacement

$\bar{\mathbf{T}}$ = Fourier transform of the load

The complex wave number is defined by

$$k' = k + j\eta \tag{4.10}$$

Substituting Equation (4.10) into Equation (4.9), one has

$$[\mathbf{A}_2(k' - j\eta)^2 + j\mathbf{A}_1(k' - j\eta) + \mathbf{A}_0]\bar{\mathbf{V}}(k' - j\eta, t) + \mathbf{M}\frac{\partial^2 \bar{\mathbf{V}}(k' - j\eta, t)}{\partial t^2} = \bar{\mathbf{T}}(k' - j\eta, t) \tag{4.11}$$

To find the load in the shifted wave number domain, one needs to impose the decaying window in the space domain before performing the Fourier transform

$$\bar{\mathbf{T}}(k' - j\eta, t) = \int_{-\infty}^{\infty} \mathbf{T}(x,t)e^{-\eta x}e^{-jkx}dx \tag{4.12}$$

To find the displacement in the original system, one needs to impose the rising window after obtaining the displacement in the space domain.

$$\mathbf{V}(x,t) = e^{\eta x}\int_{-\infty}^{\infty} \bar{\mathbf{V}}(x,t)e^{jkx}dk \tag{4.13}$$

Defining the stiffness matrix in the wave number domain

$$\mathbf{K} = \mathbf{A}_2(k' - j\eta)^2 + j\mathbf{A}_1(k' - j\eta) + \mathbf{A}_0 \tag{4.14}$$

Equation (4.7) can be briefly written as

$$\mathbf{K}\bar{\mathbf{V}} + \mathbf{M}\frac{\partial^2 \bar{\mathbf{V}}}{\partial t^2} = \bar{\mathbf{T}} \tag{4.15}$$

To solve Equation (4.15) with respect to time, an explicit finite difference scheme is implemented. The scheme is discussed in detail in Chapter II and will not be repeated here.

4.4 Numerical Examples

4.4.1 Horizontal area load

To validate the method, numerical experiments were carried out to assess the usefulness of the exponential window approach. In this sub-section, a uniform area load in the horizontal direction is applied to the infinite strip. As shown in Figure 4.4, the infinite strip is truncated so that the loading area is located at the center of the domain. As a comparison, the P-SV wave propagating in a domain of the same size as the truncated one is solved by the finite element method (Figure 4.4). *L* is the length of the domain.

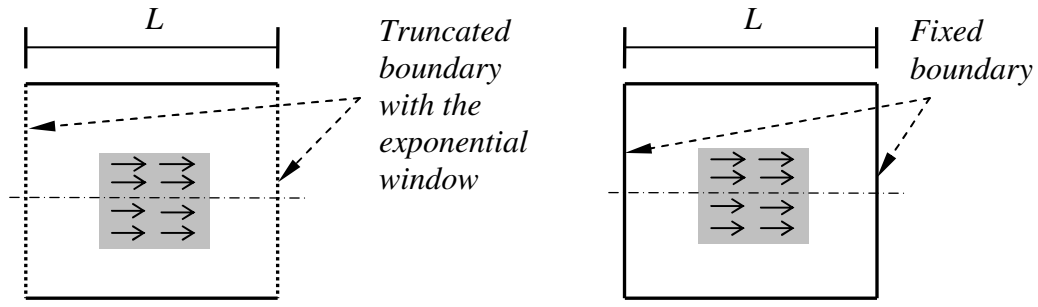

(a) exponential window (b) finite elements

Figure 4.4 Absorbing boundary and finite element method settings

The parameters are listed in Table 4.1. In the Fourier expansion approach, 65 points are used in the *x* direction and 64 linear finite elements are used in the *y* direction. In the finite element approach, 32 second-order spectral finite elements are used in both *x* and *y* directions. In both cases, the number of nodes in the *x* and *y* directions are the same, which is 65. The load is a rectangular pulse running from *0.003*s to *0.006s* in time.

Table 4.1 Parameters used in the horizontal load case

Length of the domain	L	*10.0m*
Width of the domain	h	*20.0m*
Length of the loading area	a	*1.25m*
Width of the loading area	b	*2.5m*
Mass density	ρ	*22.0 kg/m^3*
P-wave velocity	c_p	*20 m/s*
S-wave velocity	c_s	*11.57 m/s*
Magnitude of the horizontal load	q	*1.0e+3 N/m^2*

First, the horizontal and vertical displacements of the entire domain at *0.18s*, *0.33s* and *0.39s* for both methods are shown in Figure 4.5. It can be seen that at 0.18s, the wave has not reached the boundary so the two models give identical distribution pattern of the displacement fields. At *0.33s*, the wave has already arrived at the boundary so reflected waves can be observed for the finite element solution while they are absent for the Fourier expansion case. The displacements at 0.39s confirm that the exponential window approach absorbs all incident waves. Notice that the vertical displacement is anti-symmetric with respect to the center of the loading area, as expected.

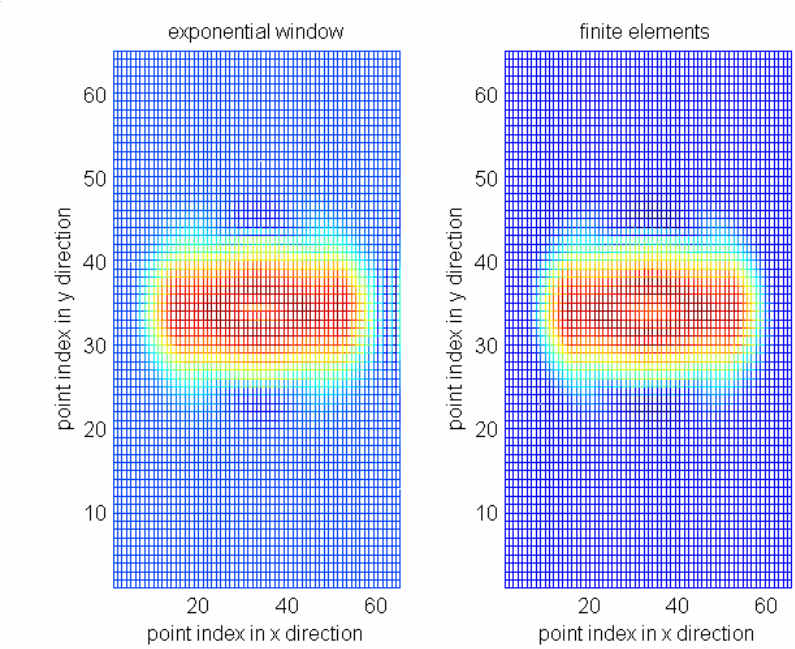

(a) Horizontal displacement at 0.18s

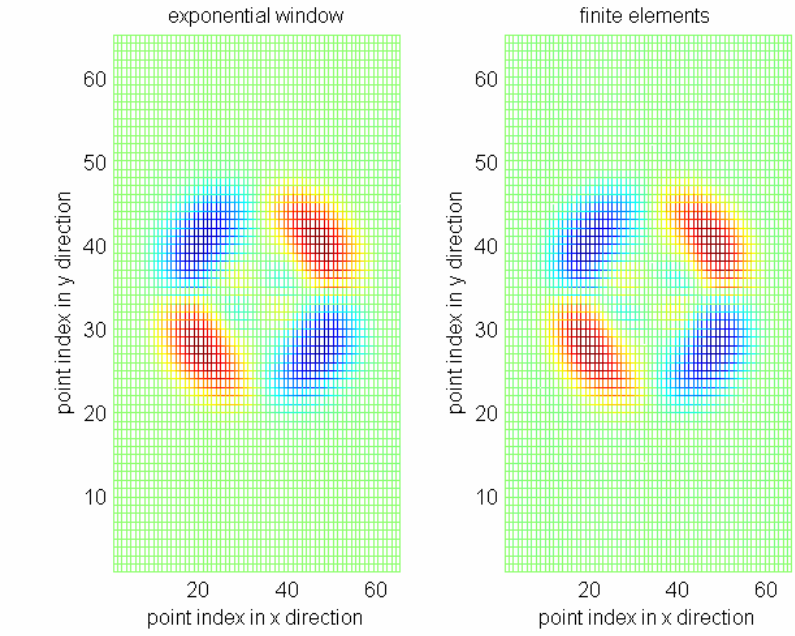

(b) Vertical displacement at 0.18s

Figure 4.5 Displacement fields at different times for the horizontal load

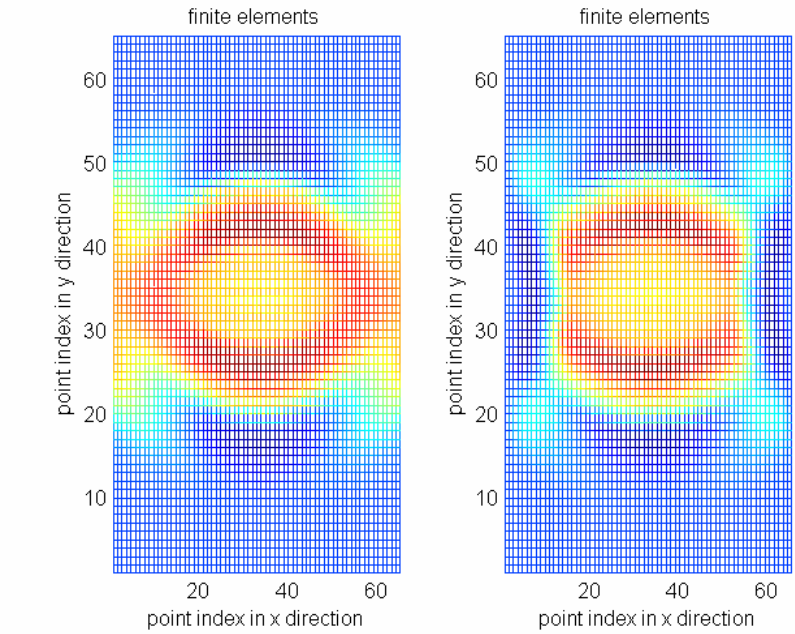

(c) Horizontal displacement at 0.33s

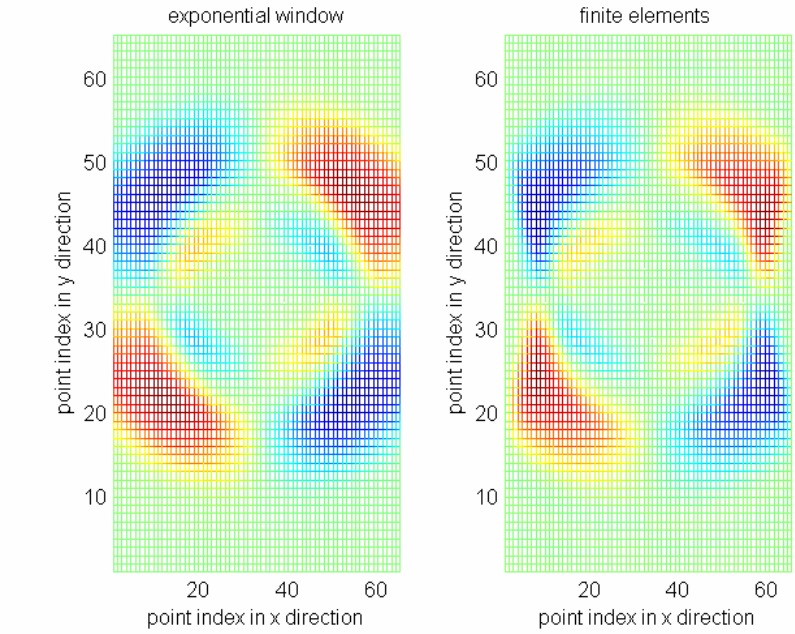

(d) Vertical displacement at 0.33s

Figure 4.5 Continued

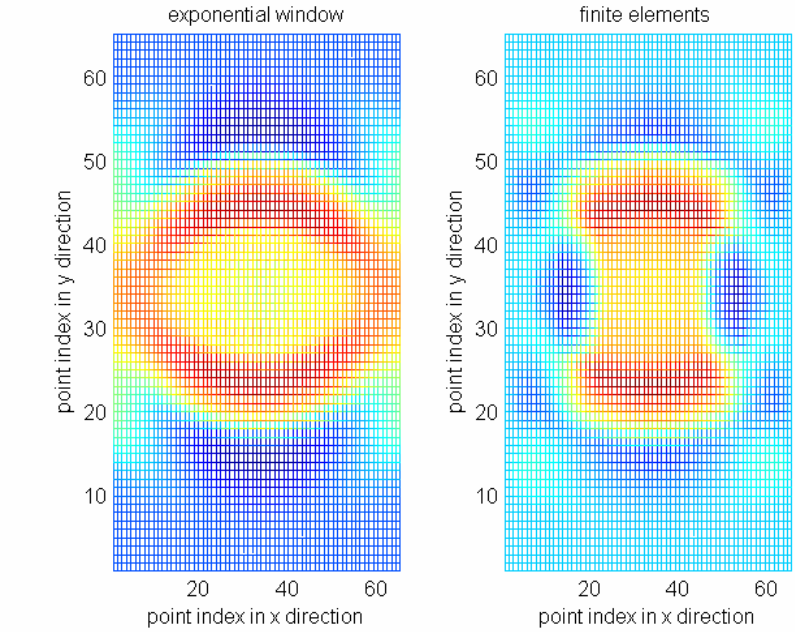

(e) Horizontal displacement at 0.39s

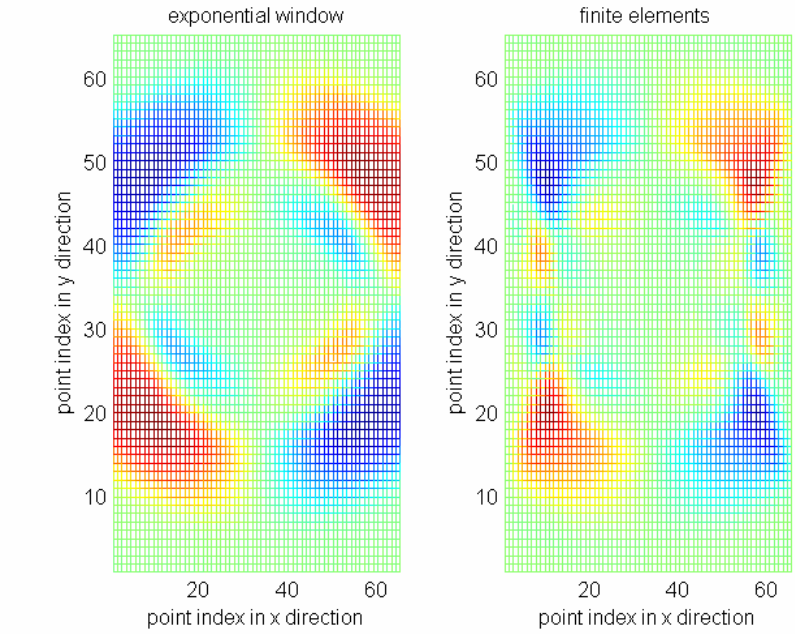

(f) Vertical displacement at 0.39s

Figure 4.5 Continued

It is also interesting to compare the time history of the displacement at specific locations. Next, horizontal and vertical displacements at four different locations in the domain are compared for these two different methods. Figure 4.6 shows the position of the points. The coordinates of the points are listed in Table 4.2. The origin is located at the left lower corner of the truncated domain. The horizontal displacements of the four points and vertical displacements of Points *C* and *D* are compared. The vertical displacement at Points *A* and *B* are zero, due to the symmetric settings of the problem. The results are shown in Figure 4.7. Again, it demonstrates the effectiveness of the exponential window approach. In Figure 4.7, "EM" stands for "exponential window". The results from the two different methods match well until the reflected wave arrives in the finite element method case.

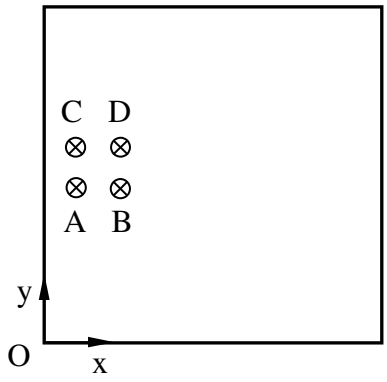

Figure 4.6 Location of the four points

Table 4.2 The coordinates of the four points

	X coordinates (m)	Y coordinates (m)
Point A	*0.156*	*10.0*
Point B	*0.468*	*10.0*
Point C	*0.156*	*11.248*
Point D	*0.468*	*11.248*

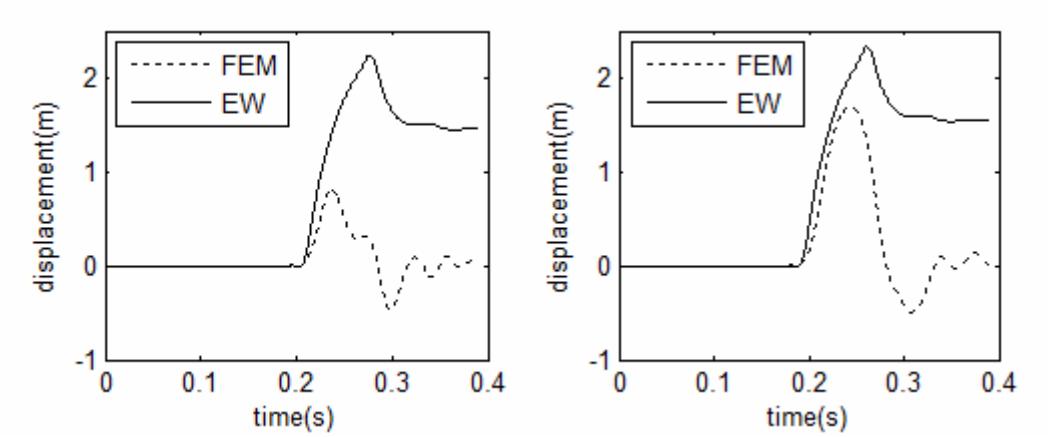

(a) Horizontal displacement at Point A (b) Horizontal displacement at Point B

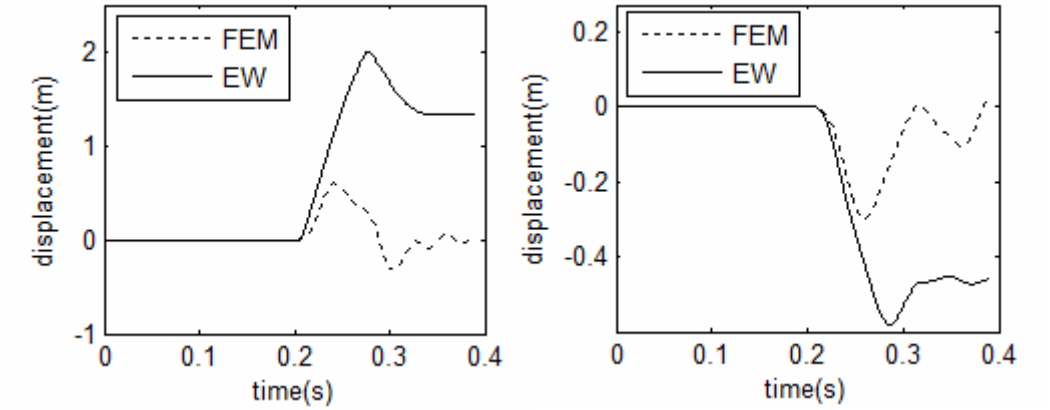

(c) Horizontal displacement at Point C (d) Vertical displacement at Point C

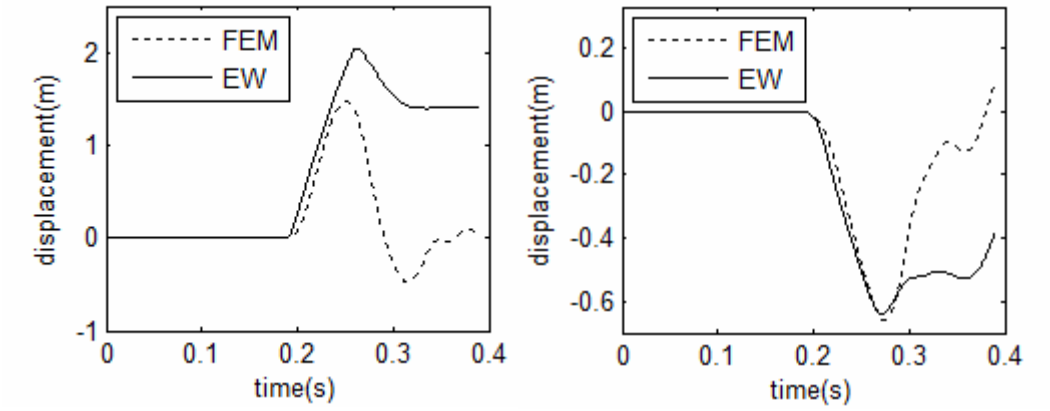

(e) Horizontal displacement at point D (f) Vertical displacement at Point D

Figure 4.7 Time history of the displacements for the horizontal load

To further confirm the effectiveness of the approach, another test was performed. Consider a new truncated domain that is twice as long as the one in the above discussion (Figure 4.8). In this new truncated domain the wave will not reach the boundary at 0.33s.

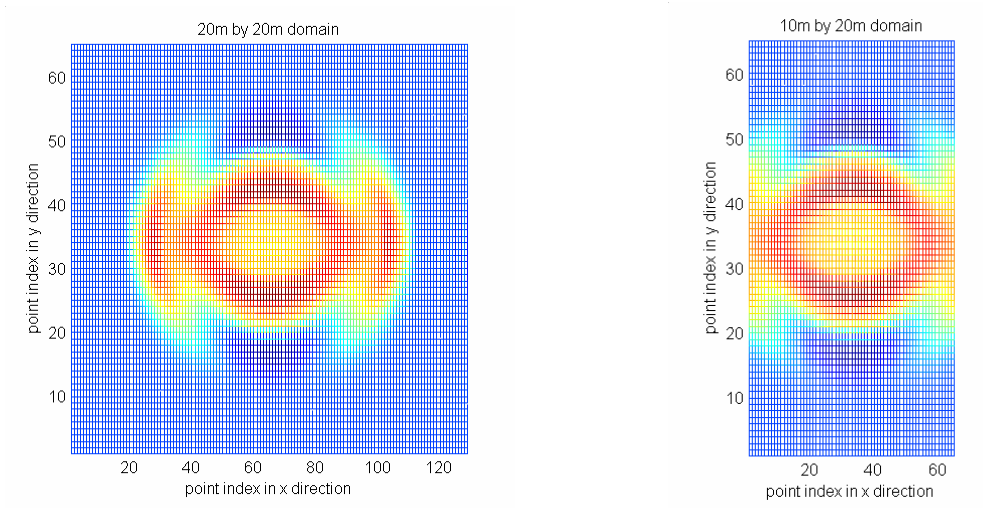

(a) Comparison of the horizontal displacements with different truncated sizes

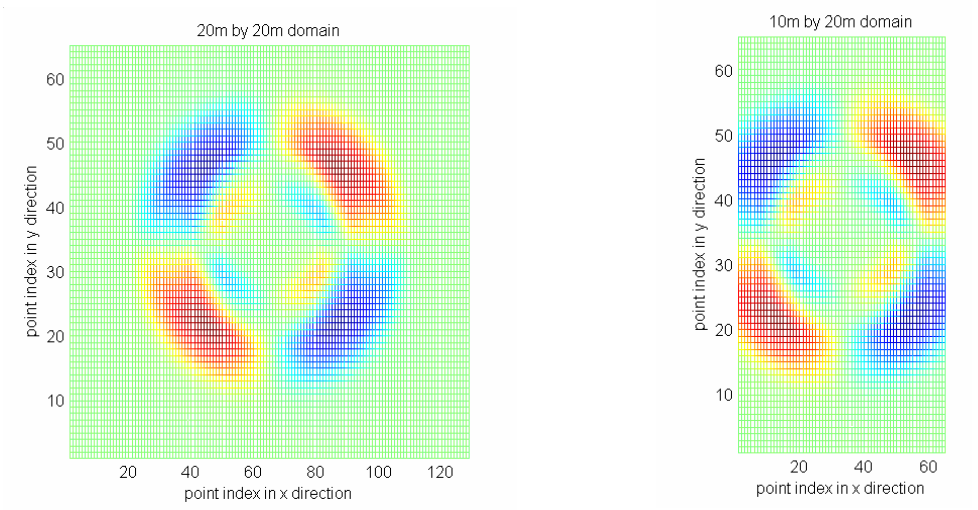

(b) Comparison of the vertical displacements with different truncated sizes

Figure 4.8 Time history of the displacements for the horizontal load

Then the results from the two domains should be identical within the area of the original truncated domain. Figure 4.8 shows the results. One can see that the displacement field in the *10m×20m* truncated domain is identical to the corresponding part in the *20m×20m* truncated domain.

4.4.2 Vertical area load

The same truncated domain in Section 4.4.1 is studied with the load direction changed to vertical. All parameters are the same. The horizontal and vertical displacements of the entire domain at *0.18s*, and *0.45s* for both methods are shown in Figure 4.9. At 0.18s, the wave is yet to reach the boundary so the two methods give the same pattern of the displacement field. At 0.45s, the wave has reached the boundary in the horizontal direction. Reflected waves can be observed in the finite element case.

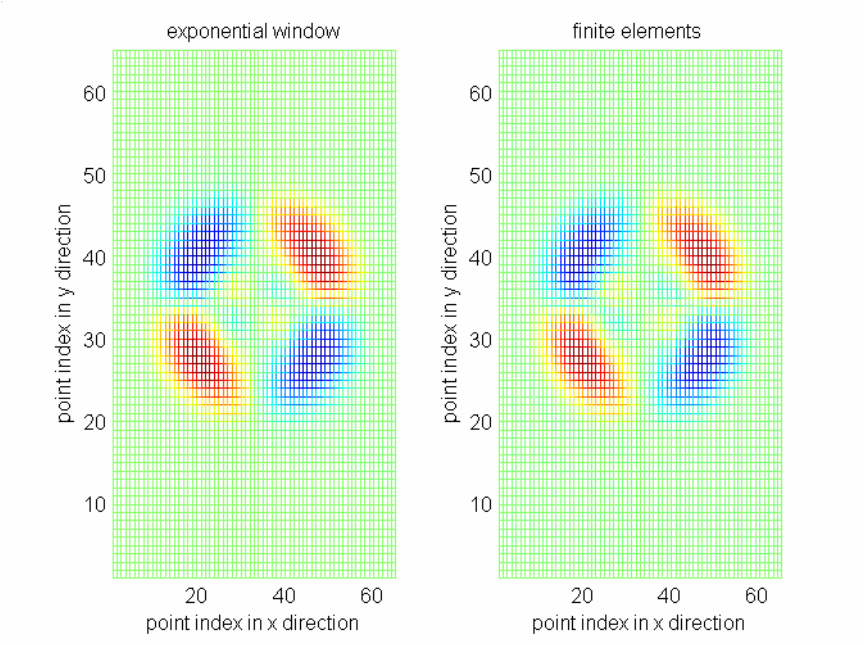

(a) Horizontal displacement at 0.18s

Figure 4.9 Displacement fields at different times for the vertical load

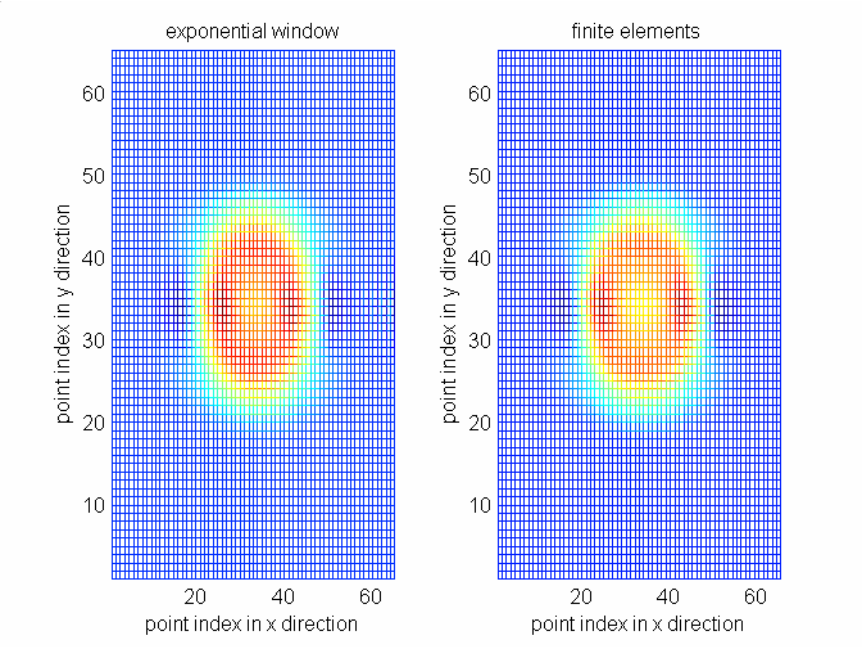

(b) Vertical displacement at 0.18s

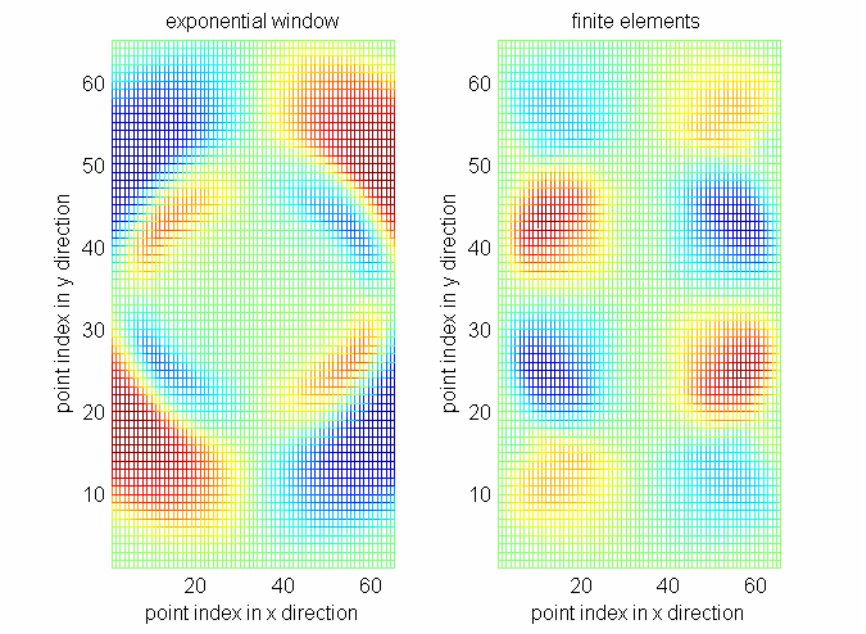

(c) Horizontal displacement at 0.45s

Figure 4.9 Continued

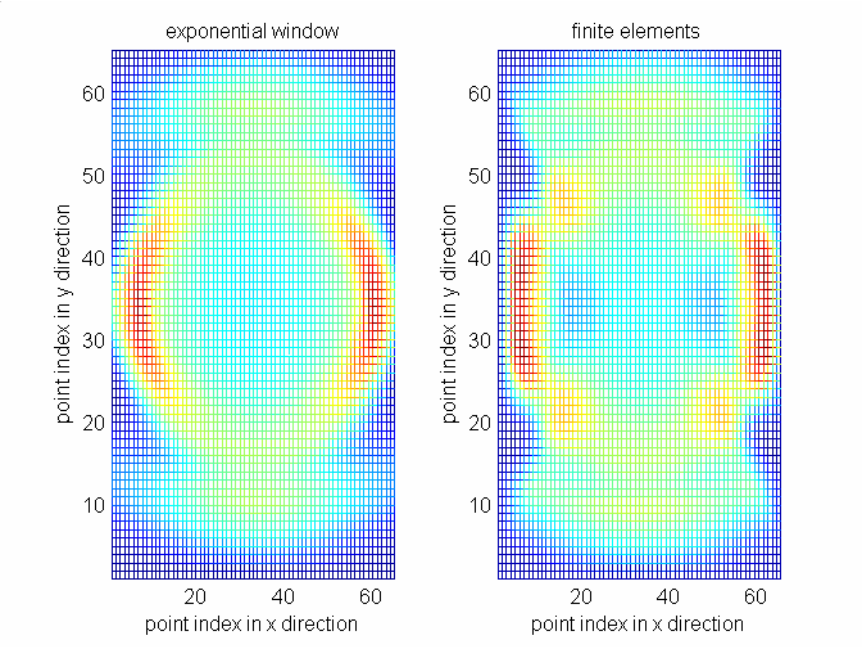

(d) Horizontal displacement at 0.45s

Figure 4.9 Continued

As in the previous subsection, the time history of the displacements at the four points is investigated. The horizontal displacement at Points *A* and *B* are zero so they are not listed here. The results are shown in Figure 4.10. Again, it demonstrates the effectiveness of the exponential window approach.

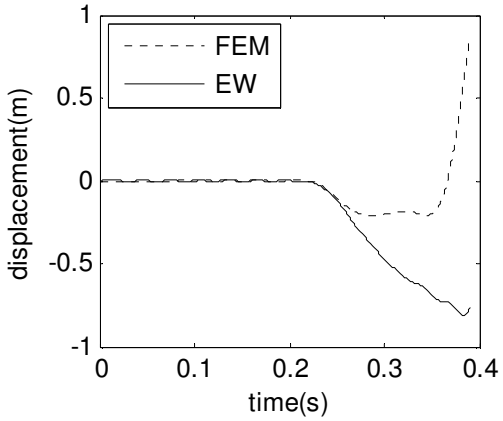

(a) Vertical displacement at Point A

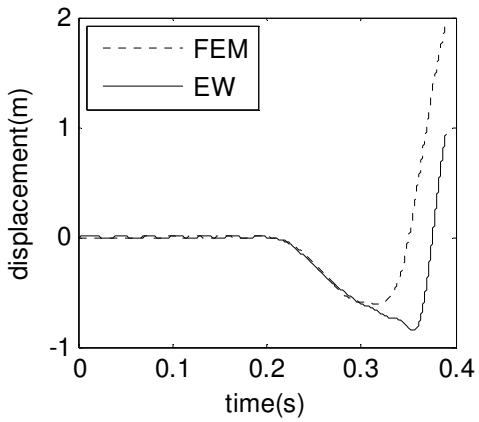

(b) Vertical displacement at Point B

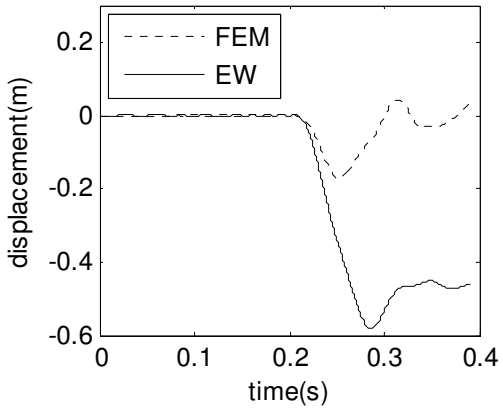

(c) Horizontal displacement at Point C

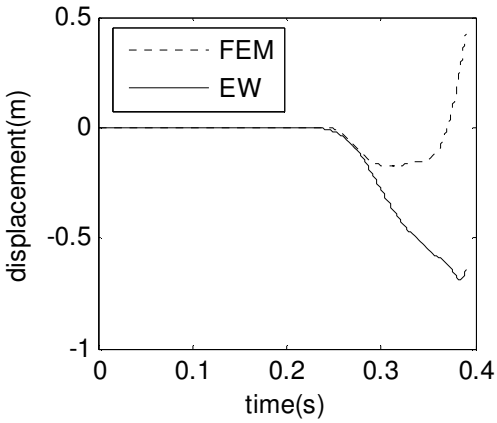

(d) Vertical displacement at Point C

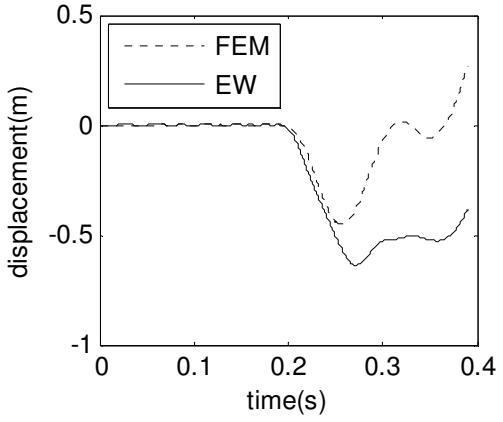

(e) Horizontal displacement at Point D

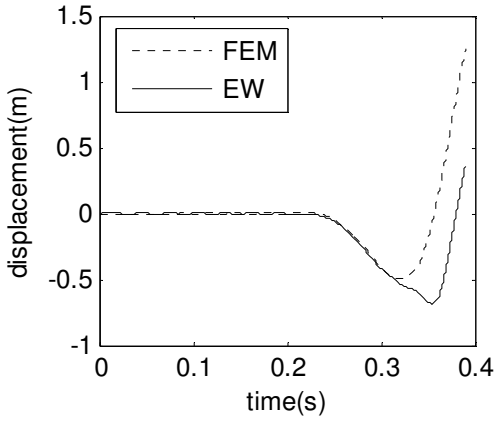

(f) Vertical displacement at Point D

Figure 4.10 Time history of the displacements for the vertical load

4.5 Line Loads on Free Surface

In this section, a line load on the free surface of an unbounded soil layer is studied (Refer to Figure 4.11). The soil layer rests on top of rock, which is considered to be rigid. In this case, besides P and SV wave, there will be another type of wave, namely, the surface or Rayleigh wave. Rayleigh waves propagate along the free surface and can be observed as a strong motion in an earthquake because their decay is slower than that of P-wave or S-waves, which are body waves.

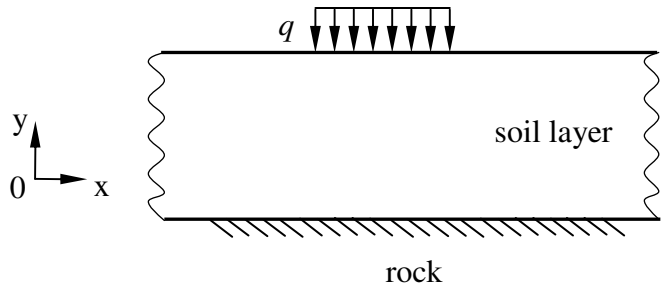

Figure 4.11 Vertical line load on free surface

The exponential window approach is applied in the horizontal direction. Figure 4.12 shows the truncated domain and the dimensions. The truncated boundary is represented by the center lines. The parameters are listed in Table 4.3.

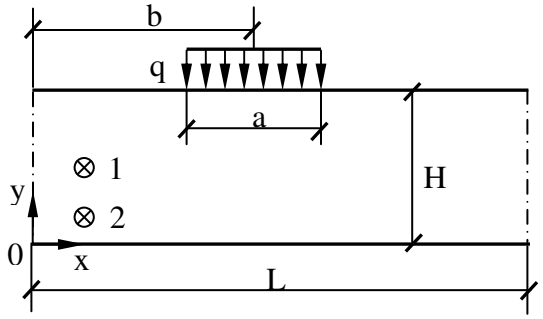

Figure 4.12 Geometric dimensions

Table 4.3 Parameters used in the line load case

Length of the domain	L	*20.0m*
Width of the domain	H	*10.0m*
Length of the loading area	a	*0.9375m*
Location of the loading area	b	*2.65625m*
Mass density	ρ	*22.0 kg/m^3*
P-wave velocity	c_p	*20 m/s*
S-wave velocity	c_s	*11.57 m/s*
Magnitude of the horizontal load	q	*1.0e+6 N/m^2*

The time history of the load is a rectangular pulse lasting from *3.0e-3s* to *6.0e-3s*. The truncated domain is meshed with 256 linear elements in the *y* direction and 256 points in the *x* direction to perform the Fourier transform. As a comparison, the same domain is also approximated with 128 third-order spectral finite elements in both *x* and *y* directions. The total number of nodes and DOFs in both cases is the same. In the finite element case, the left and right boundaries are modeled as free surfaces.

The vertical displacement field is recorded at *0.5s*. As shown in Figure 4.13, P, SV and Rayleigh waves can be observed. These waves can be distinguished by their arrival times. From Figure 4.13, all types of waves in the finite element method are reflected when they reach the left boundary while they are all absorbed in the exponential window approach. Figure 4.14 shows the horizontal displacement field at *0.5s*. Again, reflected waves can be observed in the results from the finite element method while all waves are absorbed in the exponential window approach.

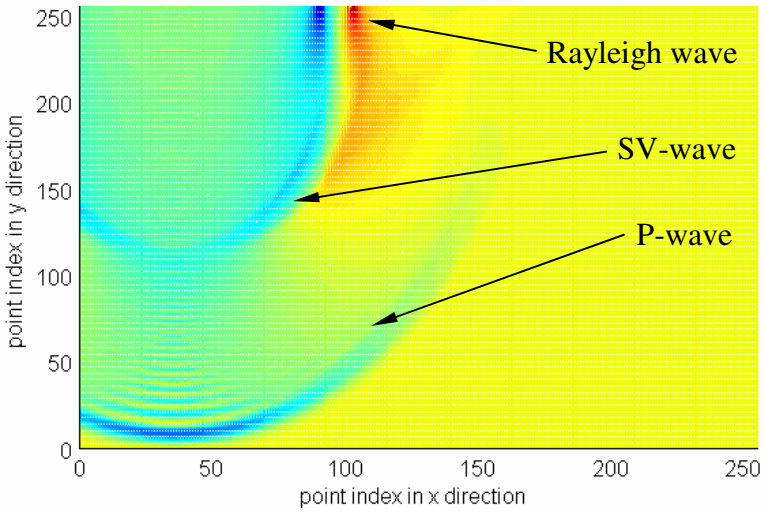

(a) Results from the exponential window approach

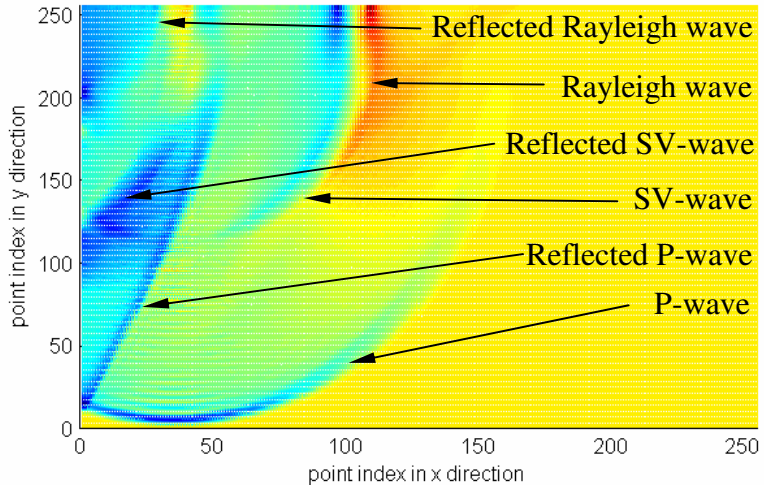

(b) Results from the finite element method

Figure 4.13 Vertical displacement field of a line load at 0.5s

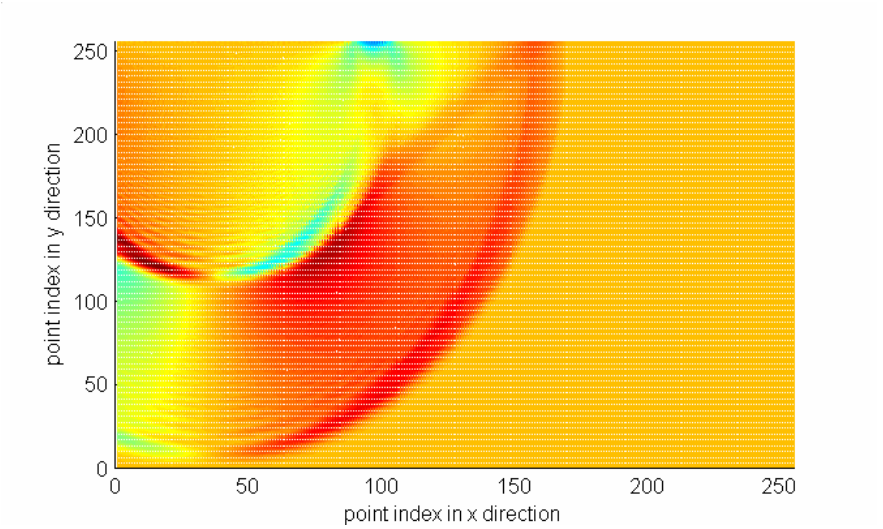

(a) Results from the exponential window approach

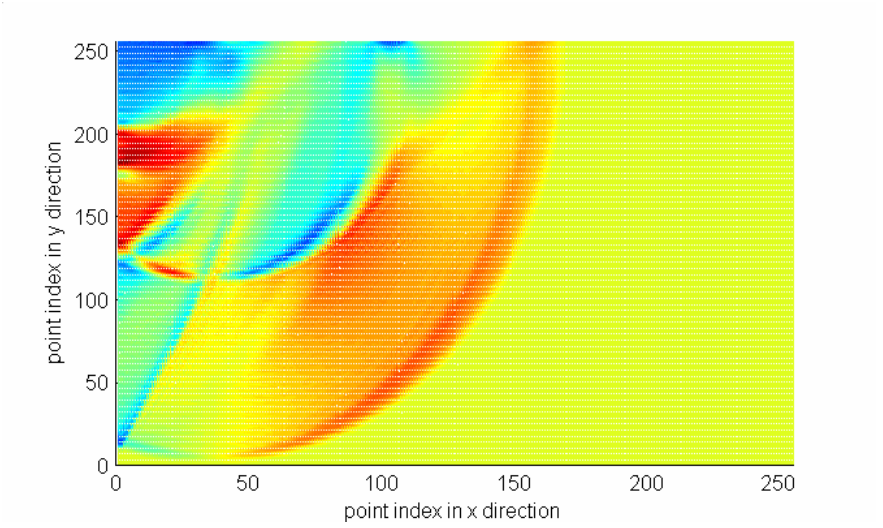

(b) Results from the finite element method

Figure 4.14 Horizontal displacement field of a line load at 0.5s

Time histories of the displacements at specific locations were also obtained. The coordinates of points 1 and 2 in Figure 4.12 are (1.72, 9.53) and (1.72, 9.22), respectively. Horizontal and vertical displacements at these two points are shown in Figures 4.15 and 4.16.

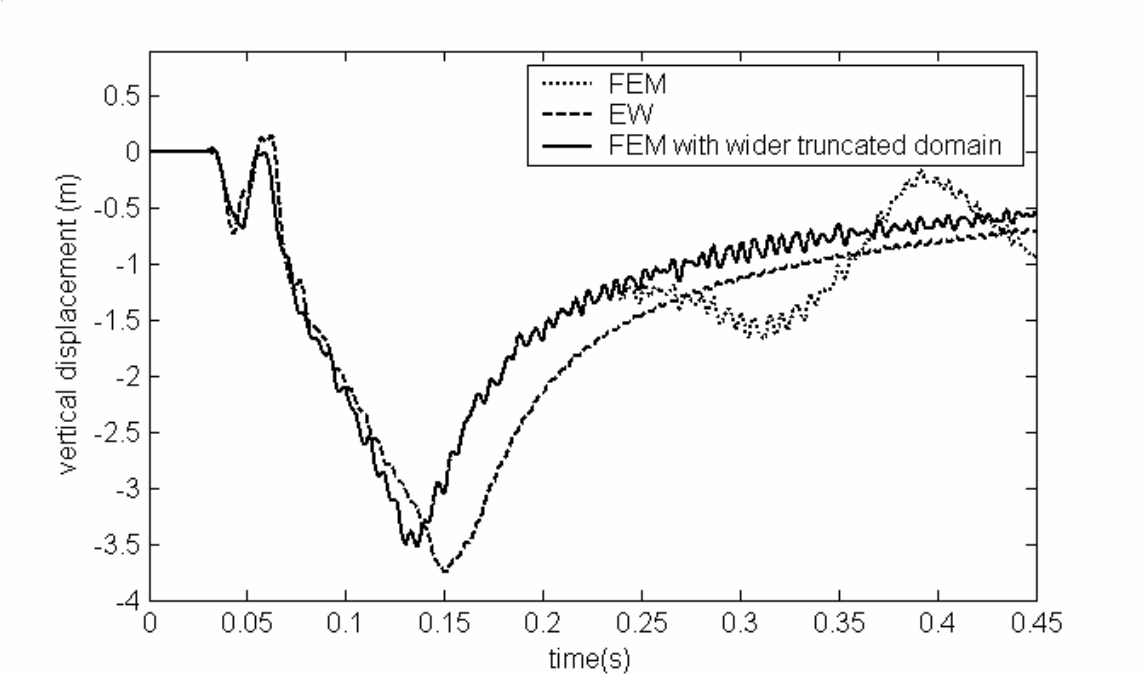

(a) Vertical displacement at Point 1

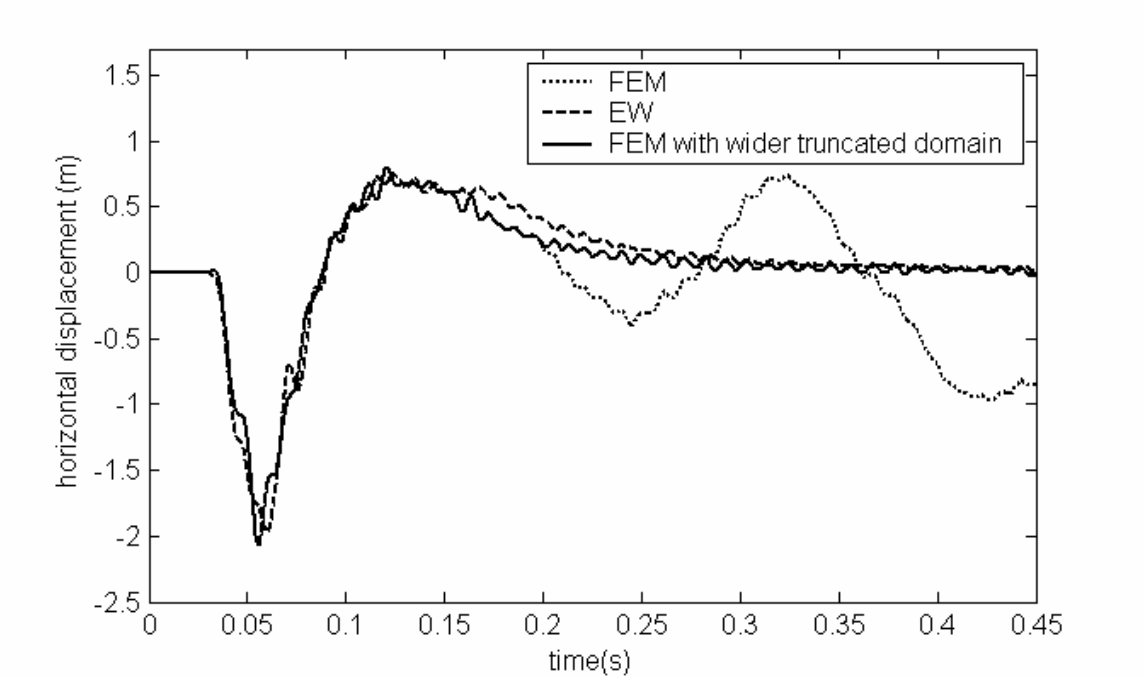

(b) Horizontal displacement at Point 1

Figure 4.15 Displacements at Point 1

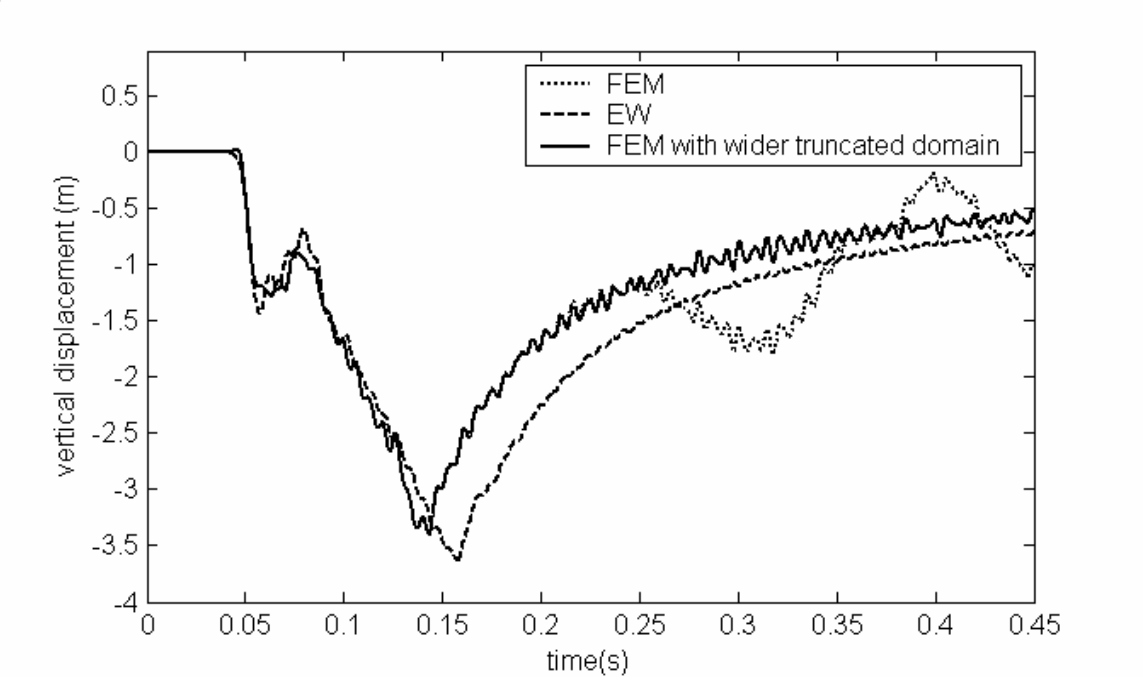

(a) Vertical displacement at Point 2

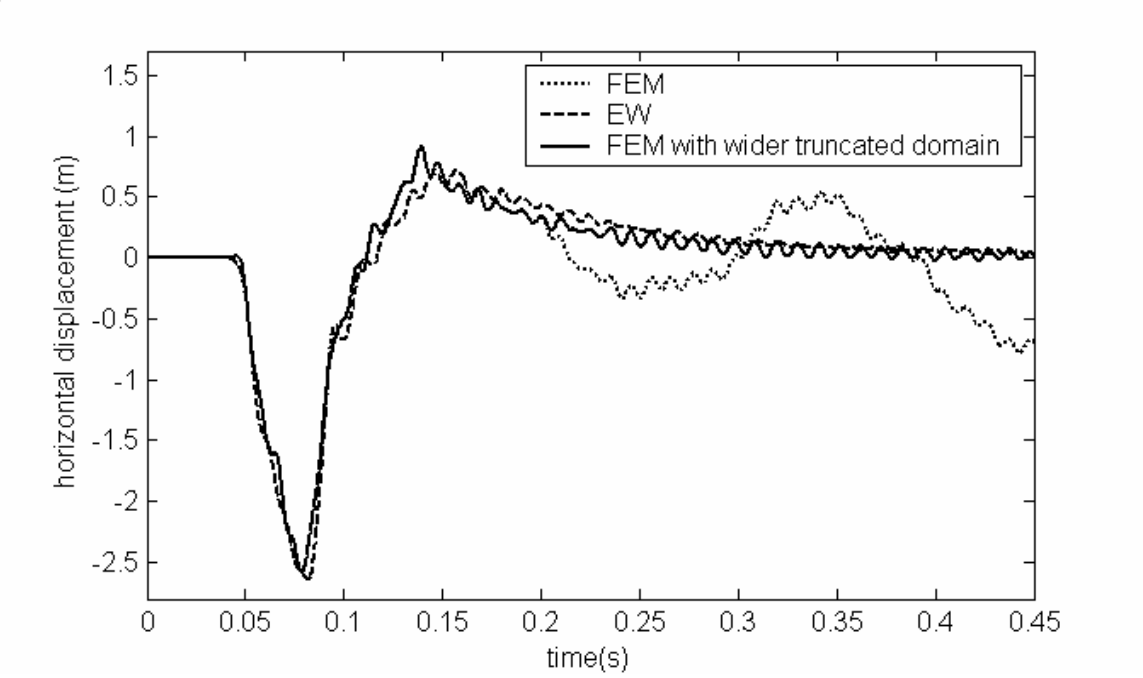

(b) Horizontal displacement at Point 2

Figure 4.16 Displacements at Point 2

In Figure 4.15 and 4.16, “EM” stands for “the exponential window approach”. To confirm the effectiveness of the exponential window, the finite element method was also applied to a wider truncated domain so that within the time range studied (0.45s in the figures), there are no reflected waves at Points 1 and 2. It can be seen that the results from the finite element method with the wider truncated domain, represented by solid lines, match very well the results from the exponential window approach, represented by dashed lines, for the horizontal displacements. For the vertical displacements, they match reasonably well with small errors. The results from the finite element solution with the original truncated domain, as represented by the dotted lines, start to deviate from the other two, at the time of arrival of the reflected waves.

The difference shown in the vertical displacements between the exponential window approach and the finite element method needs to be further studied and the wiggles shown in the results from the finite element method are also a matter of interest. But these two issues are not the main concern here because the purpose was to explore the absorbing property of the exponential window method, which was validated through the examples.

CHAPTER V

WAVES IN AN UNBOUNDED LAYER

5.1 Overview

The topic in this chapter is 3D wave propagation in an unbounded layer (Figure 5.1). The layer is infinite in the *x* and *y* directions but finite in the *z* direction. The boundary conditions on the top and bottom surface in the *z* direction are physical. For the case of a layer or layers of soil resting on rigid rock, the top surface would have specified tractions while the bottom surface is fixed. In Figure 5.1, the bottom surface is fixed while uniformly distributed loads are located in the shaded area on the top surface.

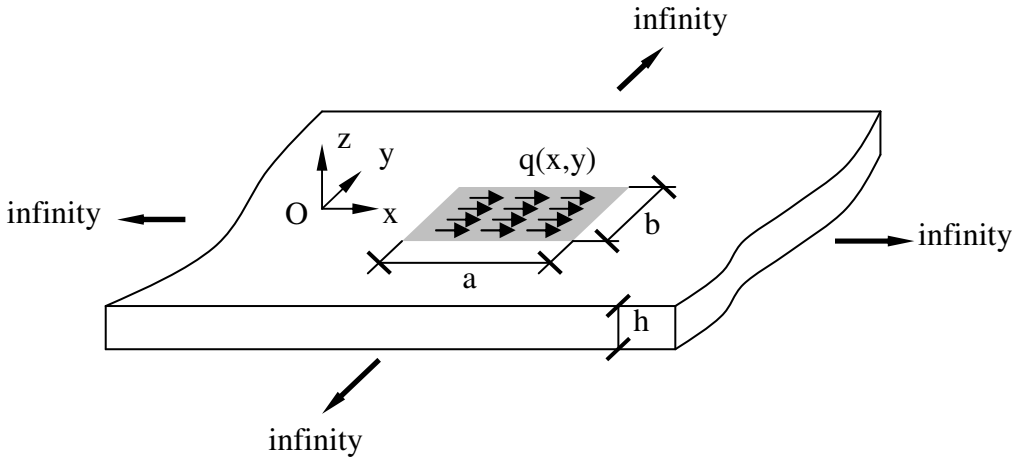

Figure 5.1 The infinite layer

The procedure followed is analogous to the one described for the 2D case in Chapter IV. The displacement field is approximated by a finite element expansion in the directions where the domain is finite and a modified equation of motion is derived. In this case, the finite element expansion is applied in the *z* direction. The layer is infinitely long in the *x* and *y* directions so it is truncated in these two directions in which the

exponential window is applied. The 2D case in Chapter IV could be applied to certain types of 3D problems. The problem addressed in this chapter is different from the one in Chapter IV in that it employs a 2D Fourier transform in the *x*-*y* plane. Applications can be found in soil-structure interaction problems where soil is treated as a layered medium. The procedure may also find applications in layered composite materials where a number of layers are bonded together to create desired mechanical properties.

5.2 Modified Equation of Motion

The equations of motion for general 3D wave propagation are

$$(\lambda+\mu)\left(\frac{\partial^2 u}{\partial x^2}+\frac{\partial^2 v}{\partial x\partial y}+\frac{\partial^2 w}{\partial x\partial z}\right)+\mu\nabla^2 u+f_x=\rho\frac{\partial^2 u}{\partial t^2} \tag{5.1a}$$

$$(\lambda+\mu)\left(\frac{\partial^2 u}{\partial y\partial x}+\frac{\partial^2 v}{\partial y^2}+\frac{\partial^2 w}{\partial y\partial z}\right)+\mu\nabla^2 v+f_y=\rho\frac{\partial^2 v}{\partial t^2} \tag{5.1b}$$

$$(\lambda+\mu)\left(\frac{\partial^2 u}{\partial z\partial x}+\frac{\partial^2 v}{\partial z\partial y}+\frac{\partial^2 w}{\partial z^2}\right)+\mu\nabla^2 w+f_z=\rho\frac{\partial^2 w}{\partial t^2} \tag{5.1c}$$

where

ρ = mass density

λ, and μ = Lame constants

u, v, and w = displacements in x, y and z directions, respectively

f_x, f_y, and f_z = body force in x, y and z directions, respectively

$\nabla^2=\frac{\partial^2}{\partial x^2}+\frac{\partial^2}{\partial y^2}+\frac{\partial^2}{\partial z^2}$, the Laplace operator

Consider a sub-layer taken from the unbounded layer in Figure 5.1. The displacement vector is $\mathbf{U}=\{u,v,w\}^T$. The nodal displacement vector is $\mathbf{V}=\{u_1,v_1,w_1,u_2,v_2,w_2\}^T$ with u_1, v_1 and w_1 as displacements at the top and u_2, v_2 and w_2 at the bottom, respectively. The force vector is $\mathbf{T}=\{p_1,q_1,r_1,p_2,q_2,r_2\}^T$ with p_1, q_1, and r_1, as tractions at the top and p_2, q_2 and r_1 at the bottom, respectively (Figure 5.2.)

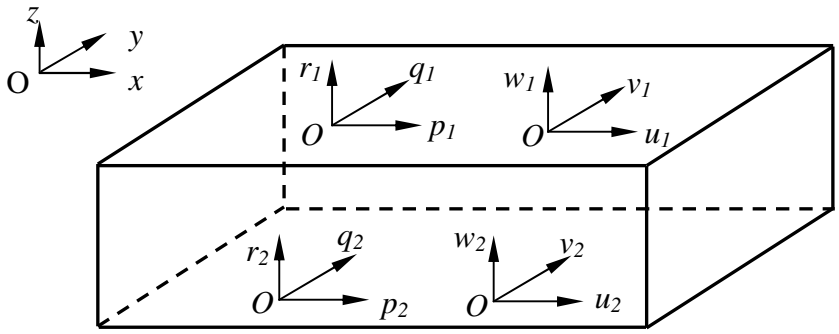

Figure 5.2 Definition of displacements and forces

Calling $\boldsymbol{\sigma} = \{\sigma_{xx}, \sigma_{yy}, \sigma_{zz}, \sigma_{yz}, \sigma_{xz}, \sigma_{xy}\}^T$ and $\boldsymbol{\varepsilon} = \{\varepsilon_{xx}, \varepsilon_{yy}, \varepsilon_{zz}, \varepsilon_{yz}, \varepsilon_{xz}, \varepsilon_{xy}\}^T$, the general Hooke's law for the isotropic material is

$$\boldsymbol{\sigma} = \mathbf{C}\boldsymbol{\varepsilon} \text{ with } \mathbf{C} = \begin{bmatrix} \lambda+2\mu & \lambda & \lambda & 0 & 0 & 0 \\ \lambda & \lambda+2\mu & \lambda & 0 & 0 & 0 \\ \lambda & \lambda & \lambda+2\mu & 0 & 0 & 0 \\ 0 & 0 & 0 & \mu & 0 & 0 \\ 0 & 0 & 0 & 0 & \mu & 0 \\ 0 & 0 & 0 & 0 & 0 & \mu \end{bmatrix}.$$

The strains and displacements are connected by

$$\boldsymbol{\varepsilon} = \mathbf{L}^T\mathbf{U} \text{ with } \mathbf{L} = \begin{bmatrix} \frac{\partial}{\partial x} & 0 & 0 & 0 & \frac{\partial}{\partial z} & \frac{\partial}{\partial y} \\ 0 & \frac{\partial}{\partial y} & 0 & \frac{\partial}{\partial z} & 0 & \frac{\partial}{\partial x} \\ 0 & 0 & \frac{\partial}{\partial z} & \frac{\partial}{\partial y} & \frac{\partial}{\partial x} & 0 \end{bmatrix}.$$

The displacement field can be written as

$$\mathbf{U}(x, y, z, t) = \mathbf{N}(z)\mathbf{V}(x, y, t) \tag{5.2}$$

The matrix **N** is

$$\mathbf{N}(y)=\begin{bmatrix} \frac{h-z}{h} & 0 & \frac{z}{h} & 0 \\ 0 & \frac{h-z}{h} & 0 & \frac{z}{h} \end{bmatrix}$$ for linear elements and

Applying the principle of virtual work to the finite element layer,

$$\delta \mathbf{V}^{*T}\mathbf{T}=\int_0^h \delta \boldsymbol{\varepsilon}^{*T}\boldsymbol{\sigma} dz \tag{5.3}$$

The superscript in Equation (5.3) stands for conjugate operation. The reason for introducing this more general form of virtual work is the same as in the 2D case in Chapter IV. With the conjugate operation, anti-symmetric first-order terms are created. The mass and stiffness matrices are

$$\mathbf{M}=\int_0^h \rho \mathbf{N}^T\mathbf{N} dz \tag{5.4}$$

$$\mathbf{K}=\int_0^h \mathbf{N}^T\mathbf{L}^{*T}\mathbf{C}\mathbf{L}\mathbf{N} dz \tag{5.5}$$

The stiffness matrix can be decomposed into matrices associated with the second-order, first-order and constant terms, respectively. After some algebraic manipulations, the modified equation of motion can be derived as the following.

$$-\mathbf{A}_{\mathrm{xx}}\frac{\partial^2\mathbf{V}}{\partial x^2}-\mathbf{A}_{\mathrm{xy}}\frac{\partial^2\mathbf{V}}{\partial x\partial y}-\mathbf{A}_{\mathrm{yy}}\frac{\partial^2\mathbf{V}}{\partial y^2}+\mathbf{A}_{\mathrm{x}}\frac{\partial\mathbf{V}}{\partial x}+\mathbf{A}_{\mathrm{y}}\frac{\partial\mathbf{V}}{\partial y}+\mathbf{A}_0\mathbf{V}+\mathbf{M}\frac{\partial^2\mathbf{V}}{\partial t^2}=\mathbf{T} \tag{5.6}$$

There are two first-order terms in the equation. As stated in Chapter II, these first-order terms do not indicate the existence of damping. For linear elements, the matrices are listed below for ready reference. Note that $\boldsymbol{A}_{\mathrm{x}}$ and $\boldsymbol{A}_{\mathrm{y}}$ are anti-symmetric.

$$\mathbf{A}_{xx} = \begin{bmatrix} \frac{h(\lambda+2\mu)}{3} & 0 & 0 & \frac{h(\lambda+2\mu)}{6} & 0 & 0 \\ 0 & \frac{h\mu}{3} & 0 & 0 & \frac{h\mu}{6} & 0 \\ 0 & 0 & \frac{h\mu}{3} & 0 & 0 & \frac{h\mu}{6} \\ \frac{h(\lambda+2\mu)}{3} & 0 & 0 & \frac{h(\lambda+2\mu)}{6} & 0 & 0 \\ 0 & \frac{h\mu}{6} & 0 & 0 & \frac{h\mu}{3} & 0 \\ 0 & 0 & \frac{h\mu}{6} & 0 & 0 & \frac{h\mu}{3} \end{bmatrix}$$

$$\mathbf{A}_{xy} = \begin{bmatrix} 0 & \frac{h(\lambda+\mu)}{3} & 0 & 0 & \frac{h(\lambda+\mu)}{6} & 0 \\ \frac{h(\lambda+\mu)}{3} & 0 & 0 & \frac{h(\lambda+\mu)}{6} & 0 & 0 \\ 0 & 0 & 0 & 0 & 0 & 0 \\ 0 & \frac{h(\lambda+\mu)}{6} & 0 & 0 & \frac{h(\lambda+\mu)}{3} & 0 \\ \frac{h(\lambda+\mu)}{6} & 0 & 0 & \frac{h(\lambda+\mu)}{3} & 0 & 0 \\ 0 & 0 & 0 & 0 & 0 & 0 \end{bmatrix}$$

$$\mathbf{A}_{xx} = \begin{bmatrix} \frac{h\mu}{3} & 0 & 0 & \frac{h\mu}{6} & 0 & 0 \\ 0 & \frac{h(\lambda+2\mu)}{3} & 0 & 0 & \frac{h(\lambda+2\mu)}{6} & 0 \\ 0 & 0 & \frac{h\mu}{3} & 0 & 0 & \frac{h\mu}{6} \\ \frac{h\mu}{6} & 0 & 0 & \frac{h\mu}{3} & 0 & 0 \\ 0 & \frac{h(\lambda+2\mu)}{6} & 0 & 0 & \frac{h(\lambda+2\mu)}{3} & 0 \\ 0 & 0 & \frac{h\mu}{6} & 0 & 0 & \frac{h\mu}{3} \end{bmatrix}$$

$$\mathbf{A}_x = \begin{bmatrix} 0 & 0 & \frac{\mu-\lambda}{2} & 0 & 0 & \frac{\mu+\lambda}{2} \\ 0 & 0 & 0 & 0 & 0 & 0 \\ \frac{\lambda-\mu}{2} & 0 & 0 & \frac{\mu+\lambda}{2} & 0 & 0 \\ 0 & 0 & -\frac{\mu+\lambda}{2} & 0 & 0 & \frac{\lambda-\mu}{2} \\ 0 & 0 & 0 & 0 & 0 & 0 \\ -\frac{\mu+\lambda}{2} & 0 & 0 & \frac{\mu-\lambda}{2} & 0 & 0 \end{bmatrix}$$

$$\mathbf{A}_y = \begin{bmatrix} 0 & 0 & 0 & 0 & 0 & 0 \\ 0 & 0 & \frac{\mu-\lambda}{2} & 0 & 0 & \frac{\mu+\lambda}{2} \\ 0 & \frac{\lambda-\mu}{2} & 0 & 0 & \frac{\mu+\lambda}{2} & 0 \\ 0 & 0 & 0 & 0 & 0 & 0 \\ 0 & 0 & -\frac{\mu+\lambda}{2} & 0 & 0 & \frac{\lambda-\mu}{2} \\ 0 & -\frac{\mu+\lambda}{2} & 0 & 0 & \frac{\mu-\lambda}{2} & 0 \end{bmatrix}$$

$$\mathbf{M} = \begin{bmatrix} \frac{\rho h}{3} & 0 & 0 & \frac{\rho h}{6} & 0 & 0 \\ 0 & \frac{\rho h}{3} & 0 & 0 & \frac{\rho h}{6} & 0 \\ 0 & 0 & \frac{\rho h}{3} & 0 & 0 & \frac{\rho h}{6} \\ \frac{\rho h}{6} & 0 & 0 & \frac{\rho h}{3} & 0 & 0 \\ 0 & \frac{\rho h}{6} & 0 & 0 & \frac{\rho h}{3} & 0 \\ 0 & 0 & \frac{\rho h}{6} & 0 & 0 & \frac{\rho h}{3} \end{bmatrix}$$

5.3 The Complex Wave Number Shift

Performing the Fourier transform with respect to the space coordinates x and y, one obtains the equation in the wave number-time domain

$$(k^2\mathbf{A}_{xx} + l^2\mathbf{A}_{yy} + kl\mathbf{A}_{xy} + jk\mathbf{A}_x + jl\mathbf{A}_y + \mathbf{A}_0)\bar{\mathbf{V}}(k,l,t) + \mathbf{M}\frac{\partial^2 \bar{\mathbf{V}}(k,l,t)}{\partial t^2} = \bar{\mathbf{T}}(k,l,t) \tag{5.7}$$

where

k = wave number in the x direction

l = wave number in the y direction

j = unit imaginary number $\sqrt{-1}$

$\bar{\mathbf{V}}$ = Fourier transform of the displacement

$\bar{\mathbf{T}}$ = Fourier transform of the load

The complex wave number is defined by

$$k' = k + j\eta \tag{5.8a}$$

$$l' = l + j\mu \tag{5.8b}$$

Substituting Equation (5.8) into Equation (5.7), one has

$$[(k'-j\eta)^2\mathbf{A}_{xx} + (l'-j\mu)^2\mathbf{A}_{yy} + (k'-j\eta)(l'-j\mu)\mathbf{A}_{xy} + j(k'-j\eta)\mathbf{A}_x + j(l'-j\mu)\mathbf{A}_y + \mathbf{A}_0]\bar{\mathbf{V}}(k'-j\eta,l'-j\mu,t) + \mathbf{M}\frac{\partial^2 \bar{\mathbf{V}}(k'-j\eta,l'-j\mu,t)}{\partial t^2} = \bar{\mathbf{T}}(k'-j\eta,l'-j\mu,t) \tag{5.9}$$

To find the load in the shifted wave number domain, one needs to impose the decaying window in the space domain before performing the Fourier transform

$$\bar{\mathbf{T}}(k'-j\eta,l'-j\mu,t) = \int_{-\infty}^{\infty}\int_{-\infty}^{\infty} \mathbf{T}(x,t)e^{-\eta x-\mu y}e^{-j(kx+ly)}dxdy \tag{5.10}$$

To find the displacement in the original system, one needs to impose the rising window after obtaining the displacement in the space domain.

$$\mathbf{V}(x,y,t) = e^{\eta x+\mu y}\int_{-\infty}^{\infty}\int_{-\infty}^{\infty}\bar{\mathbf{V}}(x,y,t)e^{j(kx+\mu y)}dkdl \tag{5.11}$$

Defining the stiffness matrix in the wave number domain

$$\begin{aligned}\mathbf{K} &= (k'-j\eta)^2\mathbf{A}_{xx} + (l'-j\mu)^2\mathbf{A}_{yy} + (k'-j\eta)(l'-j\mu)\mathbf{A}_{xy} + j(k'-j\eta)\mathbf{A}_x \\ &+ j(l'-j\mu)\mathbf{A}_y + \mathbf{A}_0\end{aligned} \tag{5.12}$$

Equation (5.7) can be briefly written as

$$\mathbf{K}\bar{\mathbf{V}} + \mathbf{M}\frac{\partial^2\bar{\mathbf{V}}}{\partial t^2} = \bar{\mathbf{T}} \tag{5.13}$$

To solve Equation (5.13) with respect to time, an explicit finite difference scheme was implemented. The scheme was described in detail in Chapter II and is not repeated here.

5.4 A Numerical Example

To validate the method, a numerical experiment is carried out to demonstrate the effectiveness of the exponential window. The unbounded layer in Figure 5.1 is truncated so that the loading area is located at the center of the truncated domain (Figure 5.3). The time history of the load is a rectangular pulse lasting from *0.003s* to *0.006s*.

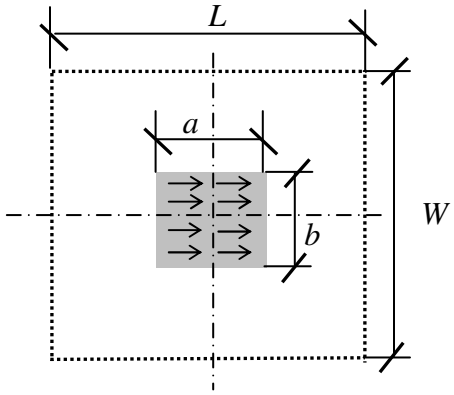

Figure 5.3 Absorbing boundary and finite element method settings

The parameters are listed in Table 5.1. Sixty four points are used in the x and y directions and 32 linear finite elements are used in the z direction. The total number of nodes is $64*64*33=135168$. The total number of DOFs is $3*135168=405504$. Figures 5.4 and 5.5 show the displacement fields at the top surface in the x and y directions at *0.45s*.

Table 5.1 Parameters used in the 3D numerical example

Length of the domain	L	*10.0m*
Width of the domain	W	*10.0m*
Thickness of the domain	h	*10.0m*
Length of the loading area	a	*1.094m*
Width of the loading area	b	*1.094m*
Mass density	ρ	*22.0 kg/m^3*
P-wave velocity	c_p	*20.0 m/s*
S-wave velocity	c_s	*10.0 m/s*
Magnitude of the horizontal load	q	*1.0e+3 N/m^2*

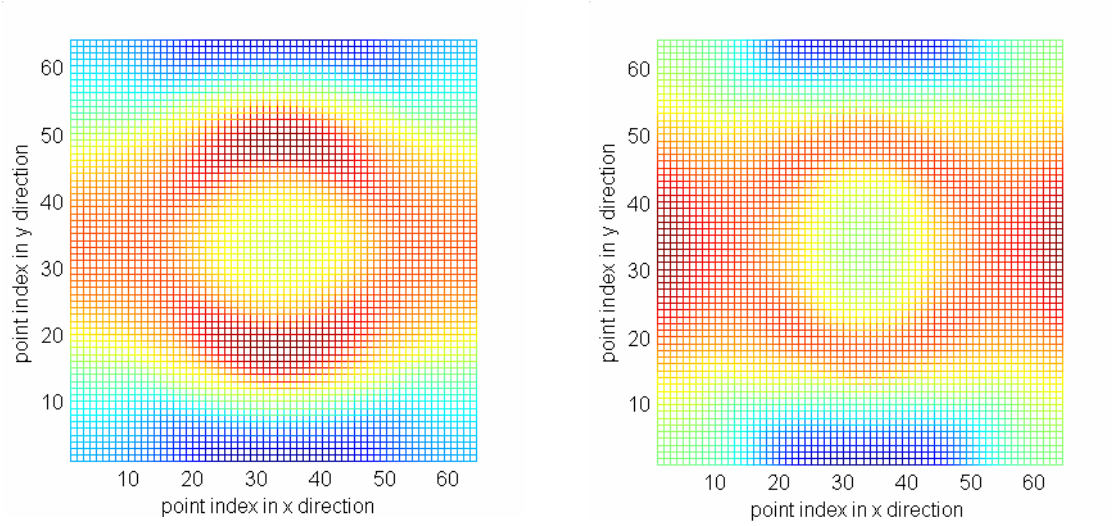

(a) With exponential window (b) Without exponential window

Figure 5.4 Displacements on the top surface in the x direction at *0.45s*

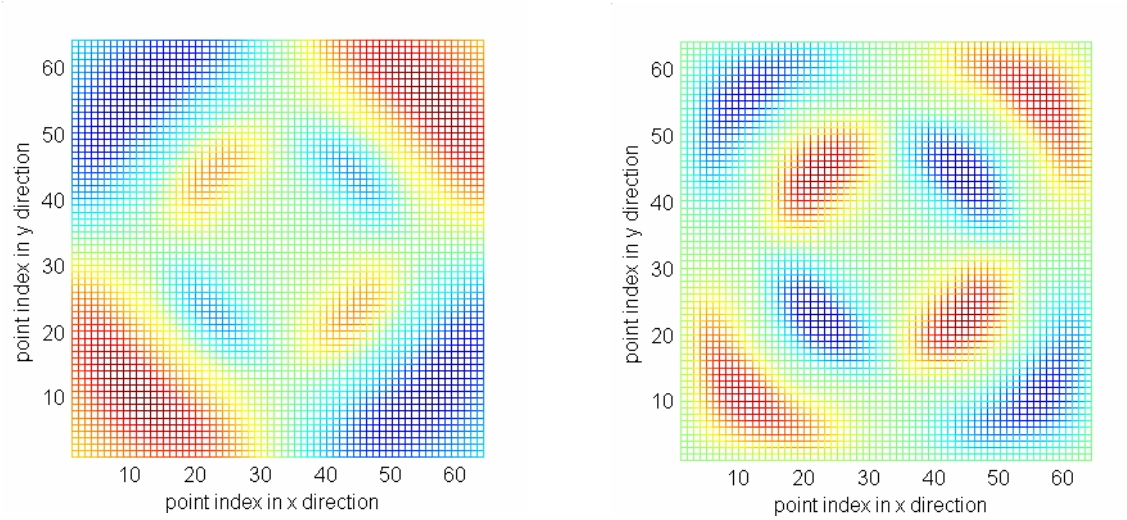

(a) With exponential window (b) Without exponential window

Figure 5.5 Displacements on the top surface in the *y* direction at *0.45s*

Figures 5.4 and 5.5 show that there are no reflected waves when the exponential window is employed. The displacement in the *y* direction is anti-symmetric as expected. As a comparison, a larger truncated domain of *16m* by *16m* was studied. The number of nodes was increased accordingly so that the size of the elements remained the same. Other parameters were also the same. The displacements at *0.45s* are shown in Figure 5.6. At this time, the waves have not reached the boundaries. It can be seen that the pattern in Figure 5.6 matches very well the pattern with the exponential window in Figures 5.4 and 5.5. This indicates that the exponential window helps to absorb the waves on the truncated boundaries very well.

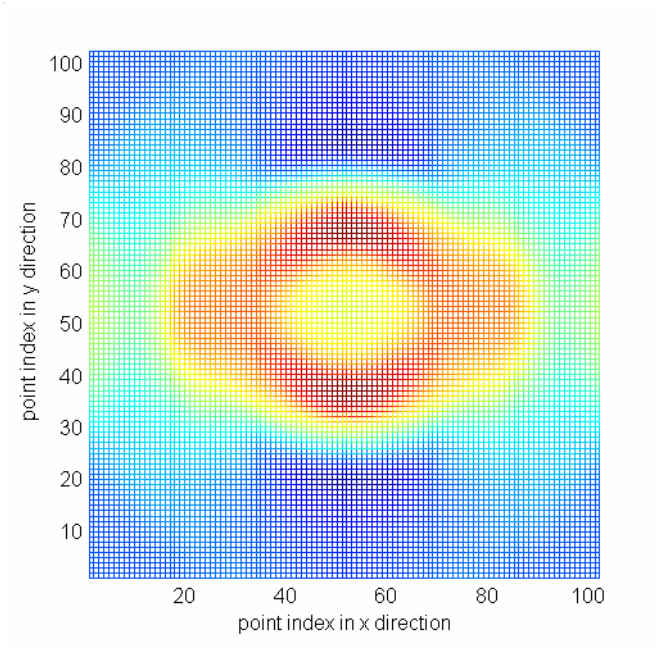

(a) Displacement in the *x* direction

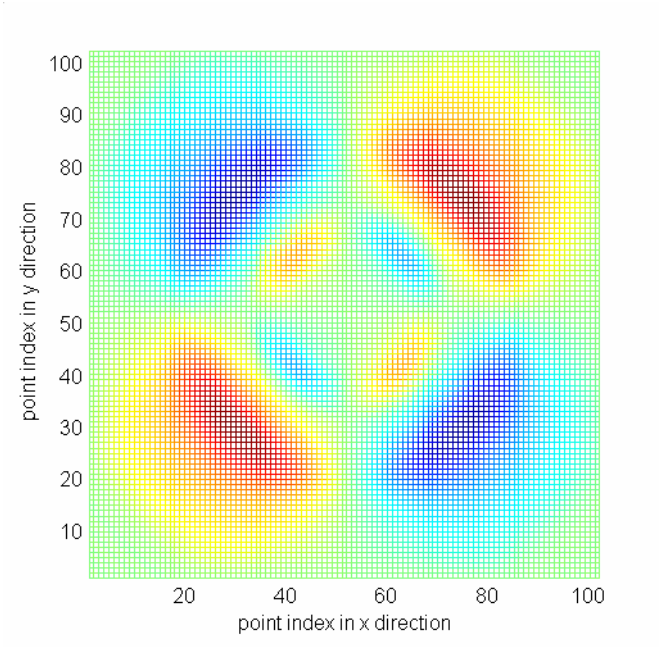

(b) Displacement in the *y* direction

Figure 5.6 Displacements in a larger truncated domain at *0.45s*

The time histories of displacements at two points located on the top surface and on the truncated boundary were also recorded. The position of the two points is shown in Figure 5.7. $a = b = 0.625m$.

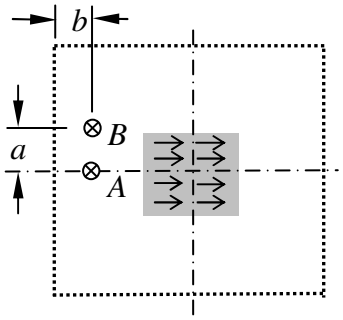

Figure 5.7 Location of Points A and B

Figure 5.8 shows the displacement histories. The displacements obtained with and without the exponential window are compared with the displacement in the larger truncated domain. The result with the exponential window matches very well that with the larger truncate domain. The result without the exponential window, however, deviates from the other two, illustrating the effective absorption on the boundary with the exponential window.

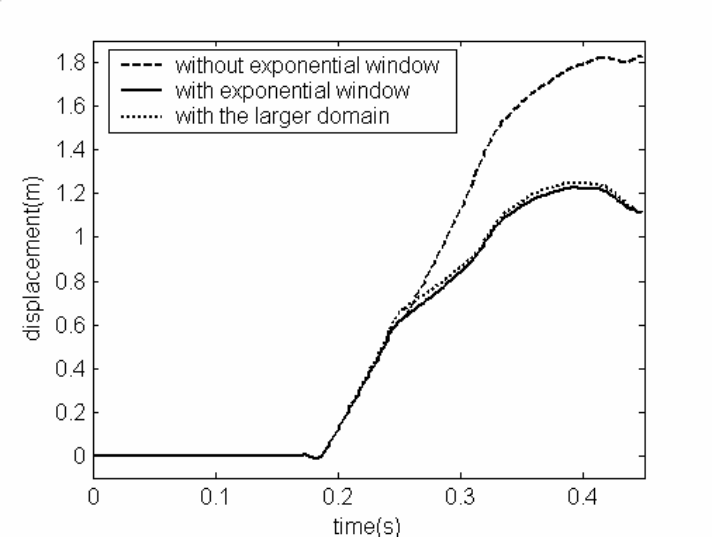

(a) Displacement in the *x* direction at Point A

Figure 5.8 Displacements with and without the exponential window

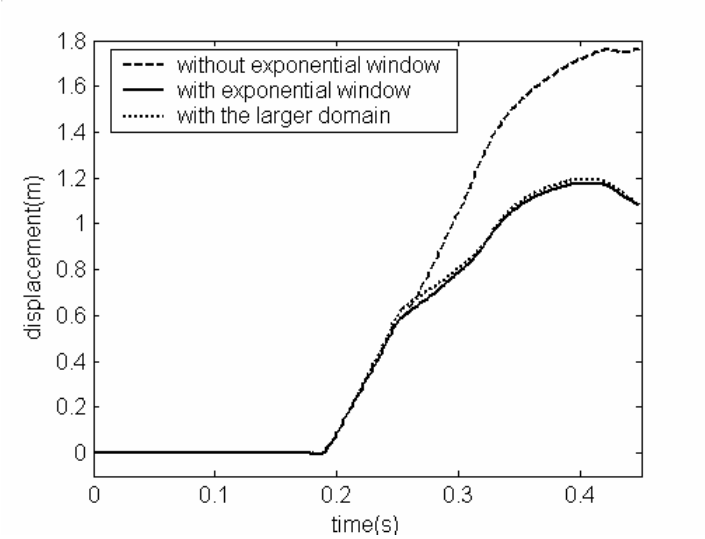

(b) Displacement in the *x* direction at Point B

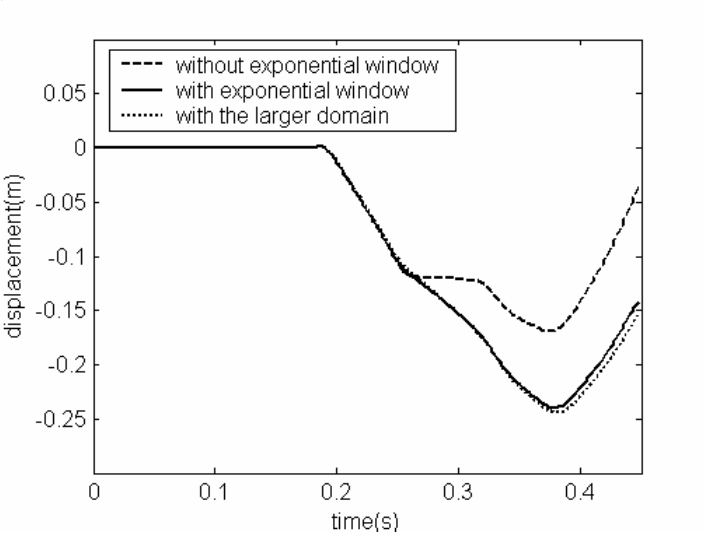

(c) Displacement in the *y* direction at Point B

Figure 5.8 Continued

CHAPTER VI

SUMMARY, CONCLUSIONS AND RECOMMENDATIONS

6.1 Summary

In this dissertation, the application of the exponential window method to solve wave propagation problems in an unbounded medium has been investigated. Wave propagation in unbounded media is a topic of both theoretical and practical significance with a wide range of applications in seismology, oceanography, and various engineering disciplines. Many researchers have studied this topic and developed solution approaches with a variety of underlying mechanisms. The purpose of this study was to investigate an efficient alternative based on the use of the exponential window method.

The idea for the approach is borrowed from the exponential window method applied in the time domain when frequency domain solutions using the Fast Fourier transform are employed to solve elasto-dynamic problems. In a problem with a domain that is infinite in some or all directions, the Fourier transform is performed along with the exponential window in those directions to create an open boundary. For the directions with finite dimensions, the problem can be solved either analytically or by numerical discretizations such as the finite element method. In the time domain, the central difference formula was adopted.

The procedure involves three steps, similar to those of the exponential window in the time domain: imposing the spatial exponential window to the input force, performing a complex wave number shift and imposing the inverse spatial window to the resulting displacement. The wave number shift in the dynamic stiffness matrix is equivalent to introducing some damping into the system so that the wave motion is damped out before it reaches the boundary. The purpose of the inverse window is to retrieve the displacement in the original system.

The proposed method implemented in the study is efficient due to a couple of reasons. First, it employs Fourier transform in the directions where the domain is unbounded and the Fast Fourier Transform is more efficient than the finite element expansion. This advantage is inherent from the use of the Thin Layer Method. Second, in the time domain, the central difference method is combined with a lumped mass matrix, leading to a highly efficient sparse storage and computational approach. The problem is thus solved in the time-wave number domain. Solving the problem in the time-wave number domain provides an alternative that complements the original Thin Layer Method, in the frequency-wave number domain.

The proposed approach was applied to one-dimensional, two-dimensional and three-dimensional problems to test its effectiveness. All of these problems have real applications.

6.2 Conclusions

In the one-dimensional case, the steady state and transient response of an infinite beam on elastic foundation were studied. In the steady state case, a sinusoidal point load was applied to the beam. Results from the exponential window approach matched very well the analytical solutions for an infinitely long beam with different truncated lengths and excitation frequencies below and above the threshold frequency. In the transient response case, a point load with the time history of a triangular pulse was imposed on the beam. Different pulse widths, which reflect different frequency contents of the excitation, were considered to test the effectiveness of the approach. Within the time duration studied, the approach showed absorption of the waves at the end of the truncated beam while a solution obtained with a finite element discretization of the finite domain showed reflections. There was a problem, however, with waves reflected from the other end.

In the two-dimensional case, the propagation of plane SV and P waves in an infinitely long strip was studied. Different types of loads were considered. In the case of

a uniformly distributed area load, both horizontal and vertical loads were investigated. From the displacement fields at specific instants and the time history of displacements at selected locations, it could be seen that waves were effectively absorbed at the truncated boundary with the exponential window, while in the results obtained with a finite element model, reflected waves were generated at the boundaries. In the case of a line load on the top boundary, the same observations were made. It was also observed that both body and surface waves were effectively absorbed with the exponential window approach, an improvement over some of the previous absorbing boundaries where inadequate absorption of surface waves was reported. It is worth noting this two-dimensional model can be applied to some three-dimensional problems with a dominant dimension in one direction.

Finally, the wave propagation in an unbounded layer was studied as a three-dimensional application of the proposed approach. In this case, a two-dimensional Fourier transform was required, preventing the applicability of the conjugate symmetry property when the complex wave number shift is performed (which is the case in the one and two-dimensional models). The dynamic stiffness must be calculated for all the wave numbers while in the previous studies, only those wave numbers up to the Nyquist wave number needed to be calculated. Again, the results showed effective absorption at the truncated boundary.

6.3 Recommendations for Future Work

An unresolved issue exists for all one-, two- and three-dimensional cases, which leads to a major future effort. In all cases, when the transient response was considered, the exponential window helped to absorb wave propagation in one direction on the truncated boundary but not on the other. On the boundary in the other direction, the exponential window resulted in oscillations that were reflected back into the truncated domain to“ruin” the correct solution after some time. This inadequacy manifests itself as unstable oscillations in the solution after a certain period of time. Although this can be

fixed by increasing the size of the truncated domain in one direction in accordance with the desired time duration, a more efficient solution is yet to be found. There is no clear answer to the question at this time. One potential solution could be to combine the exponential window approach with the one-way wave equation, which is the underlying mechanism of many local absorbing boundary conditions. If a model can be established so that it allows only wave propagation in one direction but not the opposite, from the discussion above, it is to be expected that the exponential window approach could work perfectly.

REFERENCES

[1] J. Wolf, Soil-structure-interaction analysis in time domain. Prentice Hall, Englewood Cliffs, NJ, (1988).

[2] D. Komatitsch, C. Barnes, and J. Tromp, Wave propagation near a fluid-solid interface: a spectral-element approach, Geophysics 65, 2 (2000) 623-631.

[3] A. Sommerfeld, Die greensche funktion der schwingungsgleichung" Jhrber. Deutsch. Math.-Verein, 21 (1912) 309-353.

[4] R. Clayton, and B. Engquist, Absorbing boundary conditions for acoustic and elastic wave equations, Bulletin of the Seismological Society of America 67 (1977) 1529-1540.

[5] E. Lindman, Free-space boundary conditions for time-dependent wave equation, Journal of Computational Physics 18 (1975) 66-78.

[6] A. Bayliss and E. Turkel, Radiation boundary conditions for wave-like equations, Commun. Pure Appl. Math. 23 (1980) 707-725.

[7] R. Higdon, Absorbing boundary conditions for difference approximations to the multidimensional wave equation, Math. Comput. 47 176 (1986) 437-459.

[8] F. Collino, High order absorbing boundary conditions for wave propagation models, Proceedings of the Second International Conference on Mathematical and Numerical Aspects of Wave Propagation, SIAM (1993) 161-171.

[9] M. Grote and J. Keller, Exact nonreflecting boundary conditions for the time dependent wave equation, SIAM J. Appl. Math. 55 (1995) 280-297.

[10] M. Guddati and J. Tassoulas, Continued-fraction absorbing boundary conditions for the wave equation, J. Comput. Acoust. 8 (2000) 139-156.

[11] Baker, G. A., Jr. and Graves-Morris, Padé Approximants. Cambridge University Press, Cambridge, UK, (1996).

[12] G. Waas, Linear two dimensional analysis of soil dynamics problems in semi-infinite layered media, Ph.D. dissertation, University of California, Berkeley, CA (1972).

[13] E. Kausel and J. Roesset, Dynamic analysis of footings on layered media, ASCE Journal of Engineering Mechanics 090 (1975) 568-582.

[14] T. Hagstrom and H. Keller, Exact boundary conditions at an artificial boundary for partial differential equations in cylinders, SIAM J. Math, Anal. 17 (1986) 322.

[15] J. Roesset and H. Scaletti, Boundary matrices for semi-infinite problems, Proceedings of the Third Engineering Mechanics Conference, ASCE (1979) 273-276.

[16] J. Wolf and C. Song, Finite element modeling of unbounded media, John Wiley and Sons Ltd, Chichester, UK(1996).

[17] G. Fix and S. Marin, Variational methods for underwater acoustic problems, Journal of Computational Physics 28 (1978) 253.

[18] J. Keller and D. Givoli, Exact non-reflecting boundary conditions, J. Comput. Phys. 82 (1989) 172-192.

[19] J. Berenger, A perfectly matched layer for the absorption of electromagnetic waves, J. Comput. Phys. 114 (1994) 185-200.

[20] W.C. Chew, W.H. Weedon, A 3D perfectly matched medium from modified Maxwell's equations with stretched coordinates, Microw. Opt. Technol. Lett. 7 13 (1994) 599-604.

[21] W. C. Chew, Q. H. Liu, Perfectly matched layers for elastodynamics: a new absorbing boundary condition, J. Computat. Acoust. 4 4 (1996) 341-359.

[22] F. Collino, C. Tsogka, Application of the perfectly matched absorbing layer model to the linear elastodynamic problem in anisotropic heterogeneous media, Geophysics 66 1 (2001) 294-307.

[23] U. Basu, A. Chopra, Perfectly matched layer for time-harmonic electrodynamics of unbounded domains: theory and finite element implementation, Comput. Methods Appl. Mech. Engrg. 192 (2003) 1337-1375.

[24] G. Gazetas, Stiffness functions for strip and rectangular footings on layered media, M.S. Thesis, Department of Civil Engineering, Massachusetts Institute of Technology, Cambridge, MA (1975).

[25] E. Kausel, Wave propagation in anisotropic layered media, Int. J. Numer. Methods Eng. 23 (1986) 1567-1578.

[26] H. Tan, Displacement approach for generalized Rayleigh waves in layered solid-fluid media, Bulletin of the Seismological Society of America 79 4 (1980) 1251-1263.

[27] R. Ghibril, On the partial discretization of couple plane stratified systems. Ph.D. Dissertation, Department of Civil Engineering, Massachusetts Institute of Technology, Cambridge, MA (1992).

[28] G. Liu, J. Achenbach, A strip element method for stress analysis of anisotropic linearly elastic solids, Journal of Applied Mechanics, ASME 61 (1994) 270-277.

[29] Kausel, E., and Roësset, J. M., Stiffness matrices for layered soils, Bulletin of the Seismological Society of America 71 (1981) 1743-1761.

[30] E. Kausel and R. Peek, Dynamic loads in the interior of a layered stratum: An explicit solution**,** Bulletin of the Seismological Society of America 72 5 (1982) 1459-1481.

[31] J. Doyle, A spectrally formulated finite element for longitudinal wave propagation, International Journal of Analytical and Experimental Modal Analysis 3 (1988) 1-9.

[32] J. Doyle, Wave propagation in structures: spectral analysis using fast discrete Fourier transforms, 2nd edition, Mechanical Engineering Series, Springer, New York, (1997).

[33] R. Al-Khoury, A. Scarpas and J. Blaauwendraad, Spectral analysis of wave propagation in a continuously non-homogeneous soil layer, Proceedings of 10th International Conference on Computer Methods and Advances in Geomechanics 2 (2001) 1059-1064.

[34] J. Proakis and D. Manolakis, Digital signal processing, principles, algorithms and applications, 3rd edition, Englewood Cliffs, Prentice Hall, New Jersey, (1996).

[35] E. Kausel and J. Roesset, Frequency domain analysis of undamped systems. J Eng Mech. 118 (1990) 721-734.

[36] K. Graff, Wave motion in elastic solids, New Ed edition, Dover Publications, New York (1991)

[37] D. Komatitsch and J. Tromp, Introduction to the spectral-element method for 3-D seismic wave propagation, Geophysical Journal International 139 (1999) 806-822.

[38] S. Timoshenko, Method of analysis of statical and dynamical stresses in rail, Proceedings of the Second International Congress for Applied Mechanics, Zurich, Switzerland (1926) 407-418.

[39] J. Achenback, and C. Sun, Moving load on a flexibly supported Timoshenko beam," International Journal for Solids and Structures 1 (1965) 353-370.

[40] S. Kim and J. Roesset, Dynamic response of a beam on a frequency-independent damped elastic foundation to moving load, Can. J. Civ. Eng. 30 2 (2003) 460-467.

[41] R. Gonzales and P. Wintz, Digital image processing, 2nd edition, Addison-Wesley, Reading, MA, (1987).

[42] A. Chopra, Dynamics of structures: theory and applications to earthquake engineering, 2nd edition, Englewood Cliffs, Prentice Hall, New Jersey, (2000).

VITA

Li Liu was born in a small town by the Yangtze River in Hubei province, China. He received his Bachelor of Science and Master of Science in automotive engineering from Tsinghua University, Beijing, China. He also received a Master of Science in mechanical engineering from Texas A&M University in 2005. Beginning May 2005, he was a Ph.D. student of the Zachry Department of Civil Engineering at Texas A&M University, from where he received his Doctor of Philosophy degree in civil engineering, specializing in structural engineering. He can be reached by solidwave@gmail.com, or in care of Dr. Jose Roesset, Zachry Department of Civil Engineering, Texas A&M University, College Station, TX, 77843-3136.